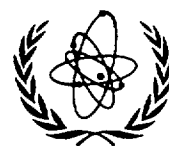


IAEA-TECDOC-1165

Surface modification of materials by ion implantations for industrial and medical applications

Final report of a co-ordinated research project



INTERNATIONAL ATOMIC ENERGY AGENCY

IAEA

July 2000

The IAEA does not normally maintain stocks of reports in this series. They are however collected by the International Nuclear Information System (INIS) as non-conventional literature. Should a document be out of print, a copy on microfiche or in electronic format can be purchased from the INIS Document Delivery Services.

INIS Clearinghouse
International Atomic Energy Agency
Wagramer Strasse 5
P O Box 100
A-1400 Vienna, Austria

Telephone (43) 1 2600 22880 or 22866
Fax (43) 1 2600 29882
E-mail chouse@iaea.org

Orders should be accompanied by prepayment of 100 Austrian Schillings in the form of a cheque or credit card (VISA, Mastercard).

More information on the INIS Document Delivery Services and a list of national document delivery services where these reports can also be ordered can be found on the INIS Web site at http://www.iaea.org/inis/dd_srv.htm

The originating Section of this publication in the IAEA was:

Industrial Applications and Chemistry Section
International Atomic Energy Agency
Wagramer Strasse 5
P.O. Box 100
A-1400 Vienna, Austria

**SURFACE MODIFICATION OF MATERIALS BY ION IMPLANTATIONS FOR
INDUSTRIAL AND MEDICAL APPLICATIONS**

IAEA, VIENNA, 2000

IAEA-TECDOC-1165

ISSN 1011-4289

© IAEA, 2000

Printed by the IAEA in Austria

July 2000

FOREWORD

The objectives of the Co-Ordinated Research Project (CRP) on Modification Of Materials by Ion Treatment for Industrial Applications were to develop economically acceptable surface modification techniques leading to thick treated layers, to predict ion beam mixing and impurity atom migration during and after implantation, and to evaluate the tribological post-implantation properties and performance of treated components.

Laboratories from Belarus, China, India, Poland, Slovenia, Spain, Romania, Thailand and the United States of America participated in the project. The CRP was able to evaluate alternative ion beam based coating techniques to coat relatively thicker coatings and achieve improvement in tribological and mechanical properties of the surfaces.

There were several outcomes from this CRP in both basic research and in applications leading to new implantation techniques, characterization procedures and new post-implantation evaluation tests.

An important activity was the common interlaboratory test for all participants. Ten standard samples of CrN coated stainless steel were provided to each participating group. The CRP participants undertook characterization and testing of the samples according to the techniques, facilities and capabilities at their disposal.

This publication provides a brief review of the methodology of ion beam implantation and describes the major results and achievements obtained.

The IAEA wishes to thank all the scientists who contributed to the progress of this CRP and to the preparation of this TECDOC, and in particular A.S. Khanna, who drafted the text. The IAEA officer responsible for the publication was J. Thereska of the Division of Physical and Chemical Sciences.

EDITORIAL NOTE

The use of particular designations of countries or territories does not imply any judgement by the publisher, the IAEA, as to the legal status of such countries or territories, of their authorities and institutions or of the delimitation of their boundaries.

The mention of names of specific companies or products (whether or not indicated as registered) does not imply any intention to infringe proprietary rights, nor should it be construed as an endorsement or recommendation on the part of the IAEA.

CONTENTS

1. INTRODUCTION	1
2. METHODOLOGY OF ION BEAM DEPOSITION	3
2.1. Ion beam mixing.....	3
2.2. Ion beam assisted deposition (IBAD).....	3
2.3. Plasma nitriding.....	5
2.4. Plasma arc.....	6
2.5. Metal vapour vacuum arc (MEVVA).....	6
3. ION BEAM ANALYSIS	7
3.1. Rutherford backscattering (RBS)	7
3.2. Elastic recoil detection analysis (ERDA)	9
3.3. Nuclear reaction analysis (NRA).....	10
4. EXPERIMENTAL WORK	11
4.1. Y ion implantation on ZrO ₂ ceramics.....	11
4.1.1. Microhardness and flexural strength	12
4.1.2. Fracture toughness	13
4.1.3. Surface resistance	13
4.2. Mo and Y ion implantation on Si ₃ N ₄ ceramics	13
4.2.1. Scanning auger microprobe	14
4.2.2. X ray diffraction analysis.....	14
4.2.3. Microhardness	15
4.2.4. Sheet resistance.....	17
4.2.5. Fracture toughness	17
4.3. Particle migration in the Ni/Al multilayers	18
4.3.1. Auger electron spectrometry (AES).....	18
4.4. Investigation of interaction of gaseous ions with getter material	19
4.5. Formation of thick, nitrogen rich layer.....	22
4.5.1. Wear test.....	26
4.6. Formation of thick, wear-resistant metallic layers via ion beam mixing technique	26
4.6.1. Auger electron spectrometry (AES).....	26
4.6.2. Wear and friction test	27
4.7. N and B ion implantation on SKD 11 steel	29
4.7.1. Hardness	29
4.7.2. Wear and friction test	29
4.7.3. Friction.....	30
4.8. N ion implantation assisted by preparative and closing implantation for surface modification of tool steel	30
4.8.1. Auger electron spectrometry (AES).....	31
4.8.2. Hardness	32
4.8.3. Wear test.....	35
4.9. Applied high-current N ion implantation of industrial steels and tools	36
4.9.1. X ray diffraction.....	36

5.2.1. Tribological and dynamic micro-indentation test.....	79
5.2.2. Hardness and modulus.....	83
5.2.3. Adhesion and scratch test	83
5.2.4. Impact testing.....	85
5.2.5. Microhardness test.....	85
5.2.6. Dry sliding test.....	86
5.2.7. Friction and wear test.....	86
5.2.8. Corrosion test.....	89
5.2.9. Discussion.....	90
6. COST ANALYSIS FOR ION BEAM MODIFICATION PROCESSES.....	92
7. CONCLUSIONS	93
8. RECOMMENDATIONS	94
REFERENCES	95
CONTRIBUTORS TO DRAFTING AND REVIEW	101

1. INTRODUCTION

Ion implantation is a suitable surface modification process for improving tooling life and performance of engineering and biomedical components. The growing interest in the field of ion implantation for modifying material properties was recognized by the IAEA many years ago. A consultants meeting (CM) was held in San Sebastian, Spain, from 29 August to 1 September 1995 on Industrial Applications of Ion Beam Implementation for Modifying Metal Properties with the objective of assessing the present situation and trends on technical and economic benefits of the technology and to formulate a CRP proposal for research and development on improvement of surface behaviour of engineering materials with respect to wear, abrasion and corrosion resistance.

It was the conclusion of this CM that ion treatment technologies, in spite of past limited acceptance by industry, have good potential for addressing material problems in wear and corrosion. The CM recognises, therefore, a need to promote ion treatment technologies for industrial applications. This CM recommended the CRP on Modification of Materials by Ion Treatment for Industrial Applications with the following objectives:

- Development of economically acceptable surface-modification techniques leading to thick treated layers that will appropriately extend the lifetime of components under typical working conditions;
- Development of methods of predictions and measurement of 'ion' mixing and migration during and after implantation, leading to an understanding of mechanisms that yield substantial protective layers for various materials;
- Post-implantation evaluation of the properties and performance of treated components and the correlation of those with the microstructure of the treated layers.

Well known laboratories from developed and developing countries were involved in co-operation in the framework of this CRP. The first RCM of this CRP was organized in Vienna, on 25–29 March 1996, the second one in Beijing, China, on 1–5 September 1997 and the third final meeting was held in Vienna on 9–12 November 1998.

Very different techniques were used for production of modified layers and coatings on materials for potential industrial and medical applications. Several methods of prediction and measurement of ion mixing and migration were applied. Post implantation evaluation of some properties were investigated as well.

The participants have benefited from exchanging information and sharing experience, from samples preparation and surface analytical services, and from mechanical and corrosion testing of coated samples. A networking scheme for interaction among CRP participants was built up, with precise tasks for 'performers' and 'customers'. The inter-laboratory research/collaborative efforts were focused on 'round robin' testing of CrN coated samples .

The CRP participants were involved with different ion assisted coatings technologies. The techniques of coatings and the coatings created were amply demonstrated that fulfil some conditions for industrial implantation requested by end users, as repeatability, controllability, good adhesion, uniformity, good tribological properties. The original ion implantation technique has therefore been complemented by ion beam assisted techniques for deposition to accomplish thicker layers and suitable for many industrial applications.

The ion beam technology is mainly based on the production of ionised atoms or molecules, which lend themselves to be accelerated in an electric field. These ions can be utilized in a variety of ways to either modify or characterise materials. For example, the process of ion implantation is used to create new surface alloys and modify surface related properties such as hardness, wear and friction, corrosion resistance of materials. It is also applicable in changing mechanical, electrical, optical and chemical properties. The application of ion implantation to semiconductor industry is already well established. Ion beam assisted coatings and various plasma-based coatings involving ion beams, can give coating thickness in the range of 1–2 μm . These can be selectively applied for various industrial applications and can also be extended to many medical applications such as bio-implants. The ion beam processes will continue to play an important role in further understanding and refinement of surface treatment of materials.

The ion beam technology has and will continue to make significant contribution in "niche" markets ranging from some specialised tools, used in industry, to surface treatment of intricate devices used in the medical field. Hence, one of the main requirements of the wider applications is making this technology more known to industry and making end users aware of the benefit.

The methods of the coatings developed and evaluated in the frame of this CRP are:

- Ion implantation (II).
- Ion beam mixing (IBM).
- Ion beam assisted deposition (IBAD).
- Plasma source ion implantation (PSII).
- Plasma source ion deposition (PSID).
- Metal evaporation arc implantation source (MEVVA).

After preparing the samples it is essential to characterise and analyse the coated materials. Several techniques have been employed for this purpose. They are:

- Rutherford backscattering (RBS).
- Auger electron spectrometry (AES).
- Scanning electron microscopy (SEM) and atomic force microscopy (AFM).
- X ray diffraction (XRD)/Glancing XRD.
- Raman spectroscopy.
- Transmission electron microscopy (TEM).

The main aim of using ion beam coating is to improve mechanical, electrical, chemical and tribological properties of materials. In order to study these properties the following techniques were used for evaluating the performance of the coated samples:

- Wear and friction.
- Microhardness.
- Fracture toughness.
- Roughness.
- Scratch test.
- Impact test.
- Adhesion.

- Corrosion/oxidation.
- Sheet resistance.

This monograph is extracted from the experimental work performed in CRP participants' laboratories. It presents the relevant experimental work of the CRP participants during three year network co-operation.

The TECDOC summarises the current status and prospects in surface modification by ion implantation methodology and technology, providing new information in basic and applied research with direct interest to developing countries. It aims to disseminate the state-of-the-art to other laboratories of developing countries helping them overcoming difficulties in experimental work and applications. This report can be used as basic document for the IAEA training courses and workshops for scientists and engineers of research and technological institutions and universities to introduce, promote and transfer the technology to MS developing countries.

2. METHODOLOGY OF ION BEAM DEPOSITION

2.1. ION BEAM MIXING

The subject of ion beam mixing deals with the compositional and structural changes of two or more component systems under the influence of an ion irradiation. Due to these changes, material properties of the system may be modified in ways sometimes difficult to achieve by conventional methods. From a collisional point of view, ion beam mixing relies on particle-solid interaction. The phenomenon becomes more complex when thermodynamical forces are involved, and these forces are sometimes modified by the presence of high concentrations of defects in the system leading to various migration mechanism of atoms, such as Radiation Induced Segregation (RIS) or Radiation Enhanced Diffusion (RED).

Ion beam mixing involves the use of energetic ion beams for driving and thereby "intermixing" the pre-deposited thin film atoms into substrates, via the dynamic collision cascades produced by the penetrating ions. The process is schematically shown in Fig. 1.

The precursors of the work on ion beam mixing were studies of the preferential sputtering of silicides where it was found that the composition changes occurred over the depth of the bombarding ions. Aside from the influence of sputter depth profiling, there were some indications that the ion induced reactions could be used for material modification. From the technological point of view Ion beam Mixings offers an unique possibility to form almost any alloy of any composition and highly metastable, often amorphous, structure.

2.2. ION BEAM ASSISTED DEPOSITION (IBAD)

IBAD consists of simultaneously depositing the desired material using some evaporating technique and bombarding by energetic ion beams. Schematic of the process is shown in Fig. 2. This technique has been studied by a number of researchers for the purpose of understanding the role of energetic ions in the conventional physical vapour deposition (PVD) processes. It has been recognized that the presence of energetic ions has a synergistic effect on thin film growth. There are several aspects of film growth that have been beneficially influenced by ion bombardment during thin film deposition including:

- (a) film nucleation growth,
- (b) adhesion,
- (c) internal stress,
- (d) surface morphology,
- (e) density, and
- (f) composition.

This technique combines the advantages of a vacuum coating method, electron beam evaporation and ion implantation. In contrast to plasma-based physical vapour deposition (PVD) techniques, the actual coating process is decoupled from the energy-input process. This makes the technique highly versatile and flexible. It has a large number of parameters, which are independent from each other and can be varied over a wide range. Additionally, it is highly reproducible. Due to these features, IBAD constitutes an excellent addition to other PVD methods and should be able to provide coating systems with special features, which in some cases can not be obtained by other techniques. For instance, a comparison of IBAD and other PVD methods for depositing corrosion protection layers on temperature sensitive substrates under very low process temperatures showed that the IBAD films generally had a higher structural density and adhesion to the substrate than the corresponding PVD films. This resulted in a superior corrosion protection performance. The ion beam provides the energy, which is necessary to grow films with suitable structures and sufficient adhesion. For a flexible IBAD system, a very wide range of ion energies should be available. The energies, which are suitable for optical thin films are quite different from those, which are useful for tribologically protective coatings.

A demonstration of the effect of ion bombardment on nucleation, involved measuring the electrical conductivity between two electrodes on an insulator while Al atoms were being deposited (at about 10 monolayers per second) both with and without simultaneous 5 keV Ar ion bombardment. The time for onset of conduction was reduced by a factor of 2 to 4 using ion bombardment, this being attributed to creation of nucleation sites by the ion beam.

Ion bombardment during deposition has also been shown to produce quite drastic structural changes. For example, ion bombardment changes a normally columnar morphology of metals into a more dense isotropic structure.

2.3. PLASMA NITRIDING

In recent years, a variety of surface engineering techniques have been used to improve titanium's tribological properties by producing a hard surface coatings. Plasma or "glow discharge" nitriding is a technique for producing a hard surface coating of titanium nitride on titanium alloys. It has been successfully employed to modify the surface of various engineering materials to improve their metallurgical and mechanical properties. The plasma nitriding process makes use of an abnormal glow discharge, which is associated with high current and charge densities. Figure 3 shows the schematic of plasma nitriding process. The components to be nitrided are electrically isolated and placed in a vacuum furnace, which is evacuated and back-filled with the treatment gas. A dc voltage is then applied between the component (cathode) and furnace walls (anode) and the potential difference ionizes the treatment gas producing the glow discharge. Positive ions in the treatment gas are accelerated towards the negatively biased substrates and hit the surface with high kinetic energy giving rise to sputtering of the surface, and heating of the components. In the plasma nitriding of titanium alloys, nitrogen ions impinge on the surface and react to form a nitrogen rich film,

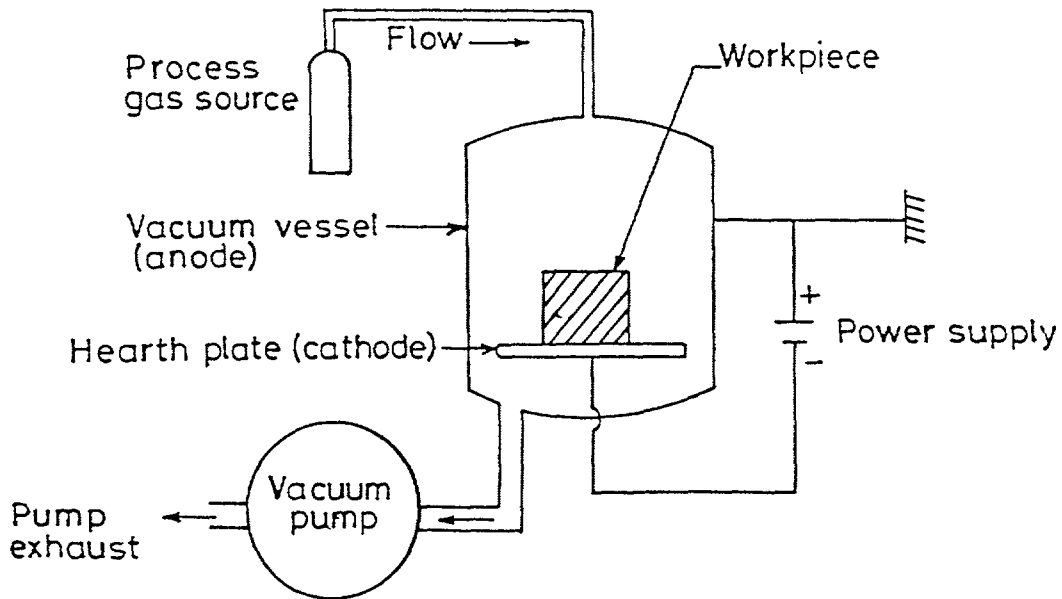


FIG. 3. Schematic of plasma nitriding technique.

which results in both the formation of a compound nitride layer on the surface and the diffusion of nitrogen in the substrate. Plasma nitriding gives high surface hardness, large production rate and gradual transition to structure of substrate material.

2.4. PLASMA ARC

Plasma arc spray (APS) depositions are being used to provide ceramic or metal alloy surface on steel and other substrates for many types of process equipments. The plasma arc spray process belongs to that family of processes that are used to produce "thermal sprayed coatings". The process consists of injecting a powdered material into a highly turbulent, high temperature ionized gas stream. Figure 4 illustrates the basic principles of APS technology.

The powder melts and is accelerated towards a target substrate. Upon impact, molten droplets are essentially splat cooled which gives rise to the rapid solidification rate characteristic of the microstructure of the deposit. Powders ranging from a few microns to several hundred microns in diameter are injected at rates from <250 g/hr to >10 kg/hr to form deposits or spray-cast structure that ranges from $1\ \mu\text{m}$ – $5\ \mu\text{m}$ thickness. The process is so versatile that virtually any material that exhibits molten condition can be stoichiometrically deposited.

2.5. METAL VAPOUR VACUUM ARC (MEVVA)

The metal vapour vacuum arc source was invented in the mid 1980s at Lawrence Berkeley Laboratory for application in high-energy physics, and is now extending its application field to surface modifications of materials. MEVVA has, in principle, great advantage in the production of high ion current density of various metals (including C), which has been difficult to obtain by using conventional ion implanter. It can produce pulsed intense metal ion current, and is easy to operate. The energy of ion is between 20 keV and 200 keV, and the average ion current is between 1 mA and 10 mA. Vacuum during the process is maintained at $\sim 10^{-5}$ torr.

3. ION BEAM ANALYSIS

There are several accelerator-based techniques that can be employed to identify the elements and determine their relative concentrations in the material under investigation. These are: Rutherford Backscattering (RBS), Elastic Recoil Data Analysis (ERDA), Nuclear Reaction Analysis (NRA), Secondary Ion Mass Spectroscopy (SIMS), etc. We shall discuss here some of the techniques like RBS, ERDA, NRA.

3.1. RUTHERFORD BACKSCATTERING (RBS)

This is a well-established method of studying the atomic depth distribution in the near surface regions (typically up to depth of about 2 microns). *Usually the target atomic mass is larger than that of the projectile.* In almost all studies the incoming projectile is a ^4He ion having the energy ranging from 1 to 8 MeV. With the advent of heavy ion accelerators several other ions like B, C, N and O have also been occasionally employed to obtain better mass resolution. In most cases the incoming ions do not produce nuclear reactions as the measurements are carried out well below the Coulomb barrier for such reactions. The RBS spectrum depends on the kinematics of the scattering and the energy loss of the projectile in the sample. Both these are well understood and well studied and hence can be directly applied to obtain the concentration of the scattering nuclei and their depth distribution. The experimental arrangement is quite simple. The target to be investigated is mounted in a vacuum chamber (with vacuum of the order of 10^{-6} torr.) which is situated at the end of a beam line of an accelerator capable of delivering 1 to 10 MeV ions with good energy resolution and stability. Typically the electrostatic linear accelerators, either single ended or tandem type are well suited for this purpose. The scattered charged particle is detected in a simple semiconductor surface barrier detector. A low noise preamplifier with a suitable linear amplifier and a multichannel analyzer are needed for efficient data acquisition. The schematic experimental arrangement is shown in Fig. 5. The incoming ion loses its energy as it travels within the sample before getting scattered, transferring a part of its energy to hit atomic nuclei within the target and finally, a part of its energy is lost on its way out to the detector after scattering. The energy of the detected particle is a function of the depth of scattering and mass of target atoms and the scattered yield is a measure of concentration of the scattering centres.

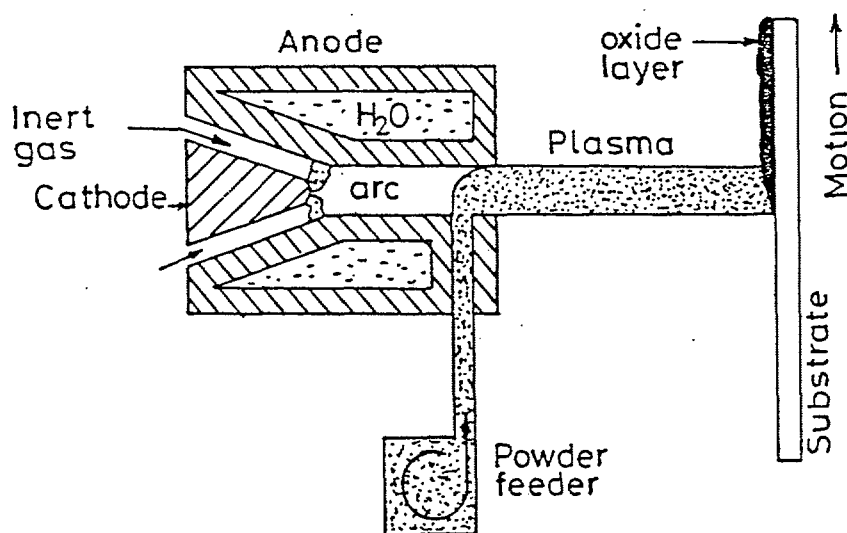


FIG. 4. Basic principles of APS technology.

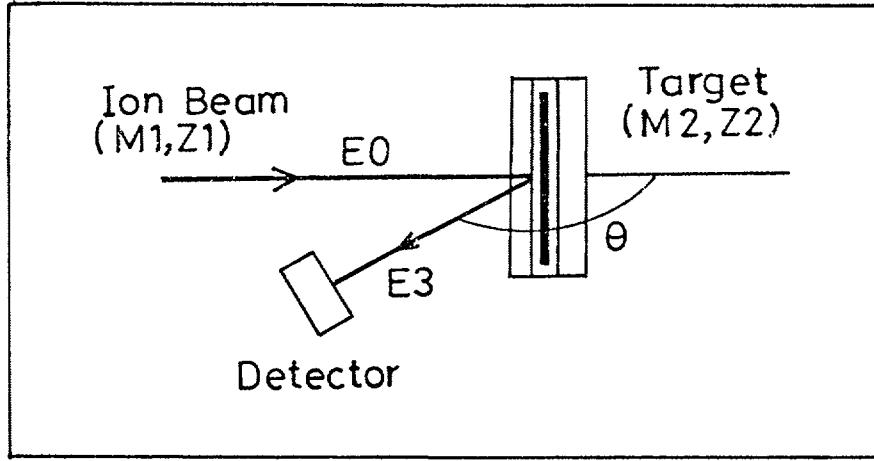


FIG. 5. Schematic of RBS experimental arrangement.

Let E_0 be the energy of the incident particle of mass M_1 and E_1 be the energy of the particle at the time of scattering. Then the energy E_2 of the particle immediately after scattering by a target atom of mass M_2 is given by:

$$E_2 = KE_1 \quad (1)$$

where the kinematical factor K is obtained from the relation

$$K = \left[\frac{((M_1^2 - M_2^2) \sin^2 \theta)^{1/2} + M_1 \cos \theta}{M_1 + M_2} \right]^{1/2} \quad (2)$$

for $M_1 < M_2$ and for scattering angle θ .

The final energy E_3 of the detected particle is:

$$E_3 = E_2 - t_2 (dE/dx)E_2 \quad (3)$$

$$\text{with } E_2 = KE_1 = K[E_0 - t_1 (dE/dx)E_0] \quad (4)$$

t_1 and t_2 being the distances traversed by the projectile in the sample before and after the scattering respectively. In these expressions (dE/dx) is the energy loss of the projectile at the indicated energy, which are extensively tabulated. Thus, knowing E_0 , E_3 , M_1 , M_2 and θ , the depth at which the scattering centre is located can be determined. The RBS scattering cross-section, for scattering angle θ , is given by:

$$\sigma(\theta) = \left(\frac{Z_1 Z_2 e^2}{E} \right)^2 \text{Cosec}^4 \left(\frac{\theta}{2} \right) \quad (5)$$

Z_1 and Z_2 being the atomic numbers of the projectile and the scattering atom respectively. The yield of scattered projectile is proportional to the scattering cross-section. Thus, by

measuring the relative yields of particles scattered from various atomic species at same depth one can easily determine their relative concentrations. A typical RBS spectrum is shown in Fig. 6.

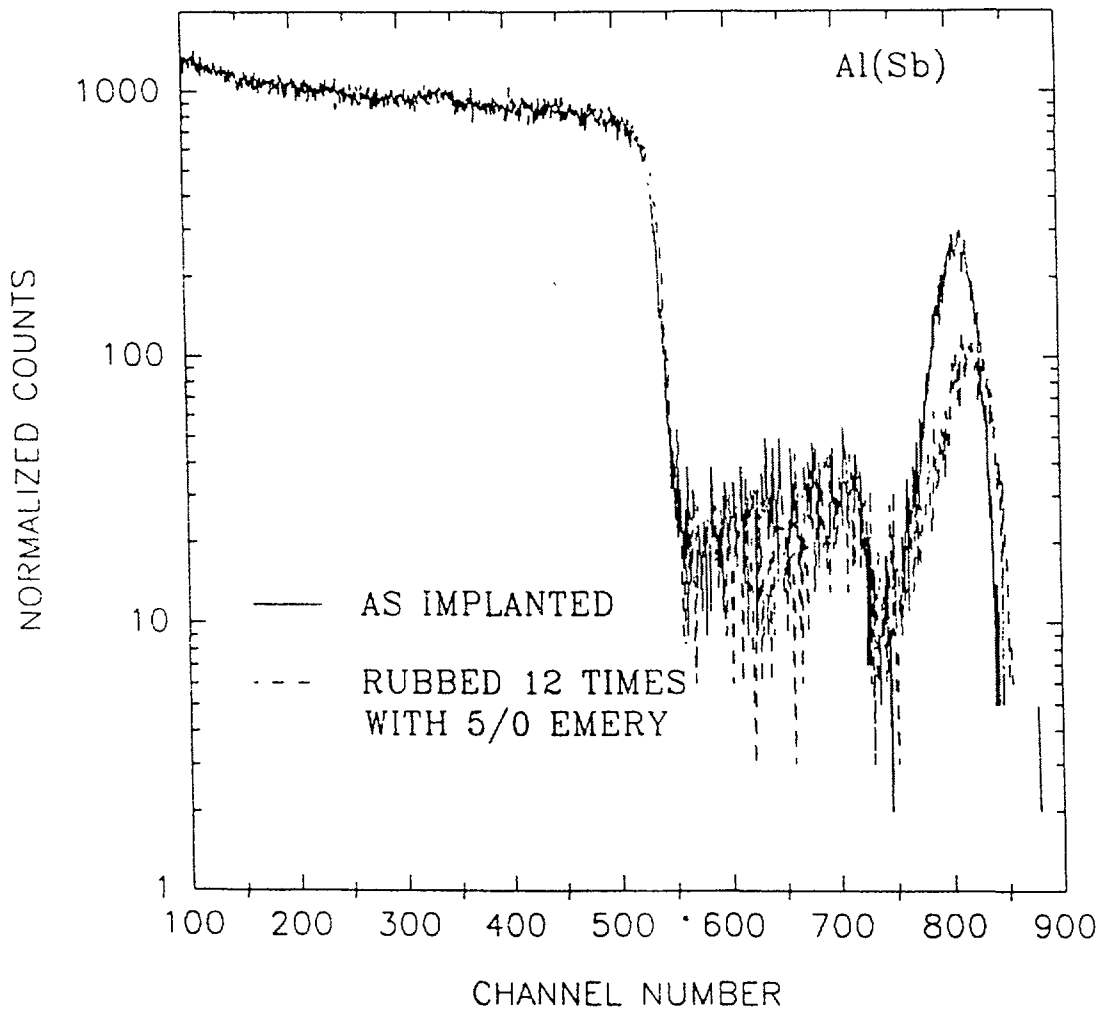


FIG. 6. RBS spectrum of as implanted FeSb sample.

3.2. ELASTIC RECOIL DETECTION ANALYSIS (ERDA)

RBS is suitable if the probe atoms are heavier than the projectile ions. In the case of lighter atoms, the technique of elastic recoil detection analysis (ERDA) can be employed. Here, the incident projectile ion causes the target atom to recoil in the forward direction. Figure 7 shows the geometrical arrangement of the experimental set up. The atoms of different masses recoil with different energies and hence can be separated out in the recoil energy spectrum. The recoil energy, E_R , is given by:

$$\frac{E_R}{E_P} \equiv K = \frac{4 m_P m_T}{(m_P + m_T)^2} \cos^2 \phi \quad (6)$$

where ϕ is the laboratory angle at which the recoil is detected and E_P is the projectile energy. The energy of the recoils from various depths of the sample is determined by two factors: (i) the rate of energy loss $(dE/dx)_{in}$ of the incident ion in the target, and (ii) the rate of energy loss

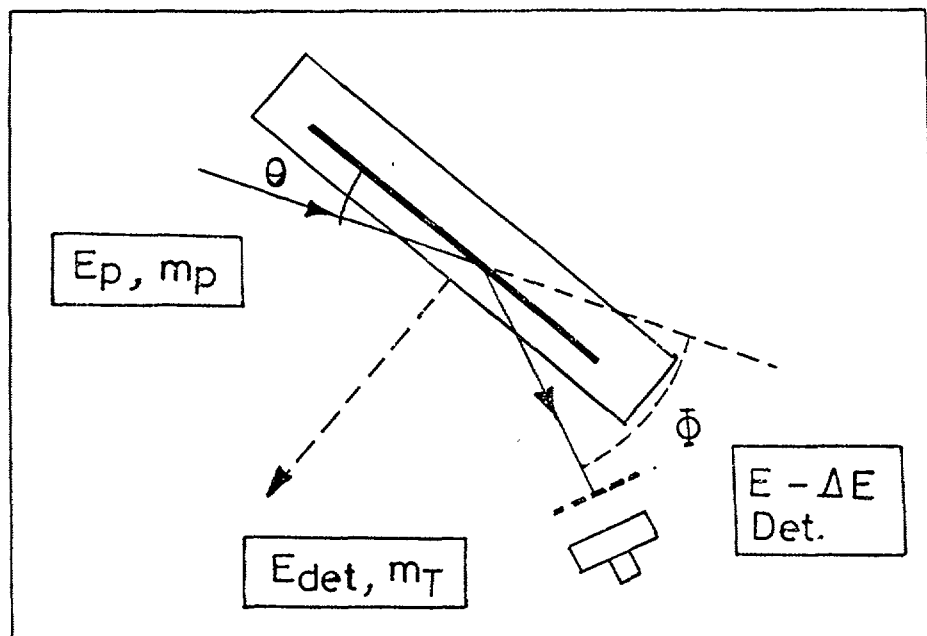


FIG. 7. Geometry for ERDA measurements.

$(dE/dx)_R$ of the recoiling atom in the target. If θ is the angle at which the beam is incident on the target and d is the scattering depth then the energy of the recoil at the detector E_{det} is given by:

$$E_{det} = K \left[E_p - \left(\frac{d}{\sin\theta} \right) \left(\frac{dE}{dx} \right)_n \right] - \left[\frac{d}{\sin(\phi - \theta)} \left(\frac{dE}{dx} \right)_R \right] \quad (7)$$

although with thin film samples a simple Si surface barrier detector is sufficient to separate out the energy signals from different recoiling atoms, in experiments with thick targets a $(E - \Delta E)$ telescope is needed to get depth distributions of various recoils in the target material.

3.3. NUCLEAR REACTION ANALYSIS (NRA)

This method usually requires protons and alpha particles of energy ranging from 100 keV to 10 MeV, although occasionally other ions can also be used. These particles induce nuclear reactions in target materials. The reaction products emitted are gamma rays, protons, neutrons, alpha particles, e^- , γ , which are detected using the nuclear radiation detectors. The nuclear reactions produce radioactive nuclei, which are long-lived (half-life > few minutes) and short lived (half-life < few seconds). In the former case the samples can be studied *off-line*, whereas in the latter, samples are investigated *in situ*. In many instances the nuclear reactions take place at a well defined energy, within a narrow energy range (resonant reactions). Under such conditions it is possible to study the depth distribution of the target atoms by varying the energy of the projectile. In many cases, where there is no resonance reaction, it is still possible to obtain the depth information if the "Q" value of the reaction (threshold energy for the reaction to occur) along with the energy of the incident particles are known and the energy of the emitted particles are measured. The detectors normally used are charged particle semiconductor detectors, neutron counters and gamma ray detectors. The method is well developed and described in detail in several review articles.

In the case of nuclear reactions producing long lived radioactive nuclei, the yield of the product is given by the expression:

$$N_0 = \sigma n_p \rho X t \quad (8)$$

where σ is the reaction cross-section in cm^2 , n_p is the number of incident ions per second, ρ is the number density of the atomic species in the target (atoms/cc), X is the effective target thickness in cms., and t is the time of irradiation in seconds. Here by effective target thickness we mean the thickness throughout which the reaction can take place. The factor (ρX) will therefore be expressed in the units of ats./cm^2 . The well known radioactive decay law gives the number of radioactive nuclei at any time t_1 , after stopping the irradiation:

$$N(t_1) = N_0 (1 - \exp(-\lambda t_1)) \quad (9)$$

λ being the decay constant for the radioactive nuclei produced in the reaction.

The decaying radioactive nuclei, in general, emit characteristic gamma rays. The energies of these gamma rays are tabulated extensively. Thus, by measuring the intensities of the specific gamma rays and using eqns. 6 and 7, value of ρ can be extracted even in case of extremely low concentrations. Another application of this method is in the study of wear and corrosion properties of various materials. Here the residual radioactivity in the material, after subjecting it to corrosion and wear processes, are measured. Of course "hot laboratory" facilities for handling and disposal of radioactive materials are required.

4. EXPERIMENTAL WORK

This section describes the actual experimental details of the coating methods (i.e. the methods of sample preparation), characterization and the performance of the coated samples, with reference to mechanical, electrical, chemical and tribological properties.

4.1. Y ION IMPLANTATION ON ZrO_2 CERAMICS

Zirconia ceramics were modified by Y ion implantation in a MEVVA implanter. The samples used for implantation were hot-pressed ZrO_2 ceramics, which were cut into $3 \times 6 \times 40 \text{ mm}^3$ bars, then polished to mirror finish with 0.5 micron diamond paste. It contained 90% tetragonal and 10% monoclinic phase. Its density was 6.05 g/cm^3 , and the grain size was one micron. Before implantation all samples were carefully ultrasonically cleaned in acetone and methanol. The Y ion implantation was carried out in a MEVVA source with an extraction voltage of 60KV. The samples were implanted with an ion current density of $80 \mu\text{A/cm}^2$ and the ion doses ranged from 8×10^{16} to $1.8 \times 10^{18} \text{ Y/cm}^2$. The samples were not cooled during implantation and their temperature rise was only due to ion bombarding.

The phase structure of as-implanted samples was determined by XPS and XRD. The microhardness, flexural strength and fracture toughness of as-implanted samples were measured. The fracture toughness was measured in the standard mode with a span of 24 mm and a loading velocity of 0.05 mm/min.

XRD and XPS analyses of implanted samples showed that there were basically T- ZrO_2 (tetragonal phase), M- ZrO_2 (monoclinic phase), CeO_2 , and the Y_2O_3 phases in the implanted region. Transformation of some of the T- ZrO_2 phase into M- ZrO_2 phase took place as dose of

implantation increased. Amorphization of ZrO₂ ceramics was also observed in the implanted region after Y ion implantation at doses above 6×10^{17} Y/cm².

4.1.1. Microhardness and flexural strength

The microhardness of as-implanted samples were determined by Knoop type diamond indenter in a load range of 0.1 to 0.5 N. The tests were carried out at ambient condition. Ten indentations per sample were made and the hardness was evaluated from the mean long diagonal value. The microhardness of as-implanted zirconia is shown in Table I. The Knoop hardness of the control sample is about 780 kg/mm² for different loads. It can be seen that the microhardness of the as-implanted sample was higher than that of the control sample and was found to increase at lower dose. The maximum hardness was observed when the sample was implanted with a dose of 2×10^{17} Y/cm², and minimum hardness at a dose of 1.8×10^{18} Y/cm². Increased dose rate results in radiation damage, thus affecting the hardness.

The flexural strength of samples was measured at room temperature using three-point bending mode with a span of 30 mm. The Flexural strength of Y ion implantation samples is shown in Table II. The flexural strength of as-implanted zirconia increased with increasing ion dose and reached the maximum value of 829 MPa at the dose of 2×10^{17} Y/cm², i.e. 17.3% higher than that of the control sample.

TABLE I. KNOOP MICROHARDNESS AS A FUNCTION OF ION DOSE FOR Y ION IMPLANTED ZrO₂ (KG/MM²)

Y-Ion Dose ($\times 10^{17}$ Y/cm ²)	Load (Newton)		
	0.1	0.25	0.5
0	775	782	779
0.8	968	1180	1269
2	1410	1689	1386
6	1116	1352	1332
10	1092	1290	1230
14	1054	1274	1199
18	868	1063	1090

TABLE II. FLEXURAL STRENGTH AS A FUNCTION OF ION DOSE FOR Y-ION IMPLANTED ZIRCONIA

Ion Dose ($\times 10^{17}$ Y/cm ²)	0	0.8	2	6	10	14	18
Flexural Strength (MPa)	707	808	829	788	707	574	08

It is clear from Table II that the implantation of zirconia with Y ions above a "critical dose" of about 2×10^{17} Y/cm² resulted in a significant decrease of flexural strength. The flexural strength of the sample implanted with the highest dose (1.8×10^{18} Y/cm²) decreased to 508 MPa and was 28.1% lower than the control sample's flexural strength. A possible

explanation is that the radiation damage piled up and expanded with increasing ion dose, and finally resulted in degradation of flexural strength. The dose dependence of the flexural strength of as-implanted samples was similar with that of microhardness of as-implanted samples.

4.1.2. Fracture toughness

The fracture toughness of as-implanted samples is shown in Table III. The fracture toughness of the control sample was $11.4 \text{ MPa}\cdot\text{m}^{0.5}$. Fracture toughness values of all as-implanted samples were less than that of the control sample. The fracture toughness decreased gradually with increasing ion dose. For the samples implanted with a dose of $2 \times 10^{17} \text{ Y/cm}^2$, the minimum fracture toughness was observed, which was 24.2% lower than the fracture toughness of the control sample.

TABLE III. FRACTURE TOUGHNESS OF AS-IMPLANTED SAMPLES AS A FUNCTION OF ION DOSE

Ion Dose ($\times 10^{17} \text{ Y/cm}^2$)	0	0.8	2	6	10	14	18
Fracture Toughness ($\text{MPa}\cdot\text{m}^{0.5}$)	11.4	9.5	8.6	8.8	9.3	9.9	10.6

It can be found from Table III that the implantation of zirconia above a "critical dose" of about $2 \times 10^{17} \text{ Y/cm}^2$ resulted in a gradual increase of fracture toughness. It is considered that, in general, the change of surface fracture toughness of as-implanted samples was due to microstructural change and stress status of surface layer. At low ion doses the fracture toughness of as-implanted sample decreased rapidly because of the radiation damage, and the minimum value was reached at a dose of $2 \times 10^{17} \text{ Y/cm}^2$. Then the fracture toughness gradually improved with increasing ion dose because of increase of compressive stress and formation of amorphous surface layer. The compressive stress prevented surface flaw from forming and extending, thus improving the fracture toughness.

4.1.3. Surface resistance

The surface resistance of as-implanted ZrO_2 samples is shown in Fig. 8. It was observed to decrease with increasing implantation dose, presumably due to the surface metallization of ZrO_2 ceramics. In the case of the sample implanted with a dose of $1.4 \times 10^{18} \text{ Y/cm}^2$ the surface resistance increased greatly because of sputtering effect.

4.2. MO AND Y ION IMPLANTATION ON Si_3N_4 CERAMICS

The samples used for implantation were hot-pressed Si_3N_4 ceramics, which were cut into $13 \times 13 \text{ mm}^2$ plates with a thickness of 8mm. One side of each sample was polished to mirror finish with 0.5 micron diamond paste. Before implantation all samples were ultrasonically cleaned in acetone and methanol. Mo ion implantation was performed in a MEVVA source implanter with an extraction voltage of 40 and 60 KV. The Mo ion implantation was mainly carried out at 120 keV and 180 keV corresponding to the extraction voltage of 40 KV and 60 KV. The particle current fraction of Mo ion beam was composed of 2% Mo^+ , 49% Mo^{3+} , 21% Mo^{2+} , 25% Mo^{4+} , and 3% Mo^{5+} . The samples were implanted with an ion current density of $53 \mu\text{A/cm}^2$.

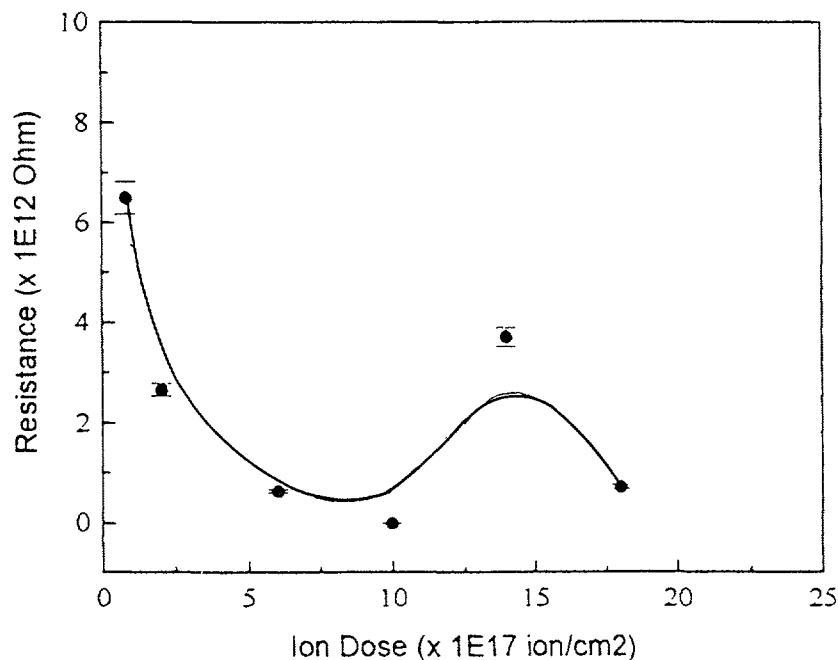


FIG. 8. Surface resistance as a function of ion influence for Y ion implanted ZrO_2 ceramics.

Y ion implantation was carried out with an extraction voltage of 40 KV. The particle current fraction of the Y ion beam was composed of 5% Y^+ , 62% Y^{2+} , and 33% Y^{3+} . The implantation energy of Y ion was mainly 90 keV. The samples were implanted with Y ion current density of 53 A/cm² and 79 μ A/cm². The implantation doses of Mo ion and Y ion ranged from 2×10^{17} to 18×10^{17} Y/cm². The samples were not cooled during implantation and their temperature rise was only due to ion bombardment.

4.2.1. Scanning auger microprobe

The as-implanted samples were characterized by scanning auger microprobe (SAM) and X ray diffraction (XRD) to determine the ion depth profiles and structure. Figure 9 shows the result of SAM analysis for Y ion implanted samples. For clarity, the distribution of N, Si, and O elements were omitted. The SAM analyses were stopped when big zigzag lines occurred on the depth profiles. It was observed that the sputtering rate of the depth profiles was 30 nm/min for silicon nitride samples. It is clear from Fig. 9 that the Y ion distribution extended much deeper than the projected ion range as predicted by the TRIM92. It is also found that depth of implanted Y ion increased initially and then decreased with increasing Y ion dose. The maximum depth value was obtained for the sample bombarded with a dose of 6×10^{17} ion/cm².

4.2.2. X ray diffraction analysis

The representative X ray diffraction patterns are presented in Fig. 10. All Bragg peaks can be attributed to Si_3N_4 phase. No Mo-Si-N or Y-Si-N compounds were observed after implantation with different ion doses. The samples implanted with Mo ion however showed the formation of $MoSi_2$. This means that the Mo ions implanted into the Si_3N_4 samples had reacted with Si atoms under implantation energy of 180 keV. It can be seen from Fig. 10 that the Si_3N_4 peaks become weak with increasing implantation dose. It is suggested that amorphization of Si_3N_4 ceramics occurred gradually.

4.2.3. Microhardness

Vickers profile indenter at a load of 1N was used to determine the microhardness of as-implanted sample. The tests were carried out at ambient conditions. A standard loading cycle time of 25 s was used for each test to minimize the effect of indentation creep on hardness. The microhardness of as-implanted Si_3N_4 samples are shown in Fig. 11. The microhardness of the samples implanted with Mo ion decreased gradually with increasing implantation dose. The samples implanted with Y ion displayed different trend. Their microhardness increased with increasing implantation dose. There was no remarkable difference in microhardness of Mo ion implanted samples with different ion energies and ion current densities. But the microhardness change of both Mo ion and Y ion implanted samples exhibited different trends, as shown in Fig. 11. It seems that the change in microhardness of Si_3N_4 depends strongly on the ion species.

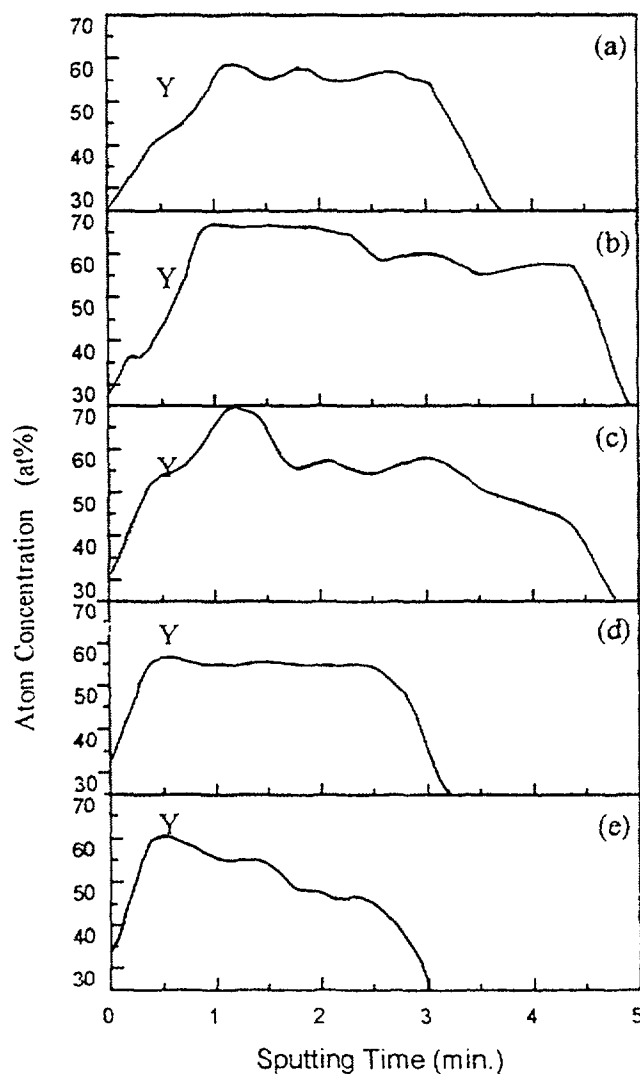


FIG. 9. SAM depth profiles: Y implantation with ion current density of $53 \mu \text{A}/\text{cm}^2$ (a) $2.0 \times 10^{17} \text{ ion}/\text{cm}^2$, (b) $6.0 \times 10^{17} \text{ ion}/\text{cm}^2$, (c) $10 \times 10^{17} \text{ ion}/\text{cm}^2$, (d) $14 \times 10^{17} \text{ ion}/\text{cm}^2$, (e) $18 \times 10^{17} \text{ ion}/\text{cm}^2$.

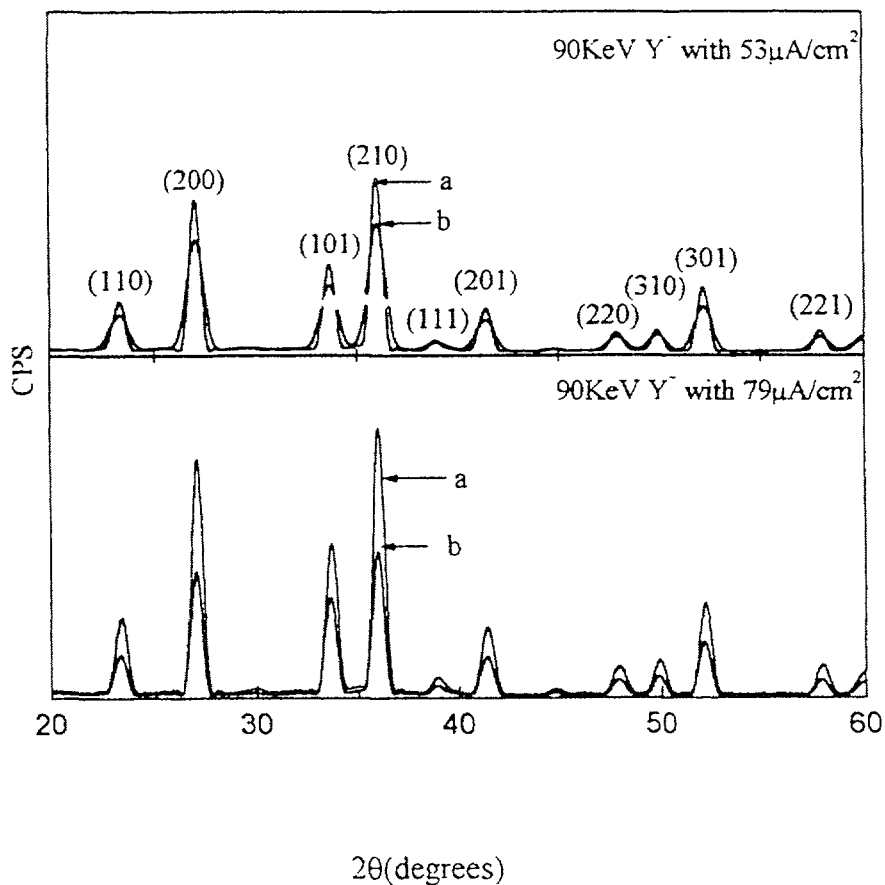


FIG. 10. X ray diffraction patterns of Si_3N_4 samples implanted with different ion dose. (a) 2×10^{17} ion/cm², (b) 18×10^{17} ion/cm², c) 14×10^{17} ion/cm².

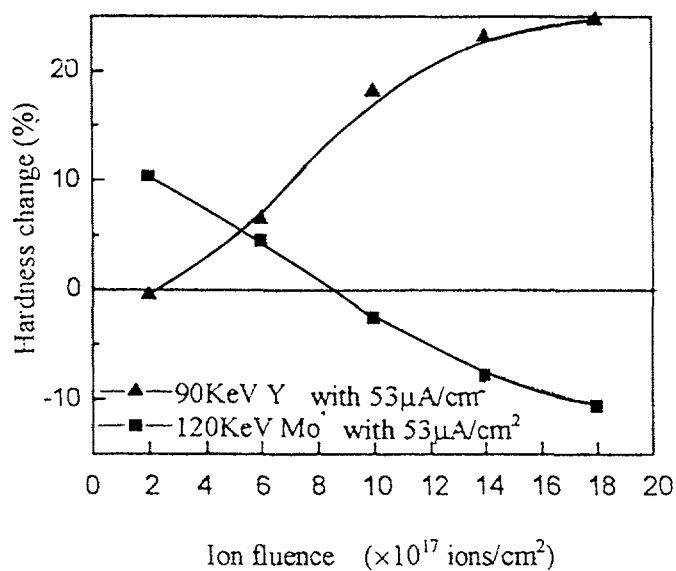


FIG. 11. Relative Vicker microhardness as a function of ion influence for Mo^+ and Y^+ implanted Si_3N_4 .

4.2.4. Sheet resistance

Silicon nitride is an insulator. After being implanted with Mo and Y ions, the silicon nitride samples became good electrical conductors. The sheet resistance of as-implanted Si_3N_4 samples was greatly decreased with increasing implantation dose because of surface metallization of Si_3N_4 ceramics, as shown in Table IV.

It can be seen that the samples implanted with Mo ion at low implantation energy of 120 keV were of low sheet resistance. A possible explanation is that the sputtering effect of implantation with 180 keV Mo ions was more serious than that of 120 keV Mo ions. The metallization layer of samples was peeled off from surface by later ions. This resulted in increase of the sheet resistance of 180 KeV samples. The samples implanted with Y ion at high ion current density of $79 \mu\text{A}/\text{cm}^2$ were of the low sheet resistance. During implantation process, diffusion and sputtering of implanted ions were related to implantation time. To get the same implantation dose, high ion current density will decrease implantation time. For the same dose, the implantation with ion current density of $79 \mu\text{A}/\text{cm}^2$ took only two third of time which was needed for implantation with ion current density of $53 \mu\text{A}/\text{cm}^2$. The samples implanted with high ion current density had a shorter diffusion and sputtering time, which made Y ions concentrate on the surface of samples and therefore the sheet resistance was lower.

4.2.5. Fracture toughness

The fracture toughness of as-implanted samples, determined by the Vickers indentation method increased gradually with increasing implantation dose (Fig.12). The maximum fracture toughness was obtained for the samples implanted with a dose of $14 \times 10^{17} \text{Mo}/\text{cm}^2$ at

TABLE IV. IMPLANTATION PARAMETERS, SURFACE TEMPERATURE AND SHEET RESISTANCE OF Si_3N_4 SAMPLES

Ion species	Ion energy (KeV)	Ion current density ($\mu\text{A}/\text{cm}^2$)	Dose ($\times 10^{17} \text{ion}/\text{cm}^2$)	Temperature (C)	Sheet resistance
Mo	180	53	2	530	464.3
	180	53	6	655	93.6
	180	53	10	700	3.6
	180	53	14	712	0.145
Mo	120	53	2	530	395.4
	120	53	6	655	87.8
	120	53	10	700	5.1
	120	53	14	712	0.127
Y	90	53	2	530	601.5
	90	53	6	655	60.7
	90	53	10	700	51.4
	90	53	14	712	11.8
Y	90	79	2	530	540.3
	90	79	6	655	51.6
	90	79	10	700	42.9
	90	79	14	712	5.21

180 keV. It was 35.9% higher than that of the control sample. Comparing the implantation parameters, ion energy seems to play an important role in the improvement of fracture toughness of Si_3N_4 . The implantation ion current density of Y ions does not seem to improve the fracture toughness. It is considered in general that improvement of fracture toughness of as-implanted samples is due to compressive stress resulting from ion implantation, and the compressive stress increased with increasing implantation dose.

4.3. PARTICLE MIGRATION IN THE NI/AL MULTILAYERS

The Ni/Al multilayer with alternating Ni (25 nm) and Al (36 nm) layers was sputter deposited on smooth silicon substrate using a Balzers Sputron Plasma System. The average composition of the multilayer was $\text{Ni}_{0.5}\text{Al}_{0.5}$ with a total thickness of 315 nm. After the deposition, the multilayer was ion treated at different temperatures, in the range between -145°C and $+430^\circ\text{C}$. Ion irradiation of NiAl multilayers was performed in a Balzers MPB 202 RR implanter using 350 keV Ar ions and a dose of 1×10^{16} Ar/cm².

4.3.1. Auger electron spectrometry (AES)

The Ni/Al multilayers were ion treated at different temperatures. All these samples were characterized with AES depth profiling. The PHI 545A scanning Auger microprobe with a

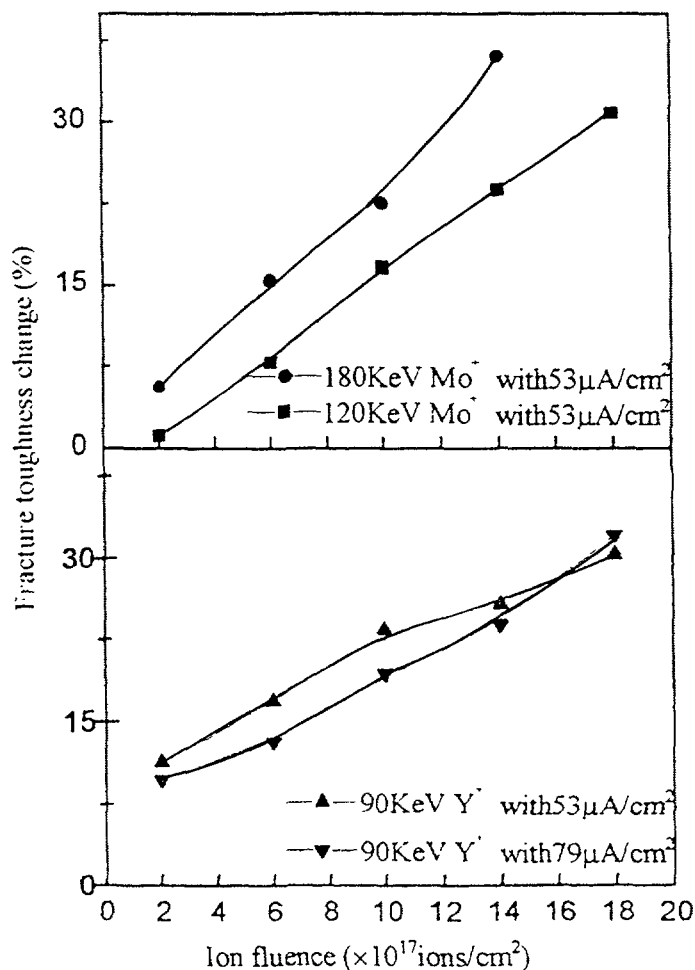


FIG. 12. Relative indentation fracture toughness as a function of ion influence for Mo^+ and Y^+ implanted Si_3N_4 .

static primary electron beam of 3 keV, 1 μ A and a diameter of about 40 μ m was used. The samples were ion sputtered by using two symmetrically inclined ion guns. The ion incidence angle was 47° with respect to the normal to the sample surface. The samples were ion sputtered with 1keV Ar⁺ ion beam, rastered across an area of 10 \times 10mm².

Fig. 13a shows the AES depth profile of the as-deposited Ni/Al multilayer with an average composition of Ni_{0.5}Al_{0.5}. Ni is present in the Al thin films even though the sample temperature during the deposition of Ni/Al multilayer was less than 100°C. We therefore conclude that Ni is the main moving element in the early stage of diffusion. However, despite high depth resolution provided by two ion guns, it is not possible to exclude topographic effect completely as they might cause a slight loss of depth resolution especially in the Al thin films.

The AES depth profile of the Ni/Al multilayers ion mixed at two different temperatures of -145°C (Fig. 13b) and 25°C (Fig. 13c) shows almost the same concentration profiles. In both cases the migration of Ni and Al atoms is only enhanced by 350 keV Ar ion mixing. As expected, the thermally activated diffusion processes are negligible up to the room temperature. However, the effect of ion beam mixing is increased by thermally activated migration already in the sample heated at 130°C (Fig. 13d) and especially at higher temperatures of 230°C (Fig. 13e), 280°C (Fig. 13f), 330°C (Fig. 13g) and 430°C (Fig. 13h). Generally, temperature effect of ion beam mixing increased with increasing temperature. The periodicity of the Ni and Al concentration profiles is lost in the samples isothermally heat treated during ion mixing at 280°C and 330°C respectively. The ion mixing and diffusion process enhanced the migration of Ni and Al atoms and accelerated the formation of NiAl solid solutions. The Ni/Al sample heated at 430°C show the completely reacted NiAl layer with the composition of about 55.0 at% Al and 45.0 at% Ni.

A detailed observation of the interface widths revealed different migration lengths of Ni and Al atoms at the Ni/Al and Al/Ni interfaces in the ion and heat-treated Ni/Al multilayer structures. The interface width was extracted from the amplitudes of the profile. The longer migration lengths were observed at the Al/Ni (Fig. 14a) than at the Ni/Al interfaces (Fig. 14b) located inside of the Ni/Al multilayer. This is the consequence of higher diffusion rate of Ni than Al atoms and of the ion range, which was estimated to be 180 nm with the TRIM 95 code. With increasing temperature the interface widths increased additionally due to thermally enhanced diffusion of Ni and Al atoms (Fig. 15).

4.4. INVESTIGATION OF INTERACTION OF GASEOUS IONS WITH GETTER MATERIAL

Samples of pure Ti plates were polished and exposed to a flux of nitrogen, oxygen and methane ions with the kinetic energy of 100 keV per molecule. The ion doses were 5 \times 10¹⁶, 1 \times 10¹⁷, 2.5 \times 10¹⁷, 5 \times 10¹⁷, 7.5 \times 10¹⁷ and 1 \times 10¹⁸ atoms/cm². The ion implantation was performed at the Institute of Electronic Material Technology, Warsaw, Poland. The composition of the surface layer on the samples has been determined with the AES method. Depth profiles have been obtained for both the ion implanted samples at room temperature and the samples implanted at 400°C. Samples were then exposed to weakly ionized highly dissociated hydrogen or oxygen plasma, which was created by RF generator with the frequency of 27.12 MHz and the power of 300W. Hydrogen plasma with electron temperature of 6eV, density of charged particle of 10¹⁶ m⁻³, plasma potential of 20V and the Debye length of the order 10⁻⁴m was generated at the pressure of 100 Pa. Oxygen plasma with the electron

temperature of 8eV, density of charged particle of $5 \times 10^{15} \text{ m}^{-3}$, plasma potential of 30V and the Debye length of the order 10^{-4} m was generated at the pressure of 40 Pa.

Composition of the surface layer of samples treated at room temperature at different nitrogen and oxygen ion doses is shown in Fig. 16 and Fig. 17. The depth profile of the Ti sample implanted with nitrogen followed by exposure to oxygen plasma for 20 seconds is

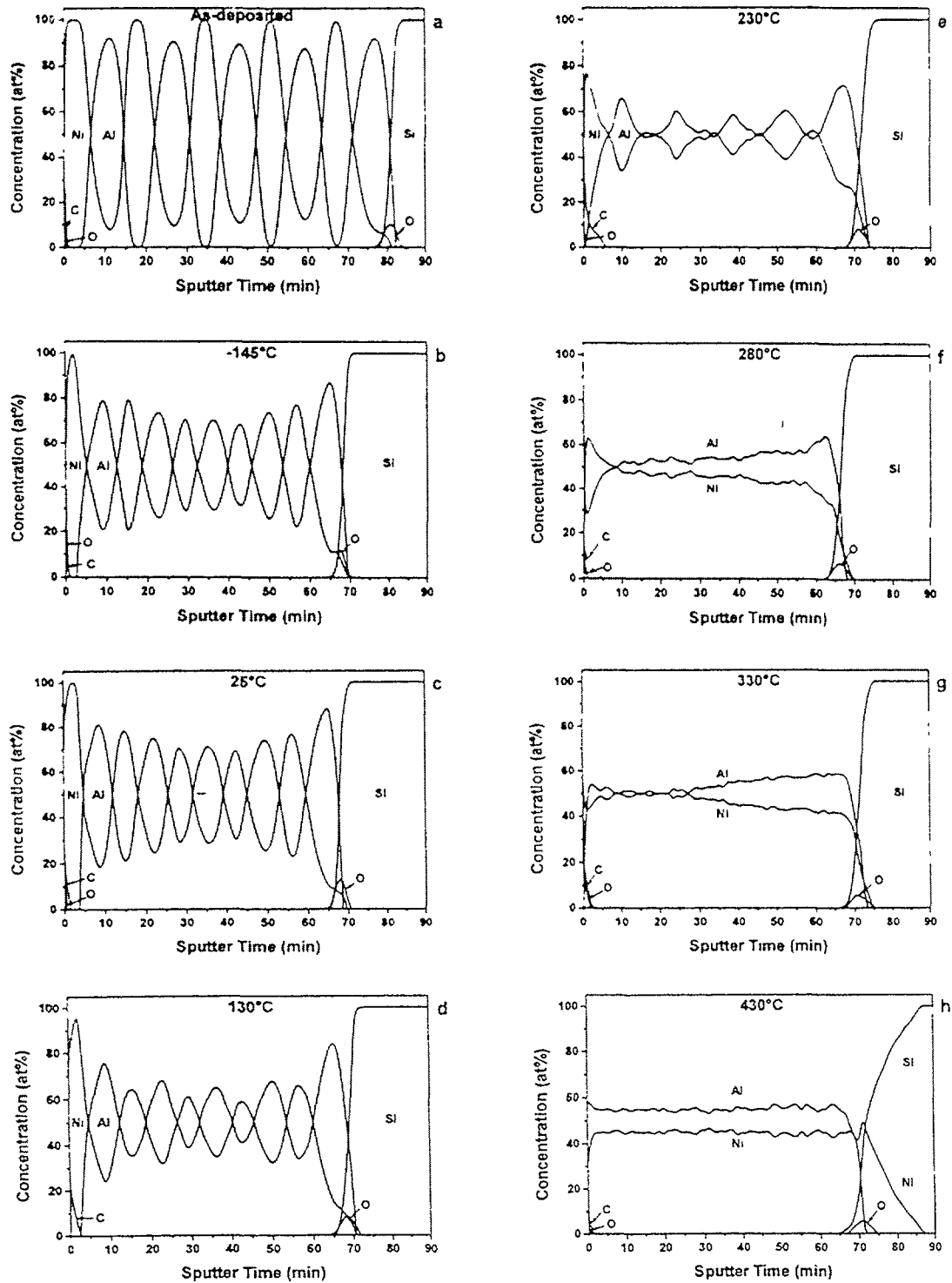


FIG. 13 *a, b, c, d, e, f, g, h*: AES depth profiles of an as-deposited Ni/Al multi-layer structure with an average composition of $\text{Ni}_{0.50}\text{Al}_{0.50}$ under dose of $1 \times 10^{16} \text{ ion/cm}^2$ at different temperatures, between (b) -145°C (h) $+430^\circ\text{C}$.

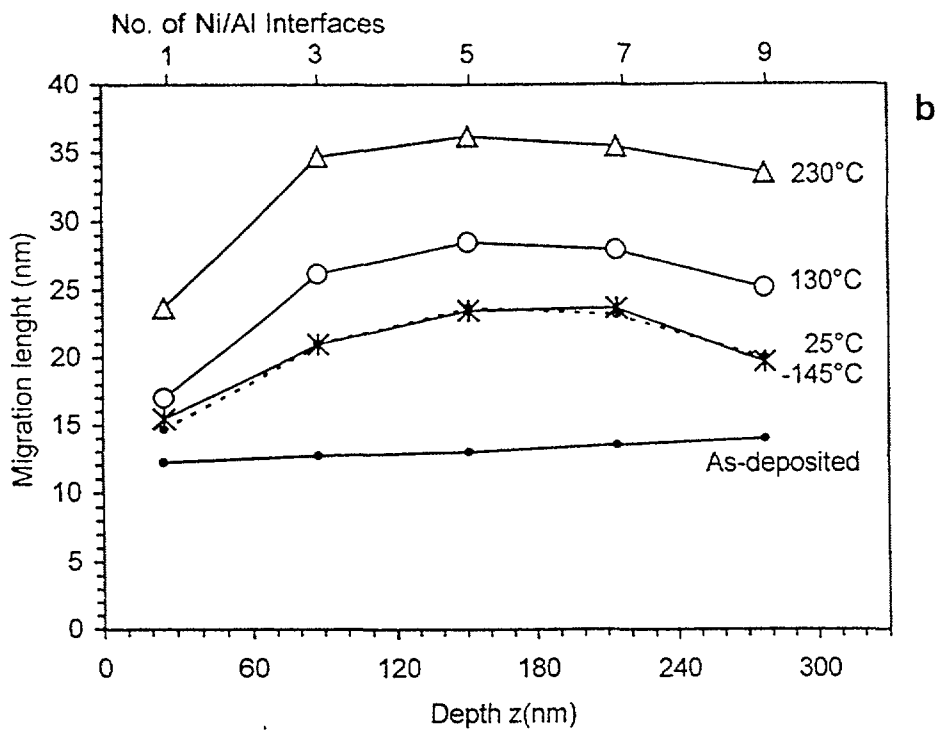
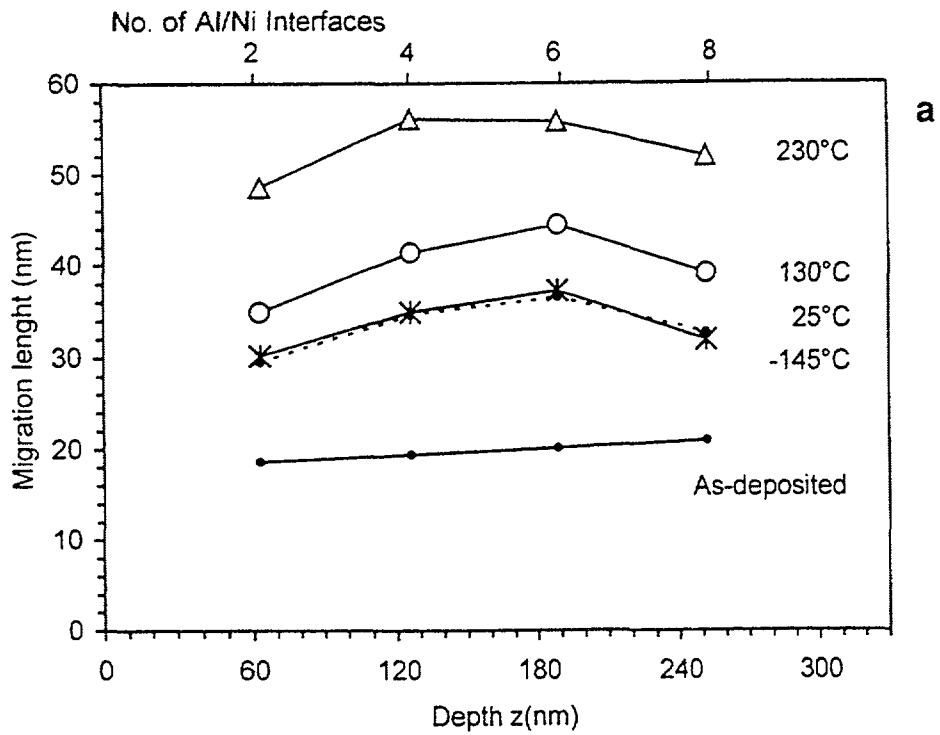


FIG. 14. Migration lengths of Ni and Al atoms (a) at the Al/Ni and (b) at the Ni/Al interfaces.

shown in Fig. 18 while that of samples of Ti implanted with oxygen and exposure to hydrogen plasma for 100 s in Fig. 19. Samples of titanium compounds were also prepared by interaction of low pressure Penning discharge with Ti substrate. A typical depth profile of the cathode and anode of the discharge cell is shown in Fig. 20 and Fig. 21 respectively. Hydrogen distribution within the coating is shown in Fig. 22.

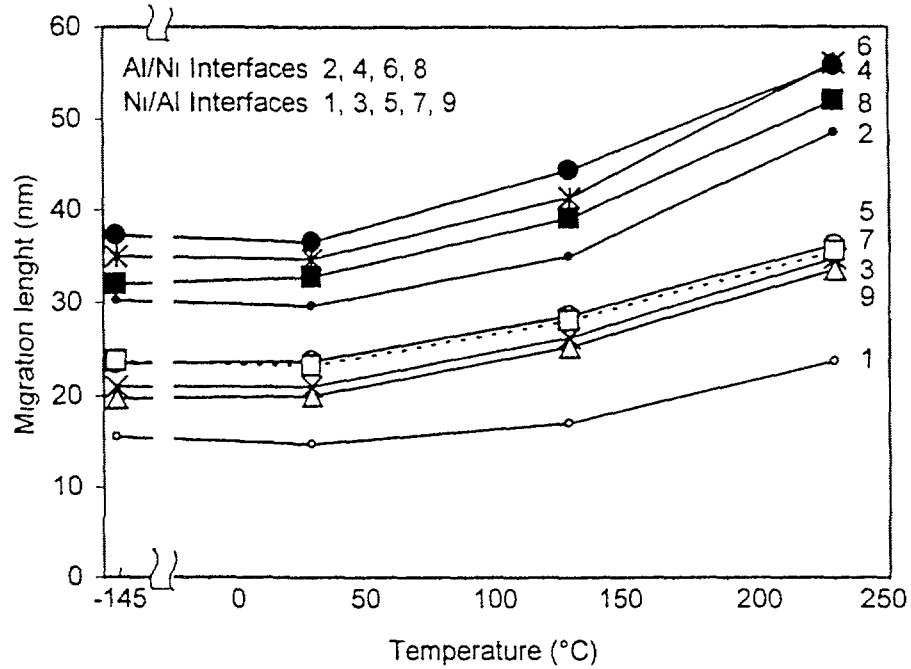


FIG 15. Dependence of migration length of atoms on temperature at the Al/Ni and Ni/Al interfaces.

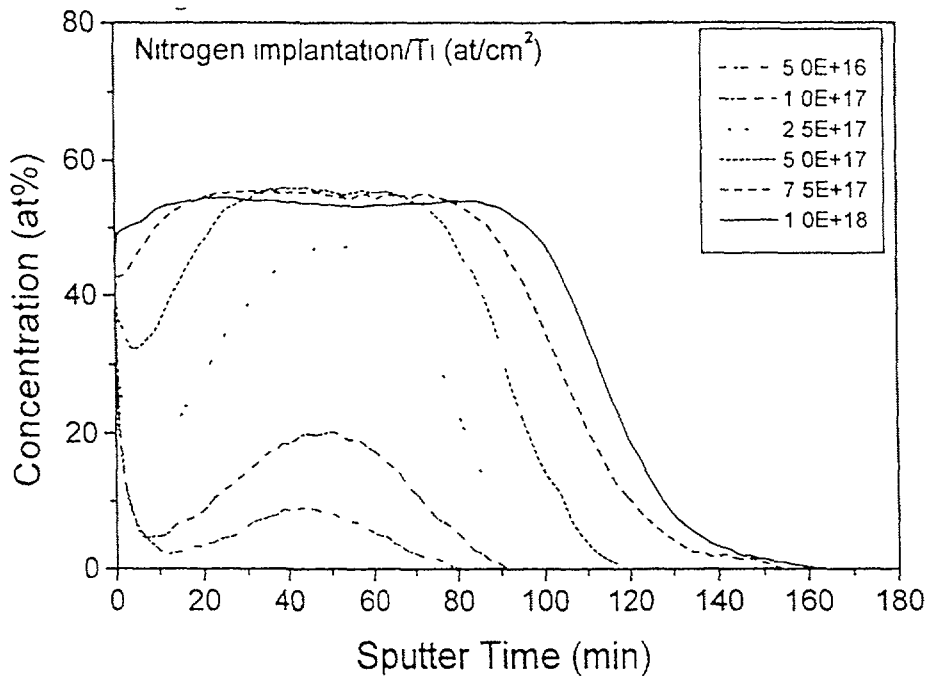


FIG 16 AES depth profiles of titanium samples ion implanted with 100 keV nitrogen molecules with different doses

4.5. FORMATION OF THICK, NITROGEN RICH LAYER

Depositions of thick nitrogen rich layer on steel samples were achieved by a special procedure, combining nitrogen implantation with post-implantation annealing. This procedure is based on the assumption that the nitride precipitates formed during post-implantation annealing may act as traps for migrating nitrogen atoms implanted at elevated temperatures.

The proposed procedure assumes the use of a typical ion implanter i. e. a machine delivering a non-separated nitrogen beam with energy up to 150 keV. The procedure is composed of four steps: pre-implantation, formation of ϵ -Fe_{3-x}N precipitates, their transformation into γ' -Fe₄N phase, and post-implantation at elevated temperatures which leads to a growth of γ' -Fe₄N precipitates ensuring the increase of the thickness of doped layer. The final process parameters are listed in Table V.

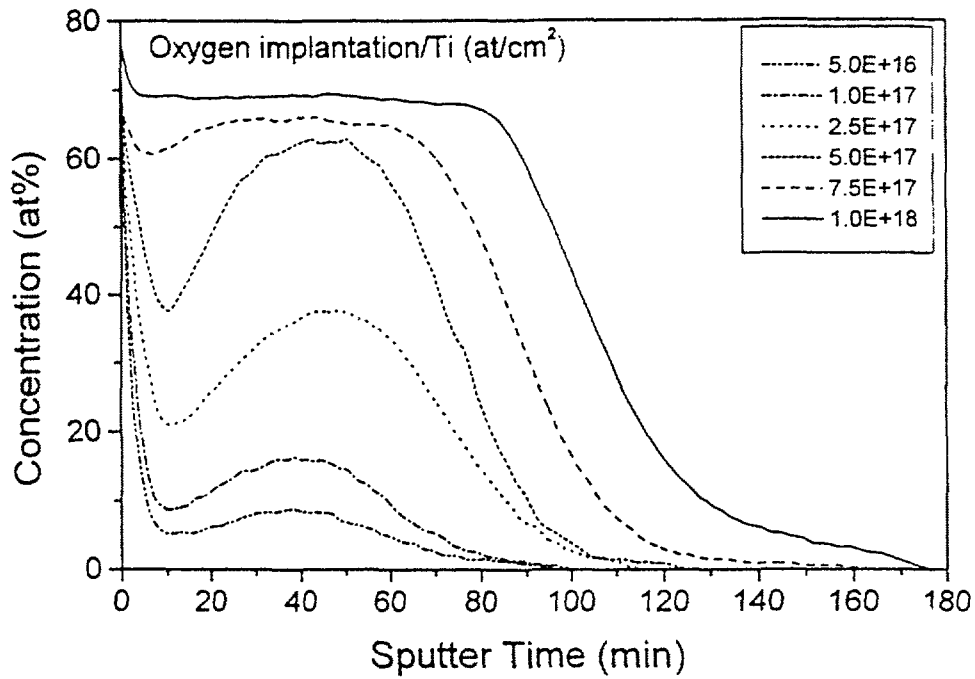


FIG. 17. AES depth profiles of titanium samples ion implanted with 100 keV oxygen molecules with different doses.

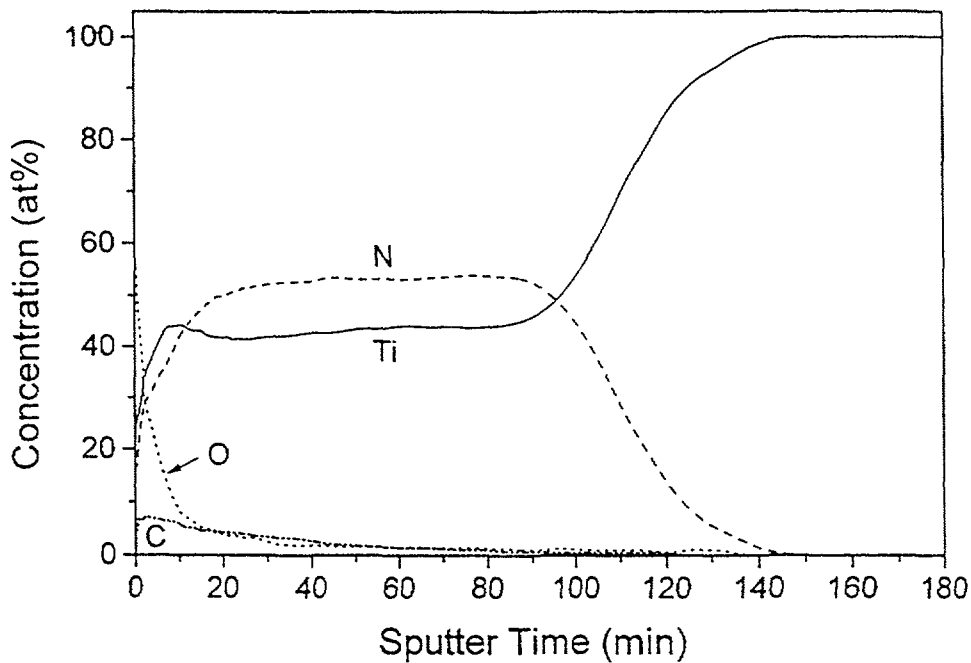


FIG. 18. AES depth profiles of titanium samples ion implanted with 100 keV nitrogen molecules at the dose of 1×10^{18} atoms/cm².

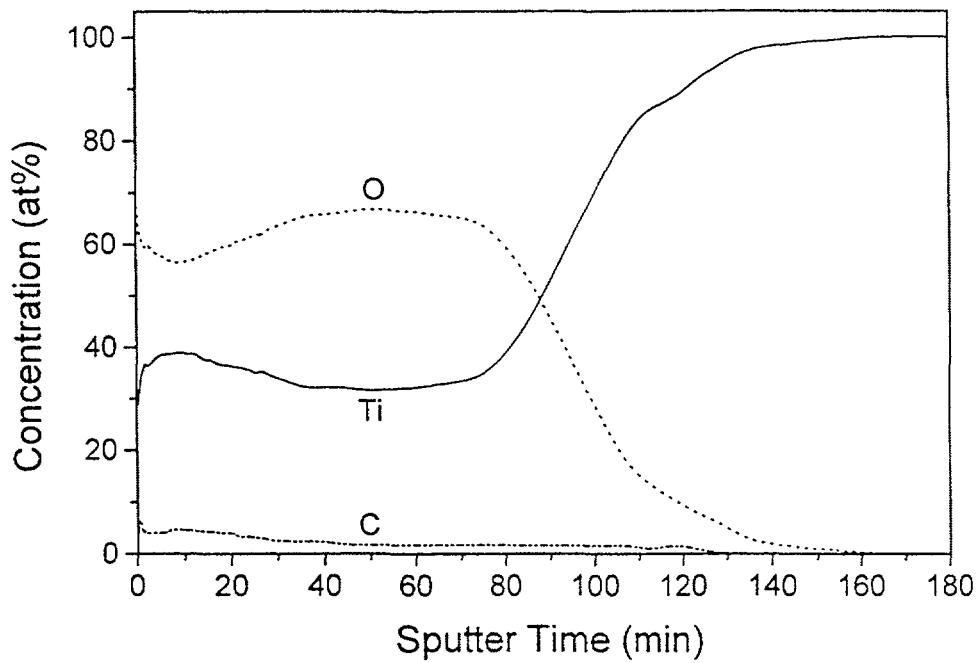


FIG. 19. AES depth profiles of titanium sample ion implanted with 100 keV oxygen molecules at the dose of 1×10^{18} atoms/cm².

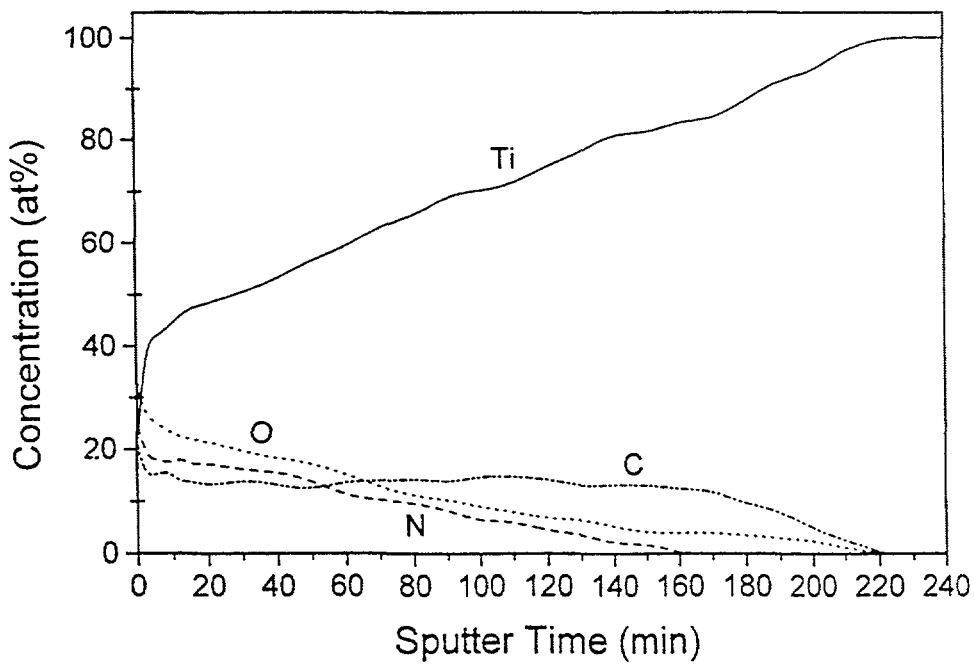


FIG. 20. AES depth profile of a coating of Ti compounds prepared on the cathode of the Penning discharge cell.

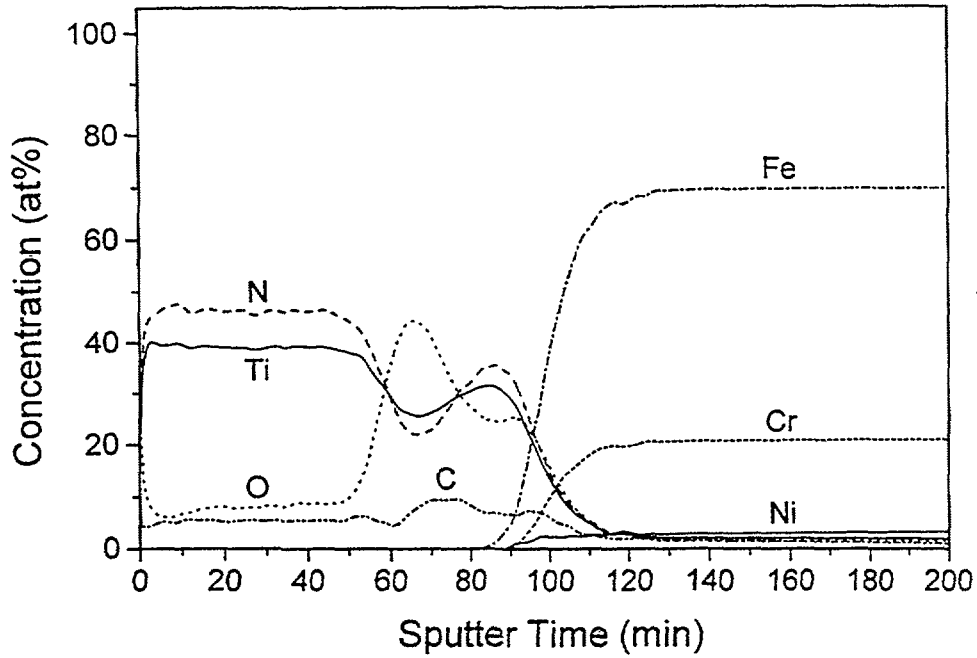


FIG. 21. AES depth profile of a coating of Ti compounds prepared on the anode of the Penning discharge cell.

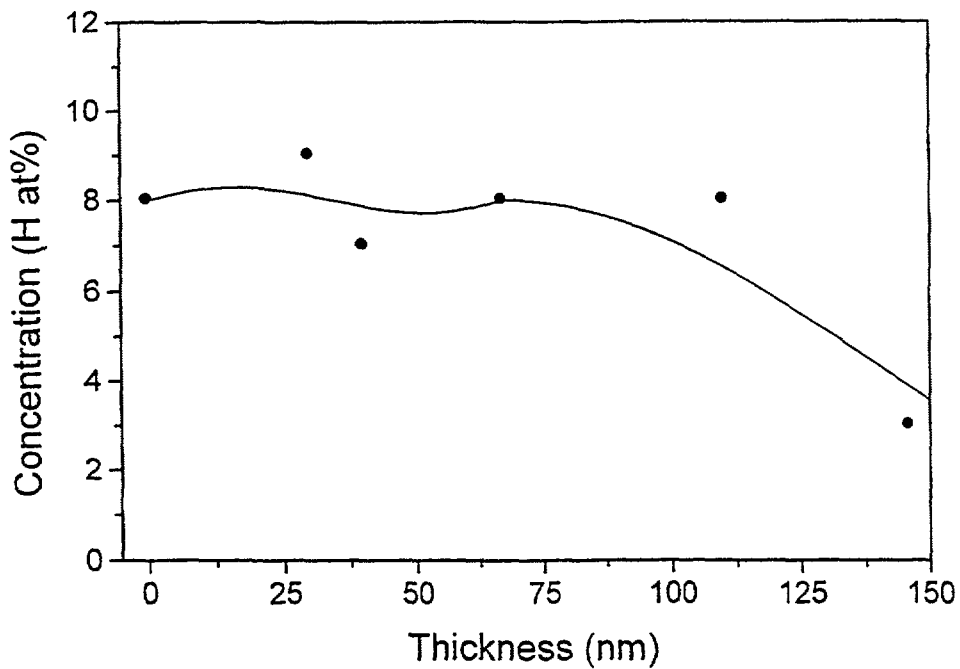


FIG. 22. Hydrogen concentration in the surface layer of the cathode of a Penning cell.

TABLE V. DESCRIPTION OF THE SAMPLE PREPARATION

Step	Process description
a) 1 st implantation	$2.1 \times 10^{17} \text{ N}_2^+$, 150 keV, RT
b) Annealing	200°C 1h + 250°C 1h + 300°C 1h
c) Post-annealing	350°C, 4.5h
d) 2 nd implantation	$2 \times 10^{17} \text{ N}_2^+$, 70 keV, 200°C

4.5.1. Wear test

The wear tests were performed using a ball-on-flat tribotester with a 6.5 mm steel ball as counter sample. The nominal load was equal to 20N, stroke was set to 3 mm and the average speed of translation amounted to 3.34 mm/s. The results of friction measurements are presented in Fig. 23. The results obtained point to significant increase of friction coefficient with processing temperature. This is especially important in the case of post-implantation carried out at 200⁰C or 300⁰C. The value of friction coefficient measured on the samples implanted at elevated temperatures exceeds even the value recorded for the untreated HSS steel samples ($f_s \sim 0.8$).

4.6. FORMATION OF THICK, WEAR-RESISTANT METALLIC LAYERS VIA ION BEAM MIXING TECHNIQUE

Deposition of wear resistant metallic layer on high speed steel samples covered with Al, Si, Mo, and W were carried out by ion beam mixing method. The mixing processes were carried out at temperatures ranging from room temperature to 350⁰C. The final process parameters are listed in Table VI.

4.6.1. Auger electron spectrometry (AES)

The depth distributions of doping elements before and after ion beam mixing process carried out at room temperatures are shown in Fig. 24. One can note that the impurity profiles extend from the interface to the depth of few hundred angstroms, i.e. the depth comparable to the projected range of implanted atoms in typical medium energy process. The increase of process temperature does not result in significant increase of the thickness of impurity rich layer but rather in the increase of impurity concentration.

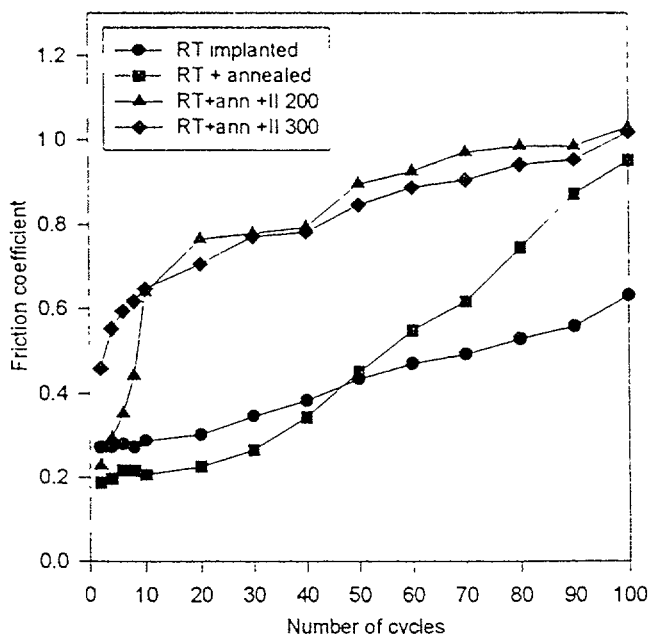


FIG. 23. Friction coefficient changes during wear test.

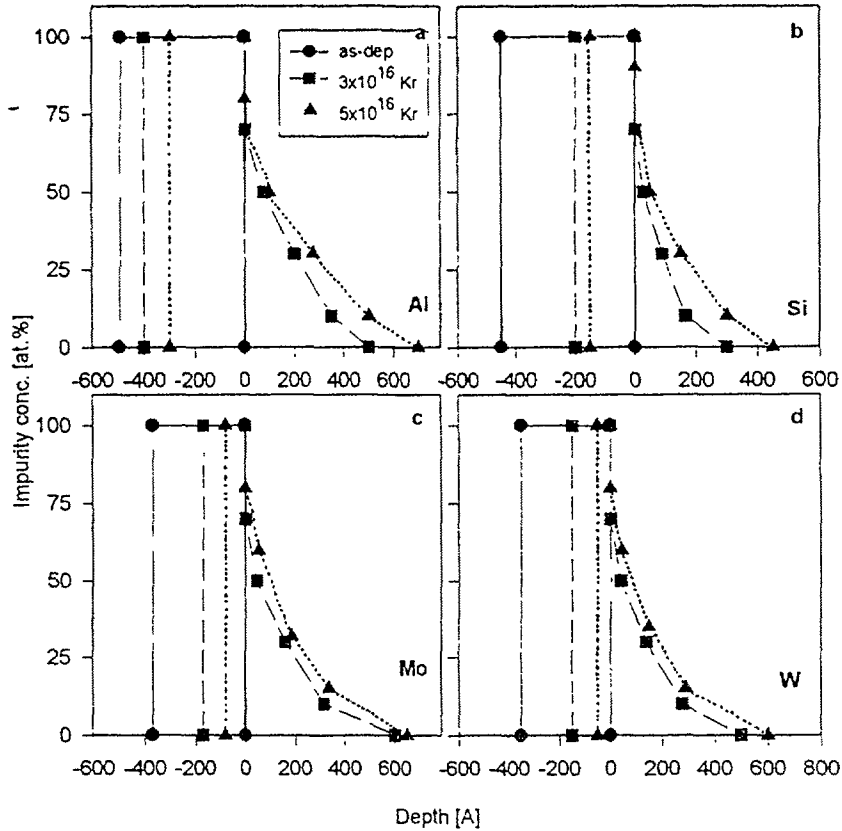


FIG. 24. Depth distribution profiles after ion beam mixing of various elements deposited on the surface of HSS samples.

TABLE VI. EXPERIMENTAL PARAMETERS

No.	Layer material	Layer thickness (nm)	Bombarding ion	Ion energy (keV)	Irradiation dose	Temp. °C
1	untreated	-	-	-	-	-
2	Al	45	Kr	150	5×10^{16}	RT
3	Si	45	Kr	150	5×10^{16}	RT
4	Mo	45	Kr	350	5×10^{16}	RT
5	W	45	Kr	350	$3-5 \times 10^{16}$	RT
6	W	45	Kr	350	3×10^{16}	250°C
7	W	45	Kr	350	3×10^{16}	350°C

4.6.2. Wear and friction test

These tests were carried out using a ball-on-flat tribometer, with a 6.5 mm dia. ball oscillating on the sample surface. The tangential force was measured during the test allowing the determination of friction coefficient. The load of 20N was used and the sliding speed was equal to 3.34 mm/s. The tests were performed in air up to 100 or 200 oscillations. After tests, the samples were analysed by scanning electron microscopy and the wear trace profiles were measured by Taylor-Hobson 3D profilometer. The results of friction measurements performed on ion beam mixed samples are presented in Fig. 25. The results obtained for the samples implanted with combination of Ti and C are included for comparison. It was observed that the

coefficient of friction decreased significantly for all ion beam mixed samples. The lowest value of ~ 0.2 were measured for W covered, Kr ion beam mixed samples. This value is comparable to the combined Ti + C implantation. The role of the process temperature was studied in the case of W layers. The results of friction measurements are shown in Fig. 26, which indicate that friction coefficient increase with the irradiation temperature.

The analysis of the mixed layer structure performed by combination of CEMS and GXR techniques indicated that, after ion beam mixing at room temperature, the structure of the layer is amorphous. The SEM images taken for the samples irradiated at 258°C or 350°C

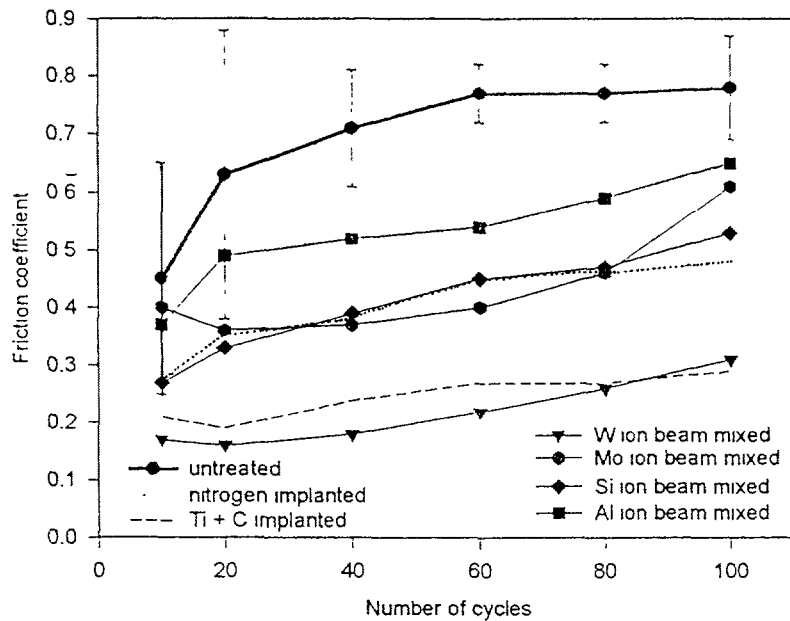


FIG. 25. Friction coefficient dependence on the number of cycles measured in ball-on-flat test for various samples.

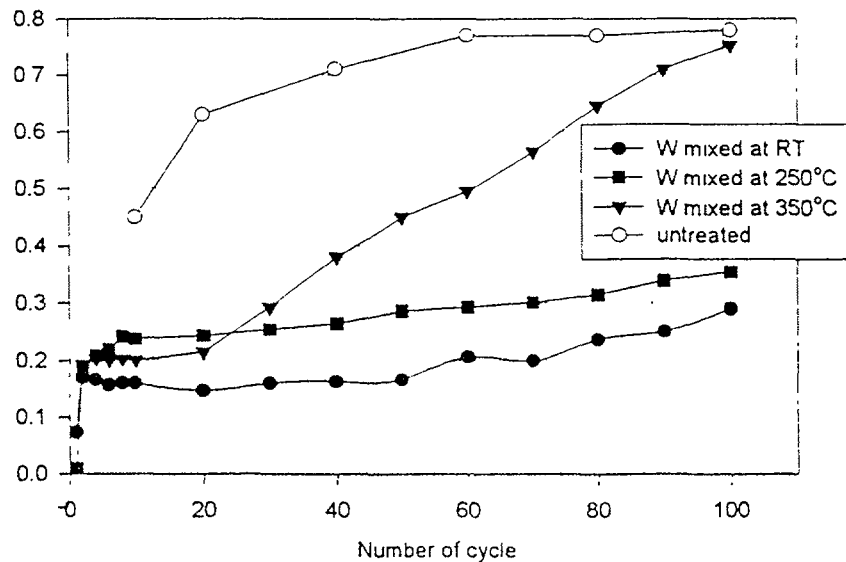


FIG. 26. Friction coefficient measured for the samples covered with W layer and ion-beam mixed at Rt , 250°C and 350°C .

revealed a granular structure of the surface layer indicating, that after ion beam mixing at elevated temperatures the layer structure is at least partially crystalline.

4.7. N AND B ION IMPLANTATION ON SKD 11 STEEL

Seven types of hardened or unhardened steels were chosen to be sample materials. All sample surfaces had a final polishing with 0.3 μ alumina powder. For N ion implantation, molecular nitrogen ions with an energy of 90 keV were selectively implanted into the steel samples to a fluence of $4 \times 10^{17} \text{ N}^+/\text{cm}^2$ with a high beam current density of 200–300 $\mu\text{A}/\text{cm}^2$. Following the N_2 -ion implantation 33-keV B ions were subsequently implanted to a fluence of $2 \times 10^{17} \text{ B}^+/\text{cm}^2$ using a low beam current density ($<50 \mu\text{A}/\text{cm}^2$). Hardness and wear tests were performed on the as-implanted samples.

4.7.1. Hardness

Hardness testing was performed using Digital microhardness tester with a load of 5 gram. The hardness results (Table VII) show that N ion implantation increases microhardness for all the tested steels. Steel with a higher chromium content, such as SKD 11 shows larger increase in hardness, which is probably due to super hard Cr-N formation. Steels with a lower Cr content after heat treatment generally exhibit less increase in hardness than those of unhardened ones. Additionally B ion implantation improves hardness for the hardened steels, but not for unhardened steels.

4.7.2. Wear and friction test

Wear test on SKD 11 samples were performed with a pin-on-disk tribometer. Two types of ball bearings were used. They are: (1) SKF3 rolling bearing steel (HK~ 800), 4.9 mm in diameter, and (2) WC (HK~ 2000), 6.3 mm diameter. The former was applied for testing the unhardened steel samples using a load of 150 gm, while the latter was for testing both unhardened and hardened samples but using a load of 500 gm. The typical sliding speed was about 5 cm/s, and the total number of sliding cycles were more than 104 for each test. The results of wear test are also given in Table VII, which show that ion implantation improves wear resistance of all types of steels, with the wear rate decreasing approximately by a factor of 2 to 4. Wear resistance increases with increasing hardness, but steels that are not heat treated are superior to heat-treated steels of the same hardness as shown by the values of $\text{HK} \times (\text{wr})$. However, our scanning high-density beam ion implantation can improve wear resistance of the hardened steels comparably to the unhardened steels, as shown by the similar values of $(\text{wr})/(\text{wr})_0$ between the hardened and unhardened steels (Table VII). Heat-treated but unhardened steels, such as S45C and SCM440, still showed improvement in wear resistance from ion implantation more than the steels without heat treatment, as seen in Table VII. Improvement in tribological properties has been found to depend on Cr content for high C tool steels, such as M-SKD11, SKD11 and SKS3, as the higher Cr steels (M-SKD11 and SKD11) have a greater reduction in wear rate than the lower Cr steel (SKS3). Improvement in wear resistance due to ion implantation is more pronounced under the wear condition of hard ball with heavy load than under the condition of soft ball with light load, as indicated by the data shown in Table VIII. For assessment of the wear behaviour, a ratio is defined by $n = w/d$, where w is the width of the wear scar and d is the diameter of the ball bearing worn area. The value of n reflects the wear-resistance of a disk material against a ball material, the lower the n value, the higher the resistance. It is clear from Table VIII that under the condition of hard ball with heavy load n decreases obviously more than under the condition of soft-ball with light load. More adhesive wear is observed in the latter condition than in the former, where

abrasive wear dominates, as exhibited in Fig. 27. This is understandable due to the similar materials in contact and more ductility of the soft ball. Mixing B ions to implanted N ion layers seems to play a role in promotion of wear resistance even though sometimes it does not harden the materials, as seen in Table VII.

4.7.3. Friction

No noticeable change in the friction coefficient was observed between unimplanted and implanted samples for either hardened or unhardened steels, partially in agreement with the previous survey of friction behaviour, but only under the wear condition of hard ball with heavy load as shown in Fig. 28a and Fig. 28b. It may be interpreted that more adhesive wear is involved in the harder materials (implanted) than in the softer ones (unimplanted) that is dominated by abrasive wear. Under the wear condition of softball with light load, the friction coefficient is generally increased by ion implantation, as shown in Fig. 28c. The reason can be attributed to more loss in ball volume caused by the ion implantation hardened steel disk surface.

4.8. N ION IMPLANTATION ASSISTED BY PREPARATIVE AND CLOSING IMPLANTATION FOR SURFACE MODIFICATION OF TOOL STEEL

Samples of hardened SKD11 (AISI D-2) steel with well finished surface were implanted with higher-energy N ions or Ar ions, followed with 120-keV N₂ ion normal implantation, and finally implanted with lower-energy BF₃ or N₂ or CO₂ ions (as summarized in Table VIII).

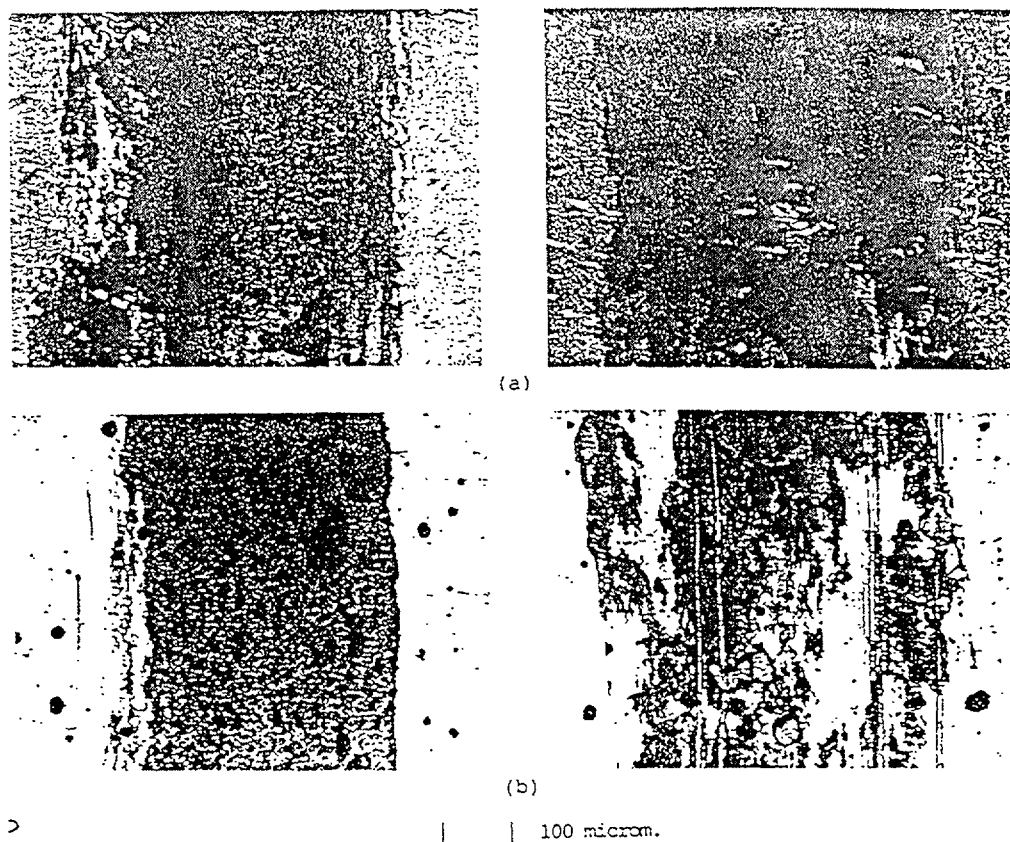


FIG. 27. Micrographs of wear tracks under different wear testing conditions.

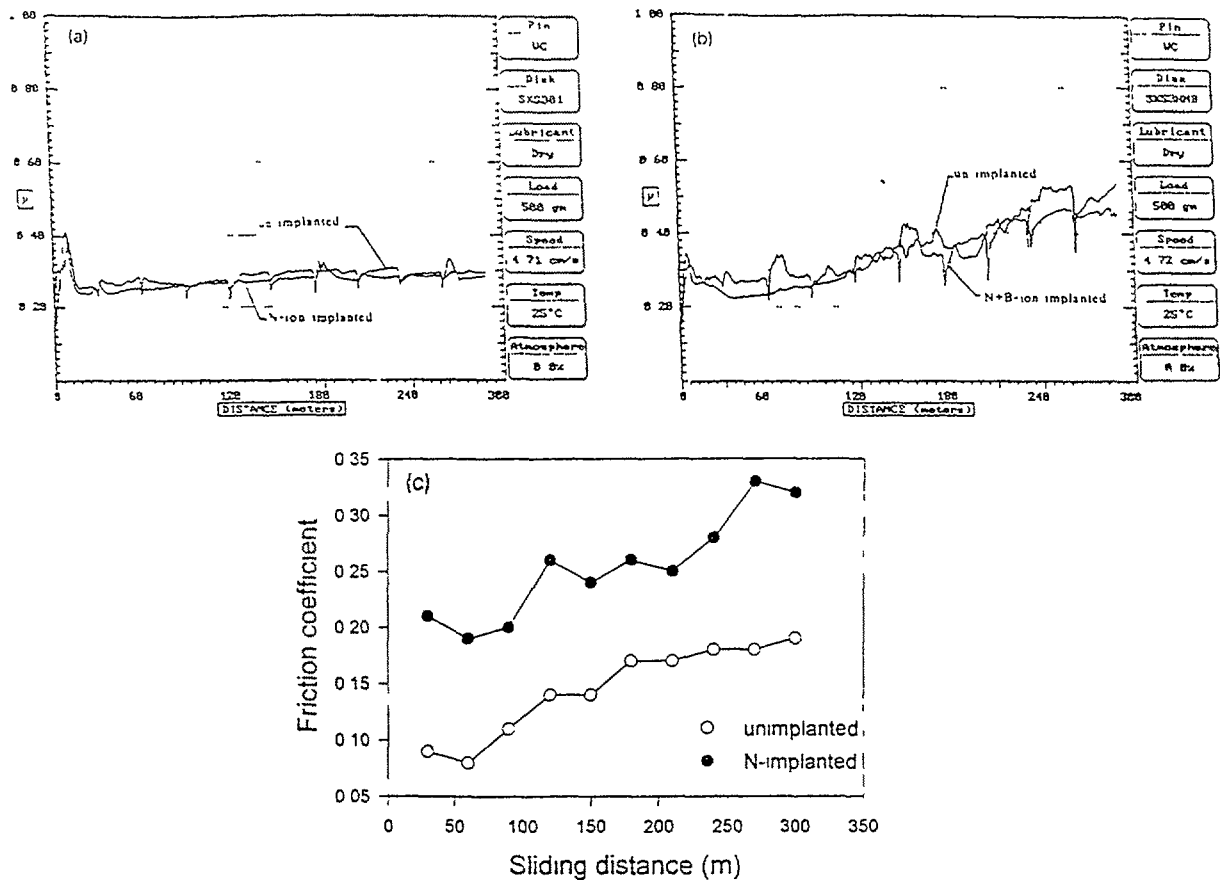


FIG. 28. Friction coefficient of (a) steel: SKS3, unheated, ball: WC, load: 500 gm; steel: SKS3, heated, ball: WC, load: 500 gm; c) steel: SKS3, unheated, ball: WC, load: 150 gm.

4.8.1. Auger electron spectrometry (AES)

The ion depth profiles of implanted samples were analyzed using AES method, as shown in Fig. 29. The preparative and closing ion implantations generally tend to broaden and deepen the nitrogen distributions. In the case of $N+N_2 + N_2$ ion implanted samples the PROFILE-simulations show a depth up to 200nm (Fig. 29a) while the measured profile (Fig. 29b) is flat and extends to a depth of more than 600nm. Other profiles display similar behaviour. The effect of broadening and deepening ion profiles seems very beneficial in achieving the lasting low wear rates. It can be seen that the closing B ion implantation leads partly to the migration of normally implanted N ions to the B ion region, as shown in Fig. 29c and e, while the closing CO_2 ion implantation causes the normally implanted N ions to be pushed further into the substrate (Fig. 29d). This fact implies that the implanted boron has a stronger affinity of bonding with the formerly implanted nitrogen than the carbon and oxygen have (correlated with the XRD result) as shown in Fig. 30. Therefore, the $N + N_2 + BF$ ion implantation produces a lower wear rate than the $N + N_2 + CO_2$ ion implantation. For the case of $Ar + N_2 + BF$ ion implantation, it is assumed that radiation damage induced by the preparative Ar ion implantation makes the N ions migrate more easily to the near surface region, so that the N ion distribution is shallower (Fig. 29e) than those in other cases. Therefore the low wear rate can not last and the average wear rate becomes high.

TABLE VII. MICROHARDNESS AND WEAR RATE (UNDER THE WEAR CONDITION OF WC BALL WITH 500 G LOAD) OF THE STEELS UNDER VARIOUS STATES. $\Delta HK = HK - HK_0$, $HK =$ THE KNOOP HARDNESS NUMBER, AND HK_0 : THE HARDNESS OF UNIMPLANTED SAMPLES. (WR): THE MEAN WEAR RATE OVER THE TOTAL SLIDING DISTANCE, AND $(WR)_0$: THE (WR) OF UNIMPLANTED SAMPLES

Steel	State	Ion implantation	Knoop hardness		Wear rate		$HK \times wr$ ($10^{-6}kg$)
			HK (Kg/mm^2)	$\Delta HK/HK_0$ (%)	wr ($10^{-6}mm^2$)	wr/wr_0	
Modified SKD11	untreated	-	266	0	0.30	1	80
		N	352	32	0.18	1/1.7	63
		N+N+B	794	200	0.11	1/2.7	87
	treated	-	676	0	0.16	1	108
		N	895	21	0.10	1/1.6	90
		N+N+B	1046	55	0.09	1/1.8	94
SKD11	untreated	-	250	0	0.50	1	125
		N	371	48	0.20	1/2.5	74
		N+B	348	39	0.14	1/3.6	49
	treated	-	519	0	0.25	1	130
		N	818	58	0.10	1/2.5	82
		N+B	874	68	0.10	1/2.5	87
SKS3	untreated	-	244	0	0.23	1	56
		N	295	21	0.17	1/1.4	50
		N+B	298	22	0.12	1/1.9	36
	treated	-	510	0	0.12	1	61
		N	620	22	0.09	1/1.3	56
		N+B	648	27	0.08	1/1.5	52
S45C	untreated	-	248	0	0.39	1	97
		N	312	26	0.14	1/2.8	44
		-	286	0	0.57	1	163
	treated	-	336	17	0.17	1/3.4	57
		N	341	0	0.47	1	163
		N	428	26	0.17	1/2.8	73
SCM440	untreated	-	317	0	0.61	1	193
		N	356	12	0.15	1/4.1	53
		-	245	0	0.27	1	66
SCM415	untreated	-	317	29	0.13	1/2.1	41
		N	459	0	0.20	1	92
		N	557	21	0.11	1/1.8	61

4.8.2. Hardness

The surface hardness is tested using a digital microhardness tester by applying a load varying from 1 g to 50 g. Table IX shows the measured hardness and the derived wear rate of the ion implanted samples compared with temperature data of the unimplanted sample. Figure 31 shows the microhardness tested with varying load. The preparative-plus-closing ion implantation increases the hardness drastically in comparison with the single and double ion implantations. The effect of the preparative implantation depends on the ion species. Nitrogen performs better than argon owing to the fact that the N ions are able to cause both radiation damage and structural strengthening whereas the Ar ions create only damage. The effect from the closing implantation seems to be more pronounced than the preparative implantation.

Proper selection of the closing implanted ion species, such as boron, carbon or oxygen ions, can result in a larger enhancement of hardness than nitrogen. It is interesting to note that, at the lowest load, all the preparative-plus-closing ion implantations increase the hardness relatively higher than other implantations do, as shown by the steeper slopes between the hardness with loads of 1 g and 3 g for the triply implanted samples (Fig. 31). This fact indicates that the triple ion implantation is more effective in improving nearest-surface hardness.

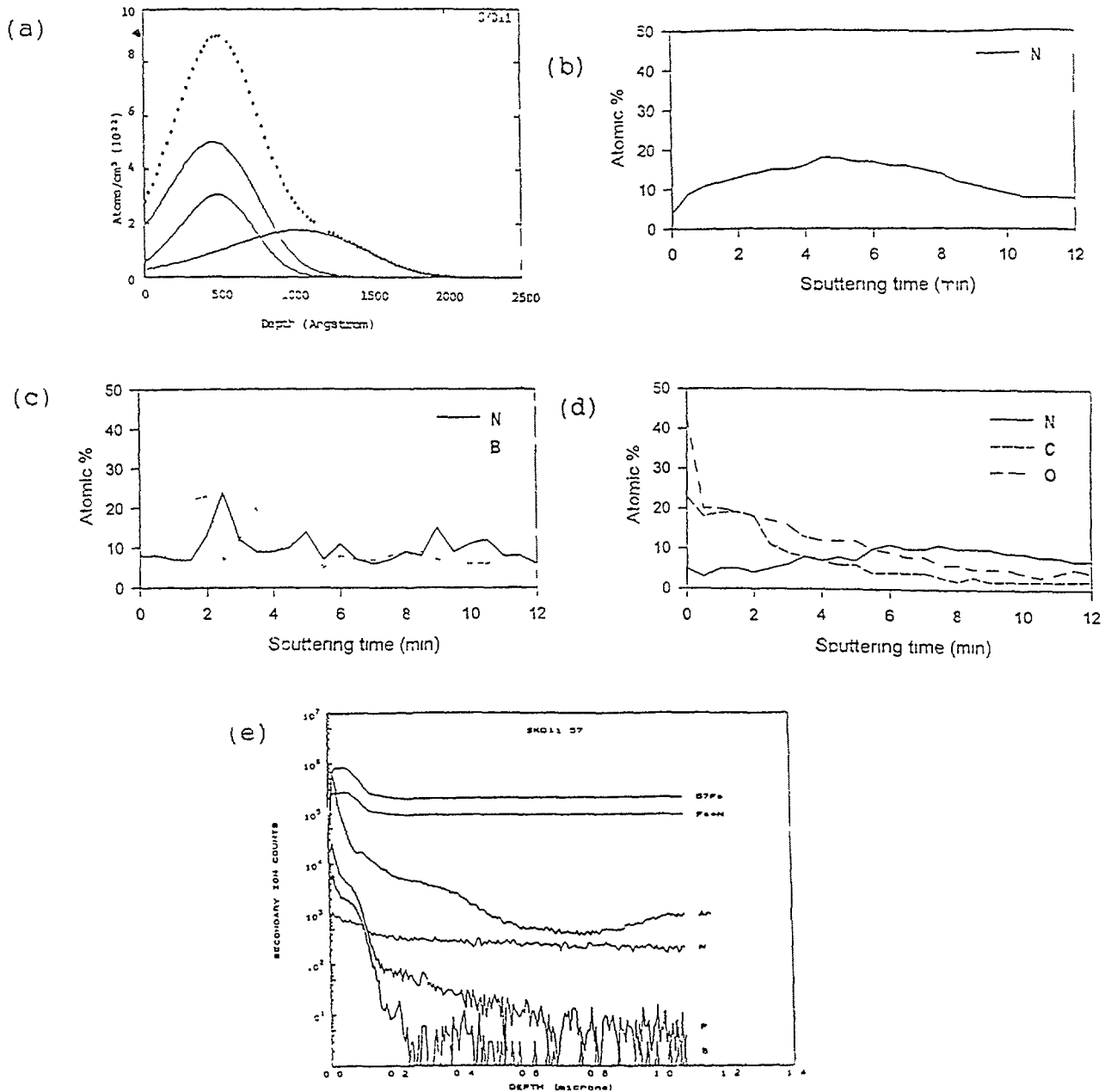


FIG. 29. Analysis of the ion depth profiles. (a) simulated profile for $N + N_2 + N_2$ ion implantation with the same parameters as the experimental ones (the dotted curve represents the final profile), (b) AES analysed profile for the $N + N_2 + N_2$ ion implantation, (c) AES analysed profile for the $N + N_2 + BF$ ion implantation, (d) AES analysed profile for the $N + N_2 + CO_2$ ion implantation and (e) SIMS analysed profile for the $AR + N_2 + BF$ ion implantation.

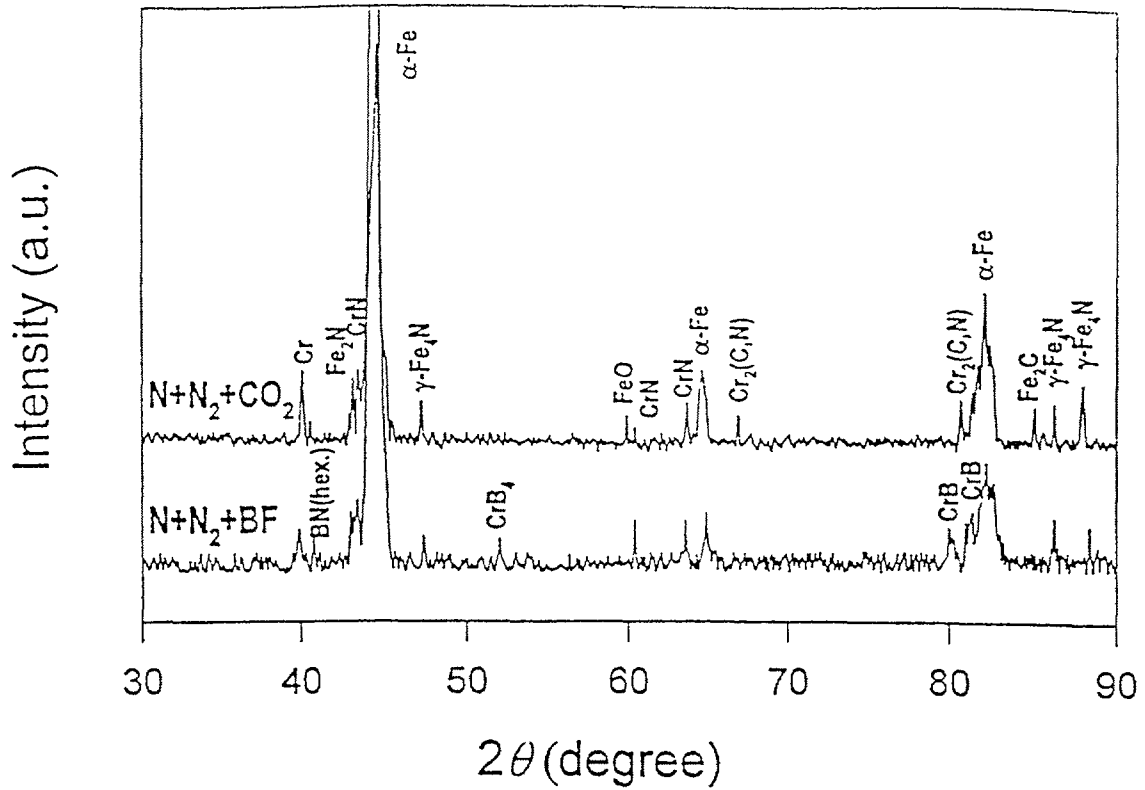


FIG. 30. XRD results from the $N + N_2 + BF$ and $N + N_2 + N_2$ ion implanted samples.

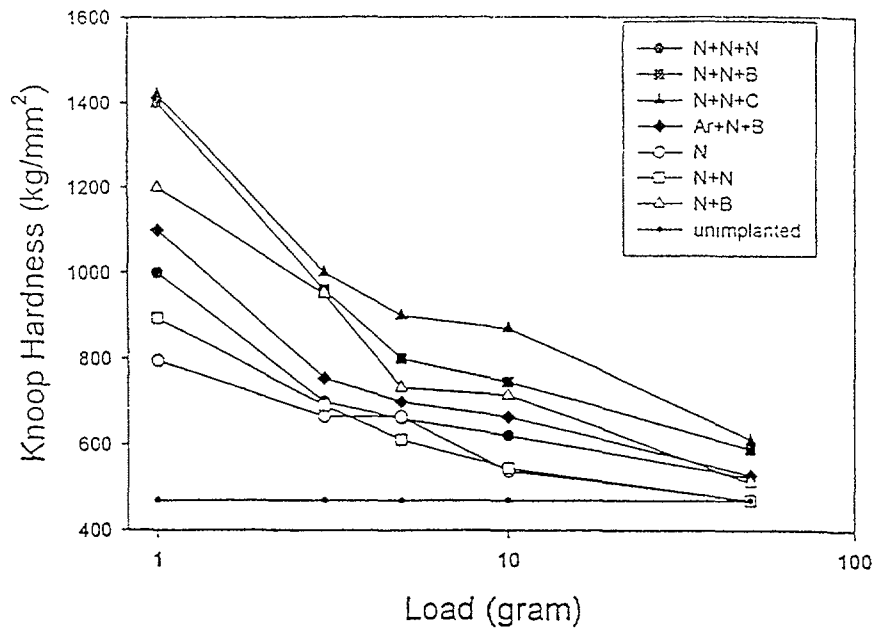


FIG. 31. Microhardness in the Knoop scale as a function of the testing load (1, 3, 5, 10 and 50 g).

TABLE VIII. RATIO N BETWEEN THE WEAR SCAR WIDTH AND THE WORN AREA DIAMETER OF THE BALL FOR ALL THE UNHEATED STEEL SAMPLES. THE RATIO IS CALCULATED AS A MEAN ONE OVER THE TOTAL SLIDING DISTANCE. HERE, R IS A RATIO BETWEEN N (IMPLANTED) AND N (UNIMPLANTED)

Steel	State	WC ball, 550g load		SKF3 ball, 150g load	
		n	r	n	r
M-SKD11	unimplanted	2.99		0.62	
	implanted	1.46	0.49	0.61	0.98
SKD 11	unimplanted	3.96		0.57	
	implanted	1.75	0.44	0.51	0.89
SKS3	unimplanted	1.60		0.83	
	implanted	1.13	0.71	0.78	0.94
S50C	unimplanted	1.10		1.00	
	implanted	0.76	0.69	0.70	0.70
S45C	unimplanted	1.60		0.94	
	implanted	0.99	0.62	0.69	0.73
SCM440	unimplanted	2.74		0.73	
	implanted	1.35	0.49	0.70	0.96

4.8.3. Wear test

Wear test of as-implanted samples were performed on pin-on-disk machine using WC balls with 500g load, 4.8 cm/sliding speed, and 10 000 total-rotations. It can be seen from the wear test results (Table IX) that the triple ion implantation generally reduces wear remarkably, while the wear on either the unimplanted sample or the single and the double N ion implanted ones is comparatively high. In due succession, the ion species for the preparative implantation being effective on the wear reduction are nitrogen and argon, and the species for the closing implantation are boron, nitrogen, and carbon/oxygen. On the surface of the N + N₂ + N₂ and N + N₂ + BF ion implanted samples we can observe an extended large-grained or textured structure whereas on the N + N₂ + CO₂ and Ar + N₂ + BF ion implanted samples we see a much finer and smoother structure. The former microstructure is thought to be related to nitride or boride formation (as shown in Fig. 30), exhibiting high wear resistance, while the latter is less helpful to wear resistance due to either brittle oxide in the case of the N + N₂ + CO₂ ion implanted surface or heavy radiation damage created by Ar ions for the case of the Ar + N₂ + BF ion implanted surface.

TABLE IX. ION IMPLANTATION AND MECHANICAL TESTING RESULTS OF THE SKD11 STEEL

Sample	Ion	Energy (keV)	Current (μA/cm ²)	Dose (10 ¹⁷ /cm ²)	HK	Wear rate (10 ⁻⁶ mm ²)
S0	-	0	0	0	470	1.30 ^a
S1	N+N ₂ +N ₂	120-120-90	100-200-200	2+4+2(N)	1040	0.11
S2-1	N+N ₂ +BF	120-120-90	100-200-50	2+4+2(B)	1410	0.10
S2-2	N+N ₂ +BF	120-90-75	100-200-30	2+4+1(B)	1046	0.11
S3	N+N ₂ +CO ₂	120-120-110	120-120-100	2+4+2(C)	1420	0.14
S4	Ar+N ₂ +BF	140-120-90	200-200-50	2+4+2(B)	1120	0.26
S5	N ₂	120	200	4	795	1.30 ^b
S6	N+N ₂	120-120	100-200	2+4	895	1.26 ^c
S7	N ₂ +BF	120-90	200-95	4+2(B)	1200	0.19

4.9. APPLIED HIGH-CURRENT N ION IMPLANTATION OF INDUSTRIAL STEELS AND TOOLS

Specimens of white steel, SKD11, SKS and S50C steels were prepared normally in the shape of a disk of 3cm diameter and 2–3 cm thickness with mirror-surface finish. Three modes were used for ion implantation of the heat-treated SKD11 steel samples: (1) 50 keV continuously, (2) 50–120–140 keV in sequence and (3) 140–120–50 keV in sequence. In order to prevent the hardened steel from being significantly heated by the high-current beam, the ion beam was pulsed and the samples were water-cooled. For investigating the beam tempering effect on the samples, some implantations were made by varying the pulse modes and without water-cooling. After ion implantation, the steel samples underwent hardness and wear tests.

4.9.1. X ray diffraction

The as-implanted sample was characterized by X ray diffraction method. It is seen from the XRD patterns (Fig. 32) that the multiple-energy ion implantation generally produces more remarkable metal nitride than the mono-energetic one. The fact, that the former shows larger improvement in the mechanical properties of steel than the latter one. This indicates that the nitride formation in the former case has a stronger effect on surface modification than the ion beam irradiation induced surface compressive stress which is the main source of strain hardening for the latter case.

4.9.2. Wear test

The wear test was performed with a pin-on-disk tribometer using WC balls at a load of 500 g. The typical sliding speed was at about 4.8 cm/s and the total number of sliding cycles was 104. The measured wear rate changes, as listed in Table X, which shows the reduction in wear rate depends on ion implantation methodology. The multiple energy ion implantation is generally more beneficial to wear reduction than the single energy ion implantation. The results from varying the beam pulse parameters show the ion beam heating effect on the steels' mechanical properties. The shorter time exposure of the target to the ion beam improves the wear reduction and hardness as compared to the longer time exposure. The beam induced heating plays a role in tempering the steel surface that leads to the least wear loss.

4.10. DEPOSITION OF ALN FILM BY HIGH ENERGY DENSITY PLASMA

Nano-scaled AlN coatings were produced on steel substrate by pulse high energy density plasma gun (PHEDP) method. The schematic of the process is shown in Fig. 33. A hard Al

TABLE X. WEAR RATE CHANGES OF ION-IMPLANTED SKD11 HARDENED SAMPLES

Sample	Ion energy (keV)	Wear rate (wr) (10^{-6} mm^2)	wr/wr ₀
* (o0)	0	0.25	1
* (o1)	50	0.146	0.25
* (o2)	50-120-140	0.111	0.25
* (o3)	140-120-50	0.121	0.07
* (a0)	0	0.50	1
* (a1)	140	0.24	1/2.08
* (a2)	140	0.21	1/2.38
* (a3)	140	0.30	1/1.67

With *, the samples are heat treated, (0): oil quenched, (a): air quenched

alloy was implanted at room temperature with 30 keV nitrogen ions using plasma immersion ion implantation (PSII) to a dose of $1.5-6 \times 10^{17}$ N⁺ ion/cm². This resulted in a uniform, continuous and polycrystalline AlN layer.

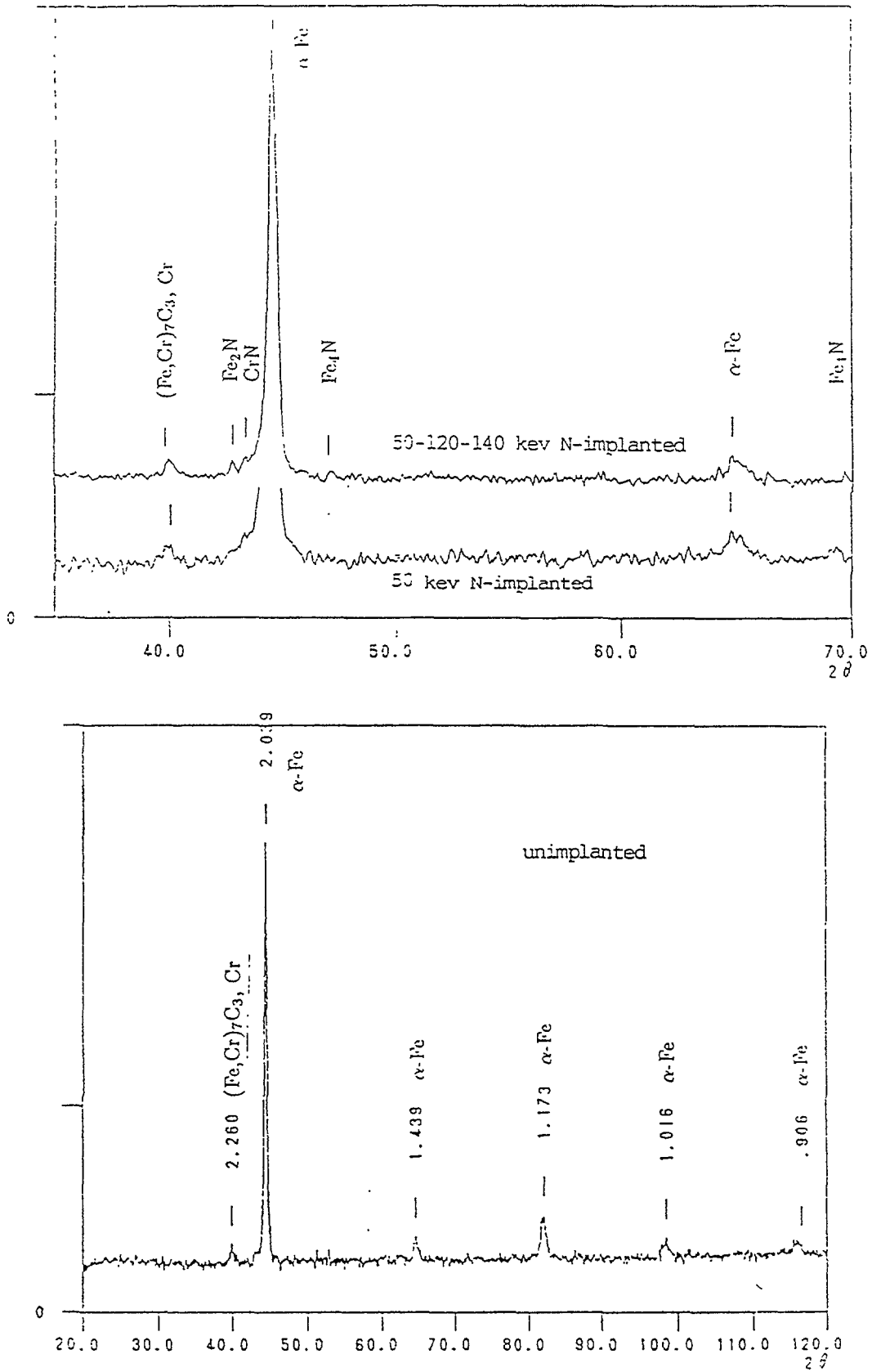


FIG. 32. XRD patterns of the ion implanted SKD11 samples.

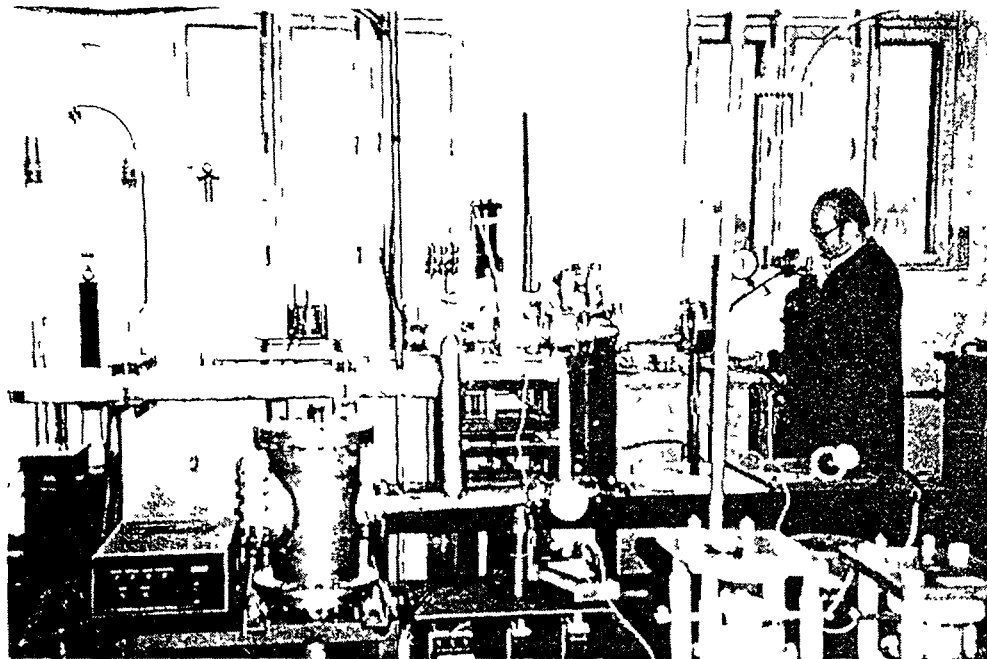


FIG 33. Experimental set-up of pulse high energy density plasma coating system.

The as-implanted samples were analyzed by XPS (Fig. 34) and AES (Fig. 35), which shows the composite film of AlN, Al, and Al₂O₃ were produced and thickness of the AlN layer being ~0.15 μ . After the coating was made, the as-implanted samples were subjected to corrosion and microhardness tests. It was observed that the corrosion resistance in the 2% salt water at room temperature increased by about 10 fold.

4.11. ION IMPLANTATION ON BIO-MATERIALS

It is widely recognized that the wear products of total hip prosthesis pose a significant clinical problem by causing adverse tissue reactions, leading to loosening of the implant fixation, pain, restricted function, and eventually can lead to an expensive and complicated revision surgery. In recent years, an increasing amount of research has been focused on the wear behaviour of prostheses and prosthetic joint materials. There are a range of surface modification processes, including ion implantation, and coating techniques that are either being applied on these materials or being evaluated.

XPS spectrums of N 1s and Al 2p

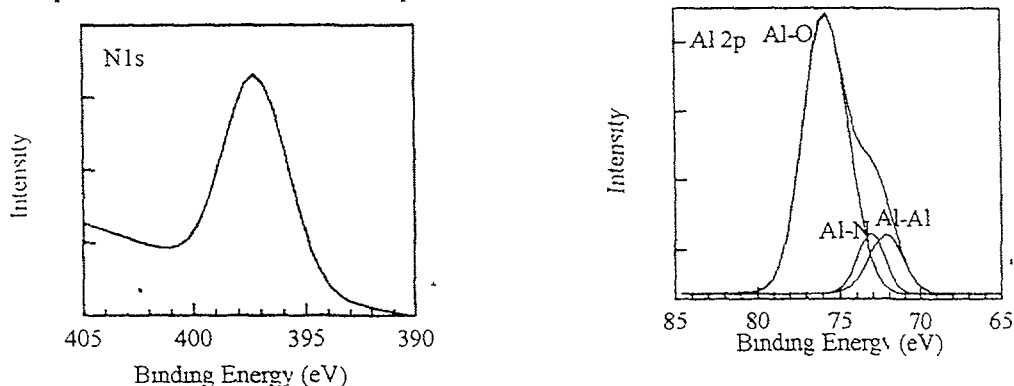


FIG. 34. XPS spectrum of N 1s and Al 2p on steel substrate.

AES profiles:

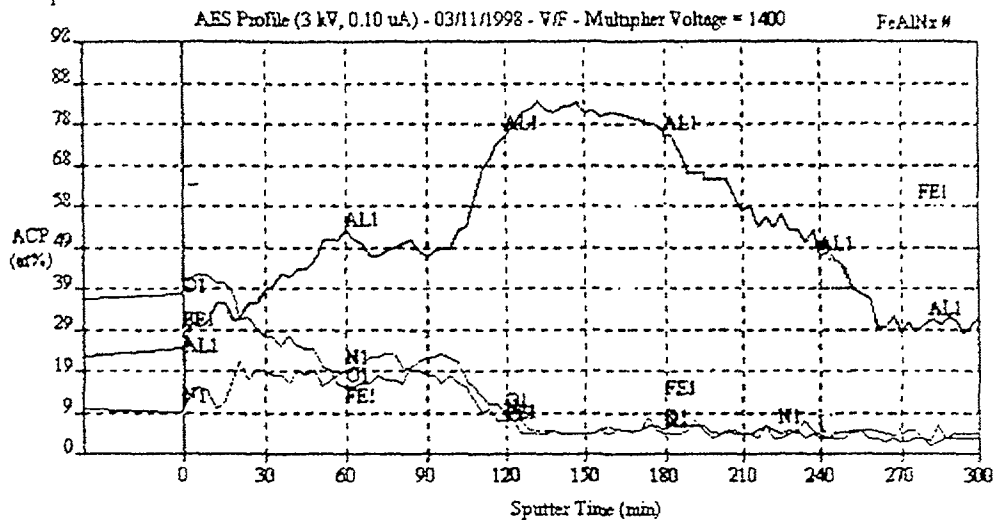


FIG. 35. AES depth profile of AlN coated steel substrate.

The main concern has not been the reduction of the metallic counterpart wear (mainly Co-Cr alloys these days) but on the reduction of the UHMWPE (ultra high molecular weight polyethylene) wear in the acetabular cups or tibial plates. The introduction of ceramic femoral heads has marked a considerable advance in the reduction of the wear of the UHMWPE, and therefore any influence of ion implantation or hard coatings on performance of hip-joints, will be compared both in results and cost basis with the ceramic materials. Therefore the aims of this task have been:

- To evaluate the performance of selected ion implantation treatments and hard coatings in a laboratory knee joint simulator.
- Application of ion implantation or thin films on Co-Cr femoral heads to reduce the wear of the UHMWPE.
- Application of ion implantation on UHMWPE to reduce wear of this material.

4.11.1. Materials and methods

The samples consisted of highly polished (0.01 μm Ra) 15 mm and about 40 mm dia., discs. Definitive ion implantation and coating were carried out on 32 mm in diameter Co-Cr femoral heads, using flat UHMWPE samples as the counterface material.

The following test couples were evaluated:

- (1) Co-Cr-Mo on UHMWPE.
- (2) PVD TiN coated Co-Cr-Mo on UHMWPE.
- (3) Ion implanted (A) Co-Cr-Mo on UHMWPE.
- (4) LC (diamond like carbon) coated Co-Cr-Mo on UHMWPE.
- (5) Co-Cr-Mo on ion implanted UHMWPE.
- (6) Commercial ion implanted (D) Co-Cr-Mo on UHMWPE.
- (7) Alumina on UHMWPE.

These combinations were tested in a knee simulator that is shown in Fig. 36. This machine simulates the movement conditions that take place in a knee, as depicted in Fig. 37, combining sliding and rolling action.

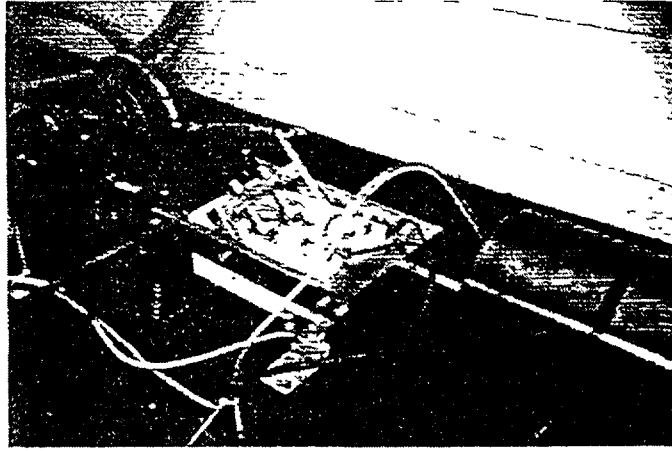


FIG. 36. Experimental set-up of knee wear testing machine.

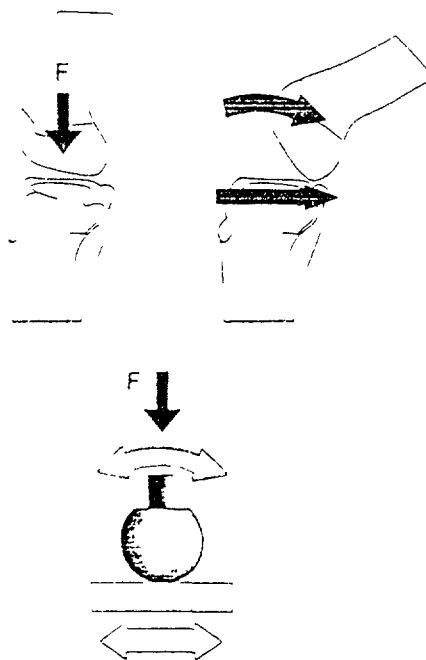


FIG. 37. Movement conditions in a knee and corresponding simulation in the wear testing machine.

4.11.2. Wear test

Wear test was carried out at a load of 500 N, 2 Hz frequency, 12 mm stroke, and 5000000 cycles test duration. The characterization of the wear was carried out by UHMWPE weight loss at given cycles, measurement of the UHMWPE wear track volume by using laser optical profilometry.

4.11.3. Friction test

To complement the knee wear tests, parallel friction tests were also carried out on flat samples of the same materials and coatings. The friction curves can be seen in Fig. 38. The testing conditions are indicated below:

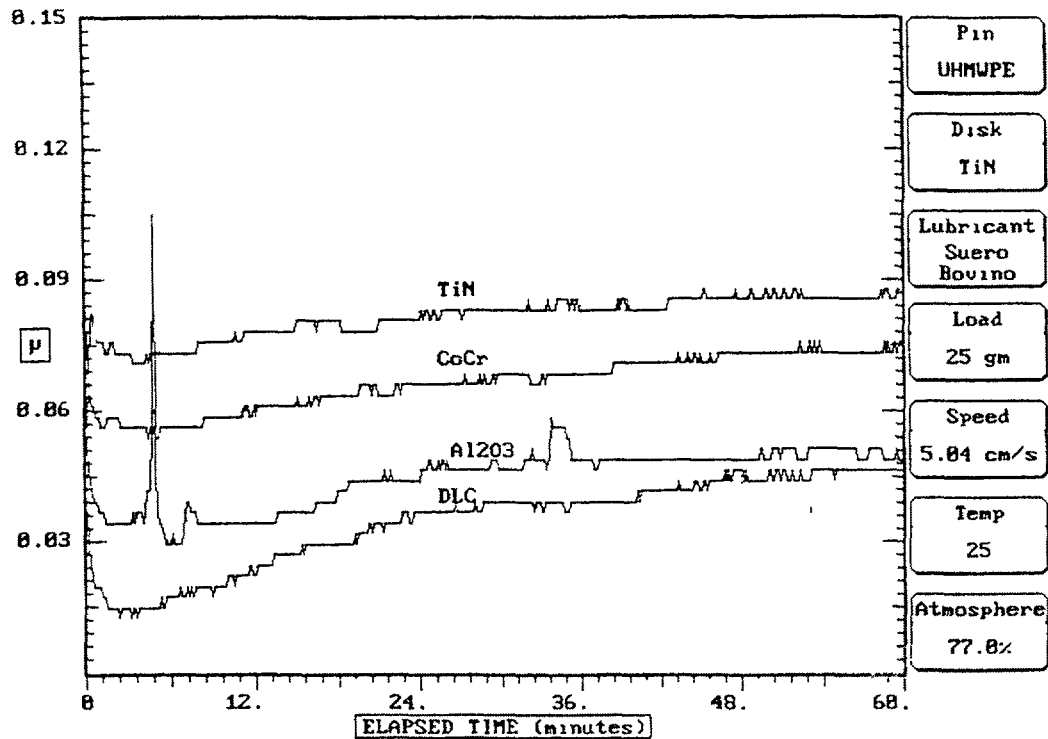


FIG. 38. Friction curves of alumina and selected coatings on Co-Cr.

- "Pin/ball-on-disc" tribometer FALEX ISC-320 with humidity control.
- Ball material: UHMWPE hemispherical pin, 12.6 mm diameter.
- Disc Material: Co-Cr untreated and Co-Cr surface treated or coated. Commercial Alumina.
- Surface finish of samples: polished at 0.01 μm Ra.
- Applied load: 25 gf. Axial load: 0.2452 N. Nominal contact pressure: 8.61 Mpa.
- Lubricant: Bovine serum. Testing temperature: 25^oC.
- Sliding speed: 50 mm/s. Friction test duration: 60 minutes.

Optical profilometry measurements clearly indicated that there was a combined effect by plastic deformation and wear on the UHMWPE surfaces, therefore masking the results. Hence, the weight loss measurements were more precise in determining the clear effect of the treatments or coatings on polyethylene wear. For the assessment of wear, the test was periodically stopped and the UHMWPE plates were removed for desiccation and weighing. Figure 39 summarizes the weight loss measurements obtained from all material combinations.

The following conclusions can be drawn after these tests:

- The higher UHMWPE weight loss is produced against the TiN coating produced by ion plating (PVD). The surface of this coating clearly shows material transfer from polyethylene and very small delamination areas can also be observed on the TiN coating. This coating also produces the highest friction coefficient.
- The untreated Co-Cr material produced a weight loss after 5 million cycles of about 0.0006 g. On the surface of the ball, there was evidence of significant polyethylene transfer. With regards to friction behaviour, the coefficient was second worst and agreed with the wear results.

- The best wear results were obtained on DLC coated and ion implanted Co-Cr together with ion implanted UHMWPE, and close to those results obtained for the alumina. The best friction coefficient was obtained for the DLC coating.

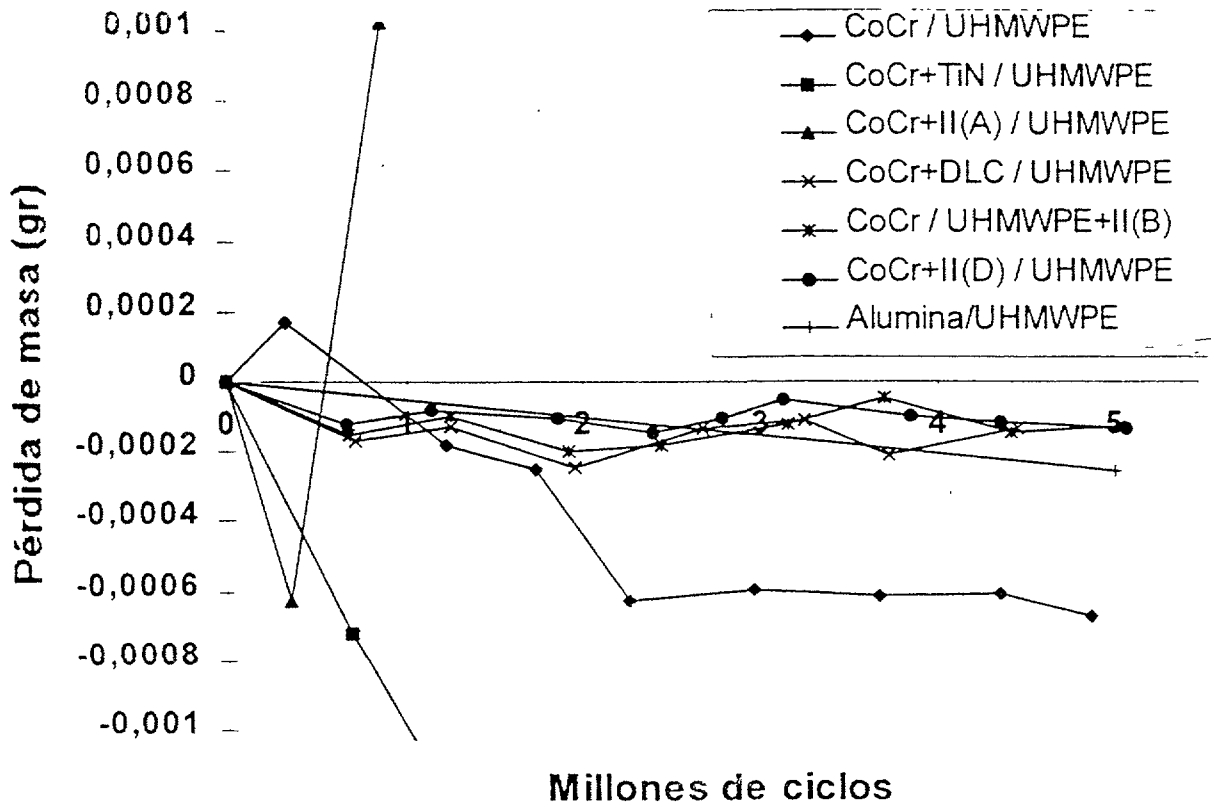


FIG. 39. Weight loss measurements of the UHMWPE material after knee wear tests.

4.12. WEAR FRICTION TEST OF DUAL ION IMPLANTATION AISIM2 STEEL

Three AISIM2 HSS samples, as provided by the supplier were implanted as under:

Sample 1: C+, 20 keV, $j = 10 \text{ (A/cm}^2\text{)}$, $D = 2 \times 10^{17} \text{ C/cm}^2$.

Sample 2: C+, 20 keV, $j = 6 \text{ (A/cm}^2\text{)}$, $D = 2 \times 10^{17} \text{ C/cm}^2$ + Zr+, 25 keV, $j = 8 \text{ (A/cm}^2\text{)}$, $D = 3 \times 10^{18} \text{ Zr/cm}^2$, $D(\text{retained}) = 2 \times 10^{17} \text{ Zr/cm}^2$.

Sample 3: C+, 20 keV, $j = 10 \text{ (A/cm}^2\text{)}$, $D = 2 \times 10^{17} \text{ C/cm}^2$ + Ta+, 20 keV, $j = 4 \text{ (A/cm}^2\text{)}$, $D = 1.5 \times 10^{17} \text{ Ta/cm}^2$.

Three implanted AISI M2 steels were tested in a ball-on-disk FALEX machine ISC 320 with humidity control cabinet. For each sample two loads were applied: 25 and 250 gf. The general conditions of the tests are shown in Table XI. Friction results for all samples and the substrate material at 25 and 250 gf are presented in Figs. 40 and 41. These curves, clearly show that combined implantation of C and Zr ions leads to a significant friction reduction at the 2 loads investigated. The samples had a distinct colour change after ion implantation. No attempt was made in our laboratory to investigate on the nature and composition of the outermost layers.

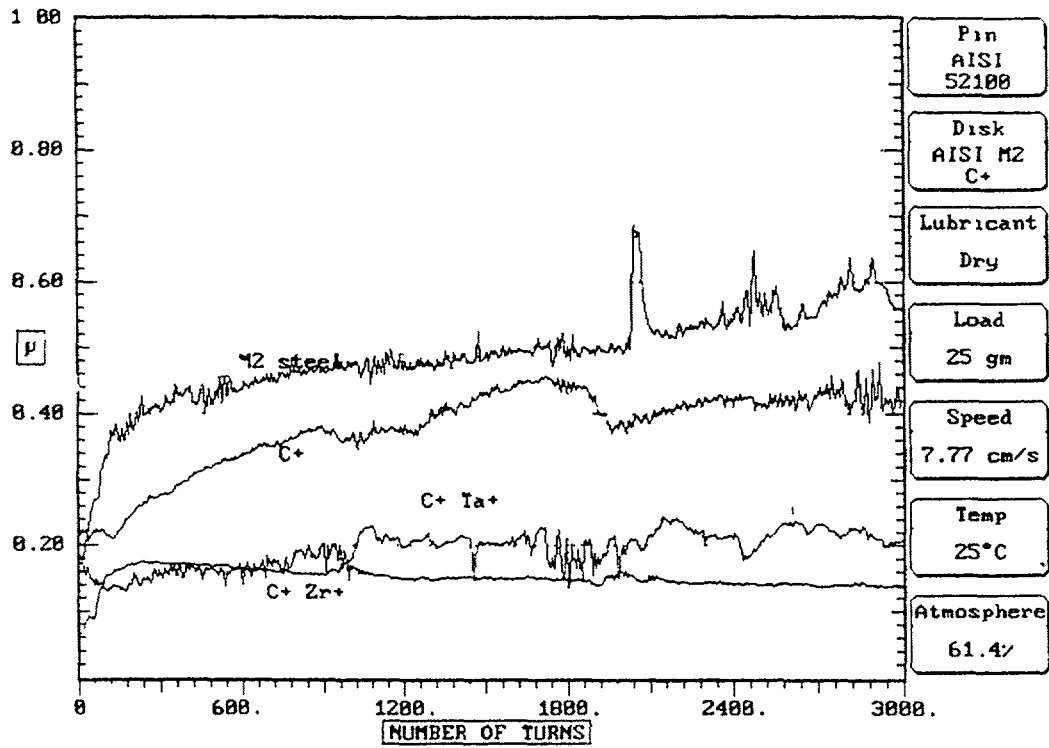


FIG 40 Friction curves of unimplanted and implanted AISI M2 high speed steel at a load of 25 gf.

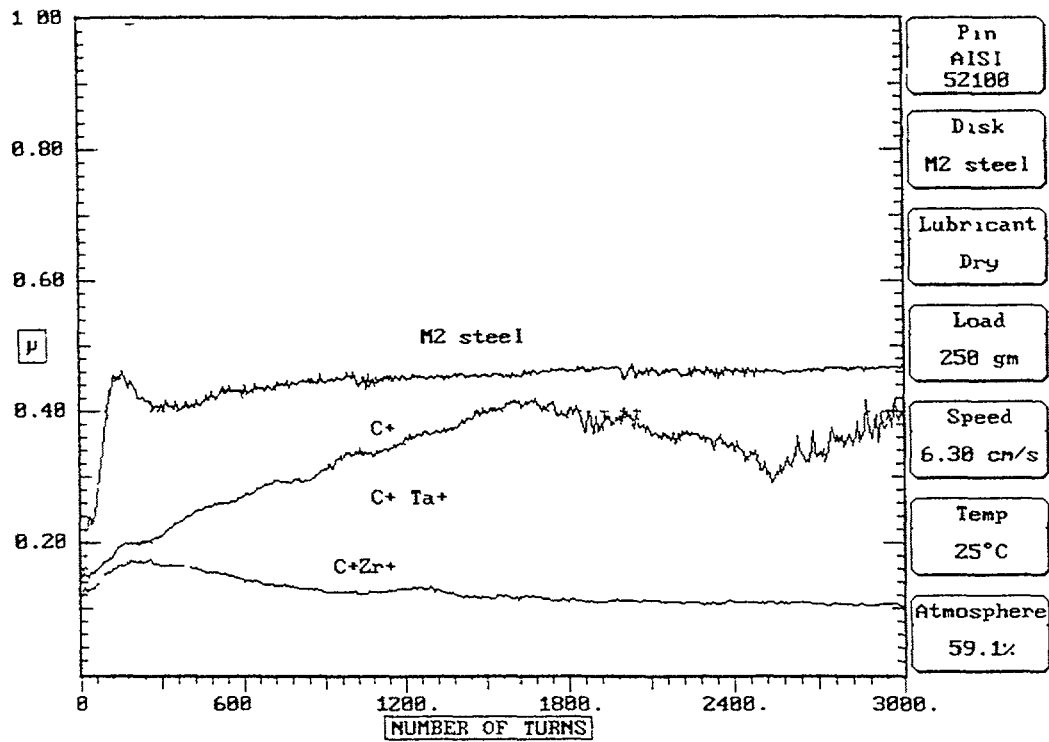


FIG 41 Friction curves of unimplanted and implanted AISI M2 high speed steel at a load of 250 gf.

TABLE XI. EXPERIMENTAL CONDITIONS OF WEAR TEST

	Lower load	Higher load
Ball material	52100 steel	52100 steel
Ball diameter (mm)	10.0	10.0
Disc material	AISI M2 high speed steel	AISI M2 high speed steel
Load (g)	25	250
Speed (rpm)	50	50
Temperature (C)	25	25
Relative humidity (%)	60	60
Track radius (mm)	15.0	12.5
Lubricant	none	none

4.13. PRELIMINARY ION IRRADIATION OF SUBSTRATE FOR IMPROVEMENT OF COATING MECHANICAL PROPERTIES

Argon ion implantation was performed on carbon steel of Y8A type (at. %: 0.22 Mn, 0.16 Cr, 3.58 C, 0.48 Si; Hv = 4.3 GPa) samples by ion beam accelerator of ILY-4 model. The samples were implanted with an ion current density of $2 \mu\text{A}/\text{cm}^2$ and the ion doses ranged from 1×10^{17} to 1×10^{17} ions/ cm^2 . Vacuum level of the chamber was set to 1×10^{-3} Pa and the implantation energy of Ar⁺ ion was 30 keV. After Ar⁺ ion irradiation TiN coating made by a cathodic arc plasma deposition (CAPD) technique (= 100A, pN = 1×10^{-1} Pa, U_{sub} = 120 V, T_{sub} = 20⁰C and 300⁰C, coating thickness h = 1 μm).

4.13.1. Auger electron spectrometry (AES)

The as-deposited samples were characterized by Auger electron spectrometry (AES) using Auger spectrometer PHI-660 (Perkin Elmer).

4.13.2. Scratch and adhesion test

The adhesion of the deposited layer was measured by using a VTT Tech Scratch Tester equipment at a load 100 N/min. Rockwell diamond indenter was used as a counter sample. The speed of translation was set to 10 mm/min.

4.13.3. Friction test

Friction coefficient of as-deposited samples were carried out in a TAY-1MY tribometer at a load of 0.7 N.

4.13.4. Mechanical properties of TiN coatings

It is clear that the best adhesion is observed for coating deposited on the irradiated substrate (up to a dose of 1×10^{17} Ar⁺/ cm^2) and for coating deposited on the substrate heated up to 300⁰C. The use of preliminary irradiation leads to decrease of friction coefficient by 20–30% for TiN coatings (Table XII). The use of Ar⁺ ion implantation of the steel substrate before TiN coating deposition improves significantly its adhesion and friction properties.

TABLE XII. SUBSTRATE TREATMENT MODE

Substrate temperature (C)	Substrate irradiation dose, (10^{16} Ar ⁺ /cm ²)	Critical load L _c , N	Friction Coefficient
	0	5.6	0.43
	1	6.6	0.35
20	5	-	0.33
	10	11.3	0.33
300	0	10.8	0.49

4.14. DEPOSITION OF TiN LAYER BY PLASMA GUN

4.14.1. Impulse plasma deposition method (IPD)

Titanium nitride coating on speed steel SW7M was carried out by IPD method. Impulse plasma deposition method based on utilization of coaxial impulse plasma accelerator as plasma source in the synthesis of coating materials. The coaxial impulse plasma accelerator consists of high current generator and two axial electrodes, separated at one end by insulator, placed inside the discharge chamber. Working gas (nitrogen) at uniform density and temperature fill the space between electrodes, of which the internal one is anode. When the capacitor bank in the current generator is discharged through the gas, an axially symmetric current sheet forms at the surface of insulator and driven by Lorentz force, propagates axially along the electrodes to their opened end. This leads to massive erosion of the electrode material, here Ti, and creates nitrogen-titanium plasma.

4.14.2. Deposition of TiN by means of PVD type steered arc evaporation (St-Arc)

Deposition of TiN layer on SW7M steel was carried out by means of PVD type steered arc evaporation as well as combination of (St-Arc) and DPE method. The device was equipped with titanium cathode of 40 mm diameter and ceramic insulator, both in cylindrical geometry. The arc stabilization has been provided by an axial magnetic field of several oersted intensity. The arc has been ignited by mechanical opening of the special element of the electrical circuit. The discharge current was maintained on the level of 60A in order to eliminate creation of multidrops effect. The deposition procedure has been carried out in one experimental chamber, without stopping of the process and exposing samples to the atmospheric air. During deposition the target material was heated up to 500 C.

Characterization of the samples have been carried out using the following methods:

- Measurements of Ti distribution on the specimen surface by means of electron microprobe microhardness measurements HV001 and HV at different load (20–100G).
- Roughness measurements.
- Microscope study of the sample surface.
- Relative thickness of Ti interlayer estimation by means of X ray analysis.

Characterization of the different type TiN coating is presented on Table XIII. All types of TiN coatings obtained from this experiment were of very good adhesion and extremely high hardness.

4.14.2.1. Adhesion test

Adhesion test was performed by using an advance CSEM REVETEST device, equipped with diamond indenter ROCKWELL, ball type with diameter of $r = 200 \mu\text{m}$ and for comparison — by means of indentation method HRC with evaluation of the indenter traces according scale HF1-HF6.

4.14.2.2. Wear test

The wear test of TiN coated samples have been performed by means of DUCOM trybotester TM-28M equipped with ball $r = 3 \text{ mm}$ operating in ball-on-plain mode at sliding reversible motion. Wear tests have been performed on the two selected samples:

Sample a: TiN coating deposition on the SW7M steel substrate by means of Steered Arc Evaporation technology combined with HIPB-DPE processing (Table XIII, sample no. 117).

Sample b: TiN coating deposition on the SW7M steel substrate by means of IPD method combined with HIPB-DPE processing (Table XIII, sample no. 140).

As reference material speed steel SW7M substrate has been used. Each of the samples has been subject to a series of 5 measurements with different number of cycles and different time duration of the tests (1–20 min.). The applied load was the same (5N) for all measurements, except measurement number of jk1b for sample b. Only in this case the

TABLE XIII. CHARACTERIZATION OF TIN COATINGS

No.	Process	Deposition TiN [nm/s]	Thickness TiN [μm]	Roughness R_a [μm]	Orientation /f-texture factor/	Interlayer distance [A]	Adhesion HF[1-6]	Adhesion Lc [N]
1	2	3	4	5	6	7	8	9
103	Ti + TiN(Arc) T=400°C	4,5	2,7	0,26	(111)/0,38	4,240	HF5	21
119	Ti (DPE-180 μs) TiN(Arc) T=400°C	4.0	2,4	0,39	(111)/0,83	4,246	HF1	53
118	Ti(DPE-190 μs) TiN(Arc) T=400°C	4.5	2,7	0,36	(111)/0,78	4,240	HF1	51
117	Ti(DPE-200 μs) TiN(Arc) T=400°C	4.0	2,4	0,39	(111)/0,83	4,246	HF1	53
137	TiN(IPD) T=400°C	4.8	2,9	0,41	(111)/0,75	4,220	HF1	0
138	Ti(DPE-180 μs) TiN(IPD) T=400°C	4.2x10 ⁴	2,1	0,85	(200)/-0,014	4,212	HF2	29
139	Ti(DPE-190 μs) TiN(IPD) T=400°C	6.0x10 ⁴	3,4	1,08	(200)/-0,32	4,215	HF1	20
140	Ti(DPE-200 μs) TiN(IPD) T=400°C	7.0x10 ⁴	2,9	0,62	(200)/-0,386	4,216	HF1	27
141	Ti(DPE-180 μs) TiN(IPD)	7.0x10 ⁴	3,5	0,32	(111)/0,67	4,204	HF1	12
143	Without heating TiN(IPD) Without heating	6,8x10 ⁴	3,4	0,33	(111)/0,82	4,206	HF1	16

applied load has been changed to 10N. The detailed description of the experimental conditions are presented in Table XIV.

TABLE XIV. EXPERIMENTAL CONDITIONS FOR THE WEAR RESISTANCE TESTS OF TIN COATINGS

Sample a:

Measurement Number	Load F_n	Number of cycles/sec (here and back)	Measurement duration time	Number of cycles
Jk1a	5N	1	5 min	300
Jk2a	5N	1	10 min	600
Jk3a	5N	1	20 min	1200
Jk4a	5N	5	20 min	6000

Sample b:

Measurement Number	Load F_n	Number of cycles/sec (here and back)	Measurement duration time	Number of cycles
(*) Jk1b	5N	5	1 min	300
Jk2b	5N	5	1 min	30
Jk3b	5N	5	20 min	6000
(**) Jk4b	10N, 5N	5	20 min	6000

(*) - trace out of the area

(**)- the load has been decreased during the test

The “experimental results” are presented in Table XV. Maximal values are calculated separately for the sliding “ball-on-plane” in two directions, *to right* and *to left* (here and back). Lack of the symmetry could be caused by the “construction of the device” (systematic error) and could be eliminated by calculation of the average value of the Friction Force $F_{tav} = (F_{1max} + F_{2max})/2$.

TABLE XV. EXPERIMENTAL RESULTS

Sample a:

Measurement	$F_{1,max}$	$F_{2,max}$	$F_{av.}$	$\mu = F_{av.} / F_n$
Jk1a	2.40N	3.60N	3.00N	0.60
Jk2a	2.75N	4.30N	3.52N	0.70
Jk3a	2.85N	4.00N	3.42N	0.68
Jk4a	3.30N	4.75N	4.02N	0.80

Sample b:

Measurement	$F_{1,max}$	$F_{2,max}$	$F_{av.}$	$\mu = F_{av.} / F_n$
Jk1b	3.80N	4.20N	4.00N	0.80
Jk2b	3.00N	3.00N	3.00N	0.60
Jk3b	4.50N	4.30N	4.40N	0.88
Jk4b	4.00N	4.10N	4.05N	0.81
	8.05N (*)	8.80N (*)	8.42N (*)	0.84 (*)

(*) - load $F_n = 10N$

The TiN coating produced with use of combination of St-Arc method as well as the IPD is characterized by extremely high wear-resistance caused probably by their very high hardness and adhesion. The only disadvantage of these techniques is relatively high roughness of the coating surface.

4.15. FORMATION OF TIN LAYER ON HSS PROFILE MILLING CUTTERS AND STEEL BALL VALVES

4.15.1. Deposition of tin layer on HSS profile milling cutters

TiN coating on HSS profile milling cutters was carried out by both the magnetron sputtering deposition and pulsed high voltage discharge ion implantation. The schematic of this process is shown in Fig. 42. The experiments have been carried out using an equipment

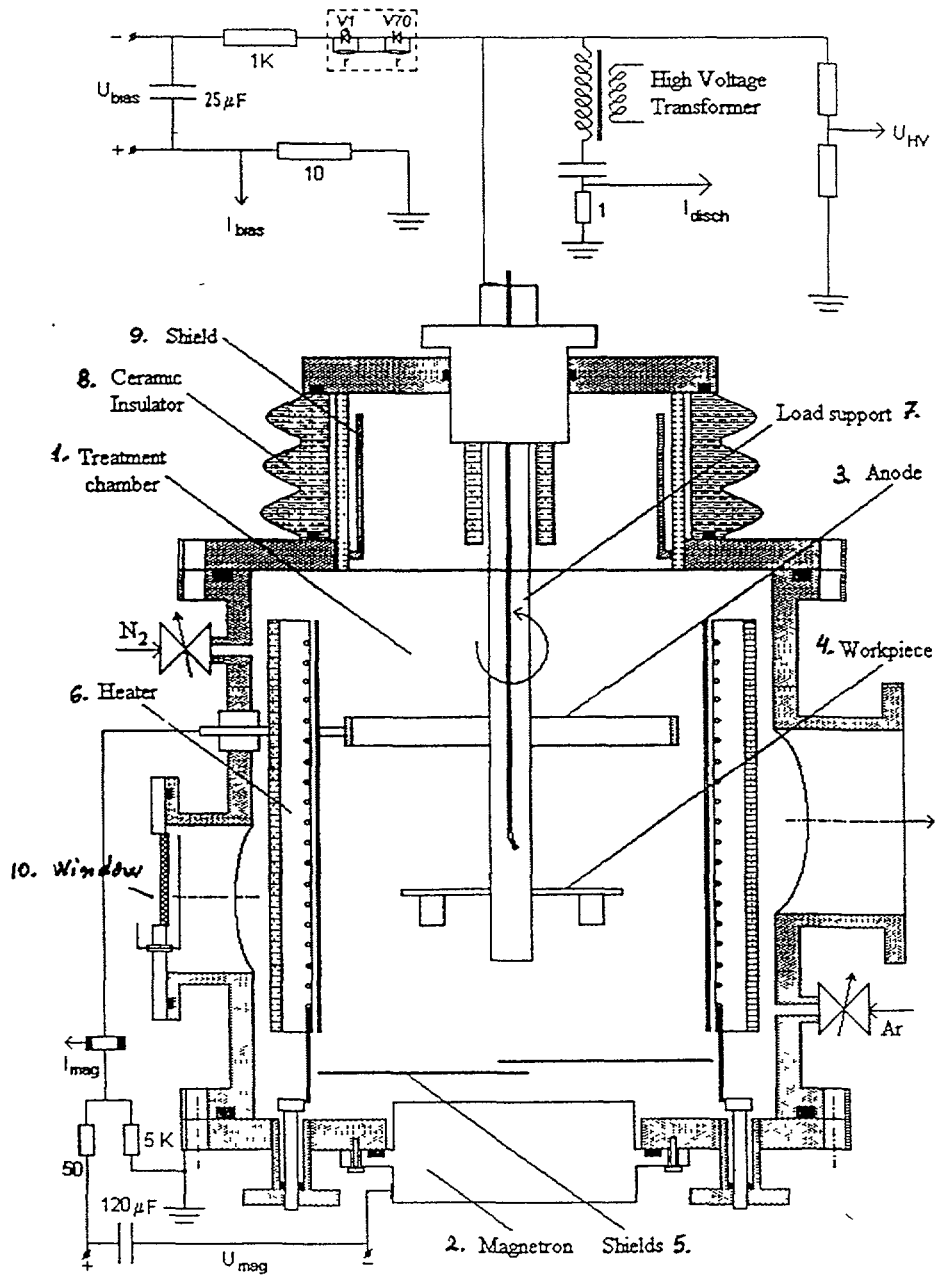


FIG. 42. Experimental set-up for combined magnetron sputtering deposition and ion implantation treatment.

especially designed and built for combined treatments of plasma nitriding, magnetron sputtering and ion implantation (Fig. 42). The treatment chamber (1), has cylindrical shape with water cooled walls. The inner diameter is 300 mm and the height is 425 mm. On the bottom plate a circular magnetron (2) with an active target area of $\sim 40 \text{ cm}^2$ is mounted. The anode of magnetron (3) is a stainless steel ring with a diameter of 165 mm, 2 mm thickness and 15 mm width. It is positioned at 220 mm above the bottom plate, insulated from the chamber wall. A pair of shields (5) cover the magnetron target surface when a plasma nitriding treatment is performed. On the bottom, plate four ceramic columns (6) are also mounted which hold the kanthal heaters. These are used to heat the workpiece before sputter cleaning. The workpiece is suspended by a special device (7), which is supported by a ceramic insulator (8), tested up to 150 kV. This entire mechanical structure is positioned on the top plate. A spherical shield (9) prevents the sputtering deposition on the inner surface of the ceramic insulator.

The gases, argon, nitrogen, hydrogen, are introduced into the treatment chamber by means of calibrated needle valves. A 500 l/s diffusion pump is used for the evacuation of the chamber. When a plasma nitriding treatment is performed, the diffusion pump is shut off and only the rotary pump is used. The discharge and the components subjected to the treatment can be visually inspected through the window (10) located opposite to the vacuum port. The X ray produced during the high voltage pulsed discharge are significantly attenuated by the chamber walls except in the window region, where a special shield has been introduced to protect this area also. The main operational parameters of this experimental set up are listed in Table XVI.

Process optimization and the building of pilot scale coating installation for wear/corrosion investigations of ball valves used in oil extraction pumps by ion beam assisted deposition of Ti(Al)N.

TABLE XVI. EXPERIMENTAL PARAMETERS

Parameter	Without High Voltage	With High Voltage
Partial pressure of N_2	4×10^{-4} torr	4×10^{-4} torr
Partial pressure of Ar	1.6×10^{-3} torr	1.6×10^{-3} torr
Magnetron current intensity	1.8 A	1.8 A
Bias voltage	70-90 V	60-120 V
High voltage amplitude	-	40 kV
Current intensity of the high voltage discharge	-	4-5 A
Characteristics		
Hardness	2700-2900 HV0.04	2300-2500 HV0.04
Thickness	$(2.7 \pm 0.2) \mu\text{m}$	$(2.6 \pm 0.2) \mu\text{m}$
Adherence	$L_c = 30-35 \text{ N}$	$L_c = 25-30 \text{ N}$
Structure, constitution	Preferential orientation TiN(111)/Ti ₂ N(200)	Preferential orientation TiN(111)/Ti ₂ N(200)

TiN thin films were deposited by magnetron sputtering of titanium targets in a mixture of argon and nitrogen at a pressure of 5×10^{-3} mbar. The deposition chamber is provided with three rectangular magnetrons. During growth, the deposited thin films were assisted with an intense ion flux drawn from the surrounding plasma by the negatively biased substrates.

4.15.2. RBS and ERDA measurements

The RBS and ERDA measurements were carried out using the Cyclotron and 8 MV Tandem accelerators of NIPNE. The projectiles were 2.7 MeV ^4He for RBS measurements at Cyclotron and 4.5 MeV $^7\text{Li}^{++}$ and 80 MeV $^{63}\text{Cu}^{10+}$ for RBS and ERDA measurements respectively at Tandem accelerator.

For RBS measurements the spot size on target was 2 mm diameter, at a typical current of 1–2 nA at Tandem and 5–10 nA at Cyclotron. Backscattered particles were detected by a surface barrier detector (SBD) placed at 150° relative to the beam direction. For ERDA measurements detector was ΔE (gas)-E (solid) telescope (M. Petrascu et. al. Nucl. Instr. Meth. B4 (1984) 396).

RBS spectra of the TiN film deposit are shown in Fig. 43. It was observed that the RBS profile height decreases with increasing nitrogen content in the film. A typical (E- ΔE) spectrum and the energy spectra of N, O, Si and Ti are shown in Fig. 44. The atomic ratio nitrogen to titanium was determined to be 0.6, and an areal atomic density of 800×10^{15} at/cm² was obtained.

4.15.3. X ray diffraction

X ray diffraction of TiN layer deposited by magnetron sputtering (MSD) is depicted in Fig. 45, which shows the TiN/Ti₂N phases orientated on (111) and (200) planes. When the CMDII (combined magnetron deposition and ion implantation) method is applied the X ray

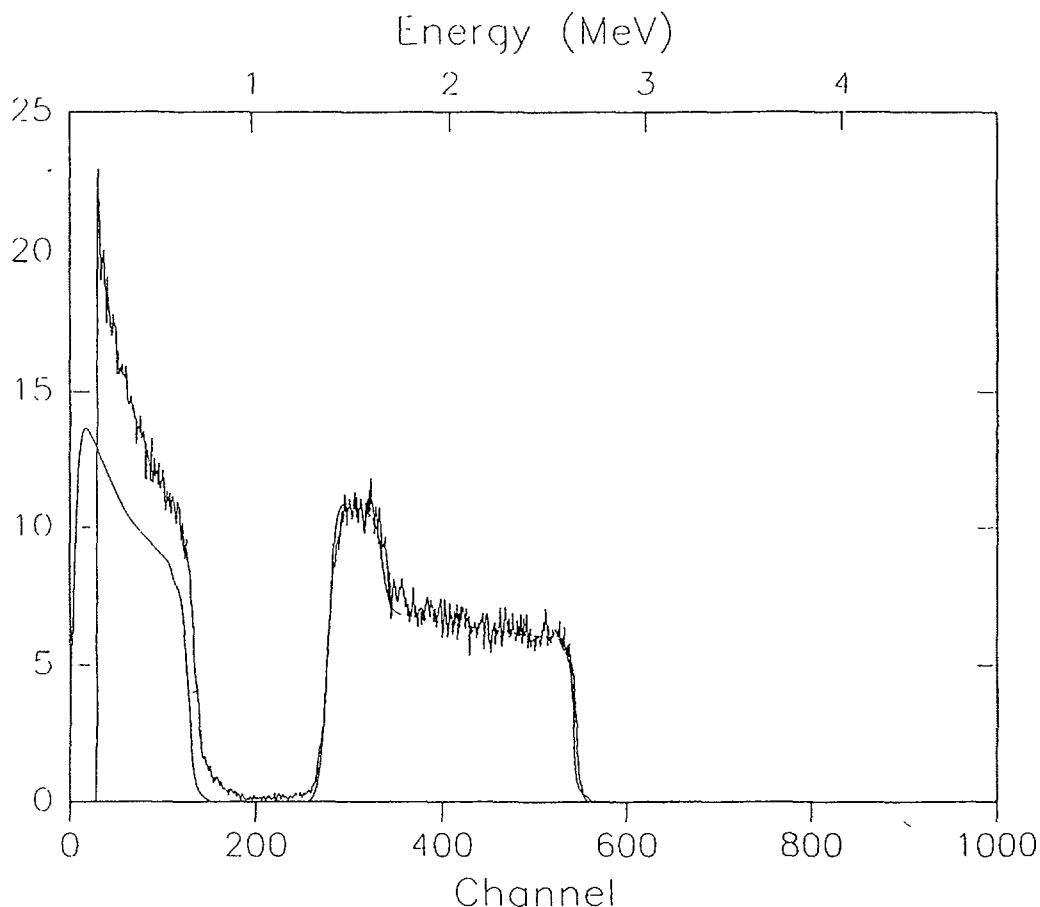


FIG. 43. RBS spectrum of the TiN film deposits on HSS substrate.

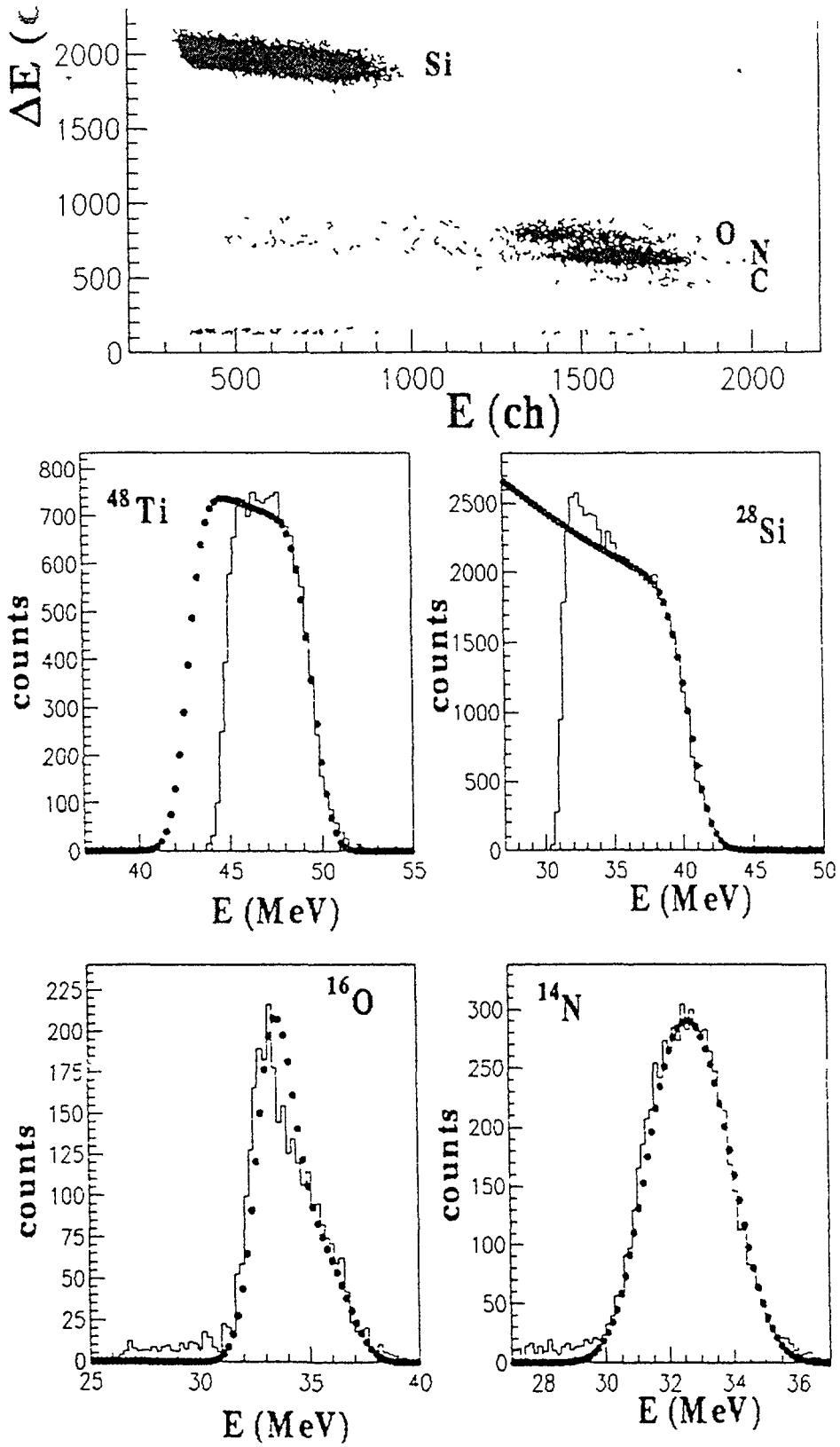


FIG 44. ΔE - E spectrum of TiN film obtained by ERDA and the total energy spectra of the main sample.

diffraction pattern significantly changes, the preferred orientation being (002) for Ti_2N and (220) for TiN (Fig. 46). The wide peak at 61.2° could be an overlap of the two peaks (Ti_2N and TiN) or could be associated with the internal stress. The layer is not too thick, the small peak of α -Fe being detected from the substrate. It is important to notice that by using the CMDII method the preferred orientation during the crystal growth process can be controlled.

As far as tribological the properties of this structure are concerned, the first experiments demonstrated a slightly improved wear resistance of the titanium nitride layer obtained by CMDII compared with that produced by usual MSD (Fig. 46).

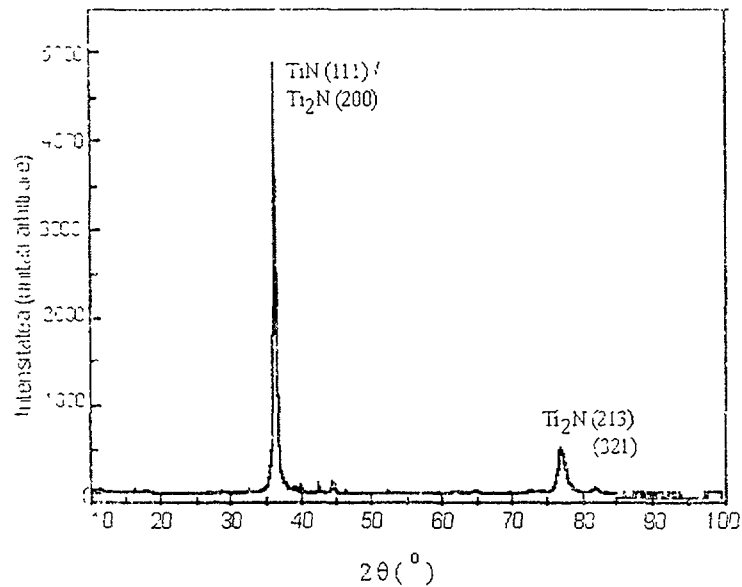


FIG. 45. X ray diffraction pattern with TiN layer produced by magnetron sputtering deposition.

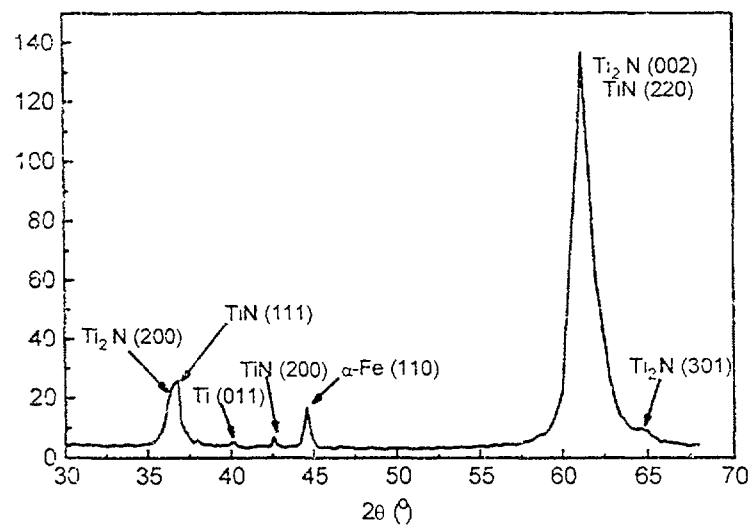


Fig. 46. X ray diffraction pattern of a TiN layer deposited by CMDII method.

4.15.4. Wear test

Wear test on TiN coated sample was performed by "pin on disc" machine, where the pin was a 10 mm diameter bearing ball. The disc was of HSS with a diameter of 60 mm and a thickness of 1.5 mm. The test conditions can be summarized as follows:

- dry sliding with a linear speed $v = 5 \text{ cm/s}$,
- normal force $F_n = 2 \text{ N}$.

Five circular traces of each 100 mts. of sliding distances were made to evaluate the volume of the worn material from the layer. During the test, the position of the ball was periodically changed, in order to eliminate, as much as possible, the influence of the ball wear on the profile of the traces on the disc. The widths of these traces have been measured on a microscope and from geometrical considerations the volume of the lost material has been calculated for each trace. The results are shown in Fig. 47.

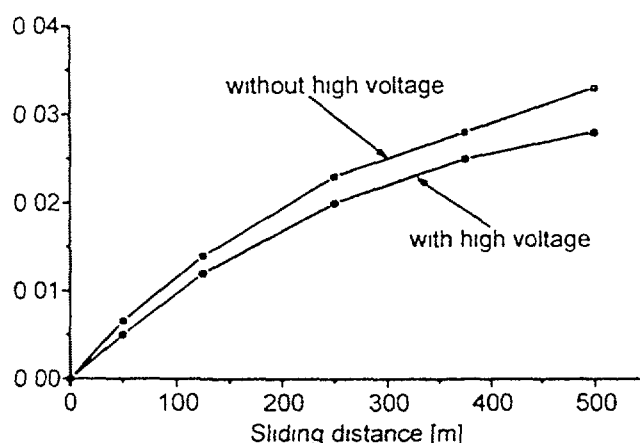


FIG. 47. Wear resistance of TiN coatings produced with and without high voltage discharge.

Regarding the life time increase of ball-valves used in oil extraction pumps, good and reliable results were obtained. The extensive field tests made revealed an increase of the life time with a factor z ranging from 2 to 6 for different extraction fields, the spread of this value for the same extraction field being $\Delta z = 2$.

The application of the CMDII method to the profile milling cutters lead to an increase of 3 to 5 times of the tool life, but from cost efficiency view point it can not compete with other procedure like plasma nitriding which is cheaper and has a higher productivity.

4.16. USE OF ION BEAM MIXING TO IMPROVE THE OXIDATION RESISTANCE OF ALPHA 2 INTERMETALLICS

4.16.1. Intermetallics

The specific properties of ordered intermetallic compounds attracted the attention of aerospace researchers searching for the materials for new generation aircraft turbine engines several years ago. Intermetallics are not only less dense than conventional superalloys, some

of them have the unique characteristic that yield strength increases with the increasing temperature. Much work is still aimed towards obtaining a better understanding of the behaviour of nickel and titanium aluminides. An alloying element, which is known to improve the oxidation behaviour of titanium aluminide, is niobium. However, the mechanism, which is responsible for this effect has not yet been elucidated and so the development of oxidation resistant titanium aluminides has had only limited success.

Titanium aluminium based intermetallics are perhaps the potential material for future gas turbine and aerospace applications for various rotating components such as, blades and vanes. $TiAl$ and Ti_3Al are being considered for these applications, because of their excellent specific strength, low density and good high temperature mechanical properties. The main problems are however, the poor room temperature ductility and relatively high oxidation rates at the temperature of their application. Addition of alloying elements, to make these intermetallics more ductile (at room temperature) and to enhance their oxidation resistance is being tried for a long time.

4.16.2. Oxidation of Ti_3Al alloys

An important aspect of the oxidation of Ti-aluminides, compared to the aluminides of Ni and Fe, is the small difference in standard free energy of formation between alumina and titania. The Al activity is much smaller than unity in Ti_3Al . Combining the activities with standard free energy data for the oxides indicates that TiO_2 is more stable in contact with the alloy than is Al_2O_3 for atom fractions of Al less than about 0.5. A thermodynamic calculation of oxide in the Ti-Al-O system shows that the selective oxidation of Ti occurred for the alloys with an aluminium content less than 50 at.%. The selective oxidation of Ti leads to a sublayer rich in Al. Since, the oxygen atoms easily diffuse inwards through TiO_2 with a large amount of anion vacancies, the Al_2O_3 forms under the outer oxide layer. The Ti_3Al alloys can not be expected, therefore, to form continuous alumina scales. Instead, they form mixed rutile-alumina scales. Since the TiO_2 scale formed on pure Ti and the mixed Al_2O_3/TiO_2 scale on Ti_3Al are both porous and flaky, the higher oxidation resistance of the Ti_3Al-Nb alloys has been attributed to the ability of these alloys to form relatively dense layer of $TiO_2.Nb_2O_5$. The oxidation kinetics of Ti_3Al -base alloys between 600-900°C are reported to be those expected for rutile growth. Since, the TiO_2 scale formed in pure Ti and the mixed TiO_2/Al_2O_3 scale on Ti_3Al are both porous and flaky, the higher oxidation resistance of the Ti_3Al-Nb alloys has been attributed to the ability of these alloys to form relatively dense layers of $TiO_2.Nb_2O_5$, which acts as a graded seal resulting in the blockage of fast diffusion paths.

Slower oxidation rates in air were due to the presence of nitrogen, which tended to concentrate at the oxide-metal interface due to the higher diffusion rate in the oxide compared to that in the metal. It was also concluded that for both the binary Ti_3Al and $(Ti, Nb)_3Al$ alloys the oxidation rates are lower in air than in oxygen because of the nitrides formed at the oxide/alloy interface during the oxidation in air. The nitride layers were found to be more profuse for alloys containing Nb.

The addition of an element, which either oxidizes selectively or helps in selective oxidation of aluminium to form protective alumina scale improves the oxidation behaviour of the Ti_3Al -base alloys. If this is not possible, then the alloying element should at least modify the scale characteristic to make it relatively more protective. The oxides Al_2O_3 and SiO_2 are of principal interest because they exhibit low diffusivities for both cations and anions as well as being highly stable.

The addition of Nb to Ti₃Al slows the rate of high temperature oxidation as the result of doping of the TiO₂ in the scale. The dissolution of Nb⁺⁵ into TiO₂ is expected to reduce the concentration of both Ti-interstitial and O-vacancies. Although the high temperature of the ternary Nb modified Ti₃Al alloys offer attractive high temperature mechanical properties, the oxidation resistance of these alloys are not satisfactory for their high temperature uses.

In this work, the surface modification of the Ti₃Al-Nb alloys have been tried by: Cr nitrided by plasma arc, plasma nitriding and Al/Ar⁺ ion beam mixing. Three different Ti₃Al-Nb alloys of following compositions were used in this work: Ti-25Al-11Nb, Ti-24Al-20Nb and Ti-22Al-20Nb.

4.16.3. Ion beam mixing

A coating of aluminium was made by deposition of Al using PVD. This was followed by implantation of a 30 keV Ar⁺ ion beam. Ion implantation facility of the University of Bombay, was used for this purpose. The samples were coated with 300Å Al thin film from both sides at room temperature (by PVD method), followed by the implantation with Ar⁺ ion at an operating voltage of 30 keV for a total of 1×10^{17} ions/cm². Average beam current was maintained at 8.5µA. Vacuum during implantation was of the order of 7×10^{-5} torr.

4.16.4. Plasma nitriding

Plasma nitriding was carried out at Multiarc Pune. The pressure of nitrogen was maintained at 0.4 torr. with a ratio of N₂:H₂ = 1:3. The temperature used for coating was 750°C and the coating took about 2 h

Oxidation tests were carried out in air at 800°C. The weight change of the sample was recorded continuously during the oxidation. The oxide scale was characterized using optical microscope, XRD and SEM/EDAX.

4.16.5. Plasma - Arc CrN coating

Scanning electron micrographs of chromium nitrided Ti-25Al-11Nb, Ti-24Al-20Nb alloys before oxidation are shown in Fig. 48. Unmelted chromium is seen in the form of bubbles on the surface of the alloys. Distribution of various elements present in the coating is shown in the X ray area scan maps depicted in Fig. 49, which shows a weak but uniform distribution of nitrogen and densely distributed chromium in the coating. X ray diffraction analysis (Fig. 50) reveals the presence of chromium nitride (CrN) as the main phase in the coating. Surface composition for CrN layers on Ti-25Al-11Nb and Ti-24Al-20Nb sample was determined by EDAX as shown in Tables XVII and XVIII.

These analyses confirm that the coating consists mainly of CrN with some incorporation of Ti and Nb. Small traces of Al were also found in the coating.

4.16.6. Plasma nitriding coating

Scanning electron micrograph of plasma nitrided Ti-25Al-11Nb alloys before oxidation is shown in Fig. 51. Some local inhomogenities can be seen on the coated surface. Distribution of various elements present in the coating is shown by the X ray area scan maps depicted in Fig. 52, which reveal a weak but uniform distribution of nitrogen and dense distribution of Ti, Nb, and Al in the coating. X ray analysis (Fig. 53) reveals the presence of titanium nitride (TiN) as the main phase in the coating. Surface composition for TiN layer on the coating was determined using EDAX. The results are given in Table IXX.

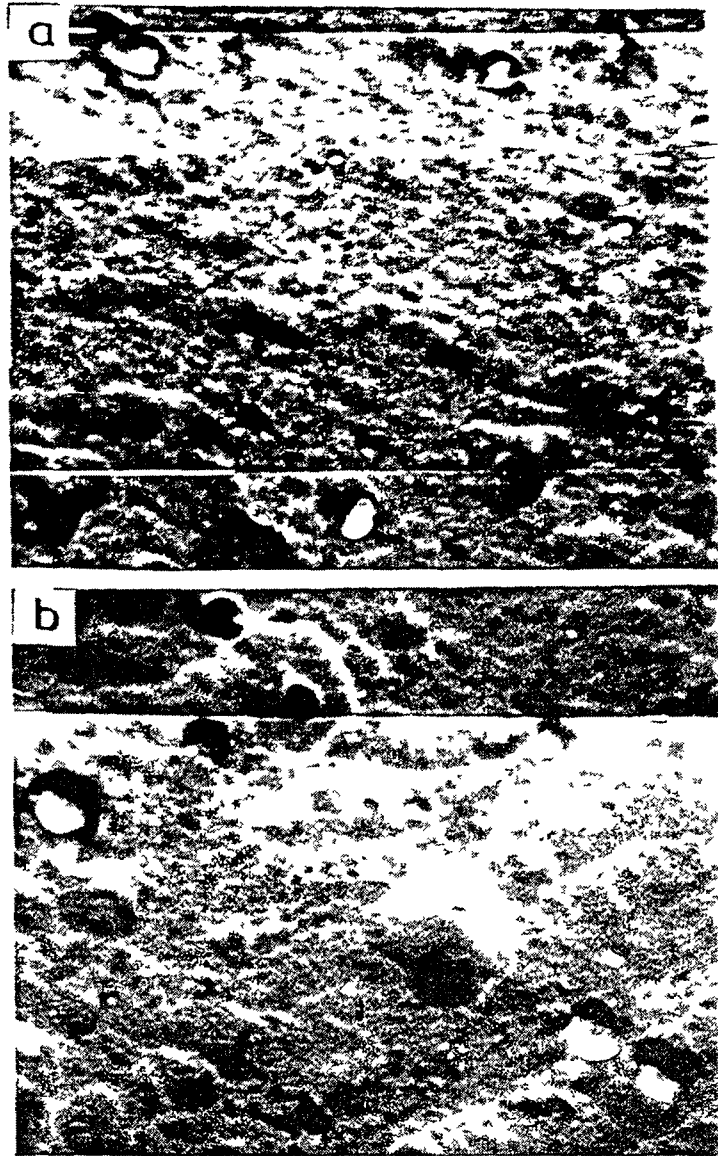


Fig 48 Scanning electron micrographs of chromium nitride coated (a) Ti-25Al-11Nb and (b) Ti-24Al-11Nb alloy before oxidation

TABLE XVII. COMPOSITION OF CRN COATED TI-25AL-11NB SAMPLE (ELEMENTS IN WT.%)

Location	Al	Ti	Cr	Nb
1.	0.662	2.092	94.471	2.775
2	0.746	2.271	94.020	2.964
3	0.595	2.2144	4.596	2.666

TABLE XVIII. COMPOSITION OF CrN COATED Ti-24Al-20Nb SAMPLE (ELEMENTS IN WT.%)

Location	Al	Ti	Cr	Nb
1	0.695	2.269	94.179	2.856
2	0.642	2.296	94.024	3.038
3	0.503	2.098	95.076	2.323

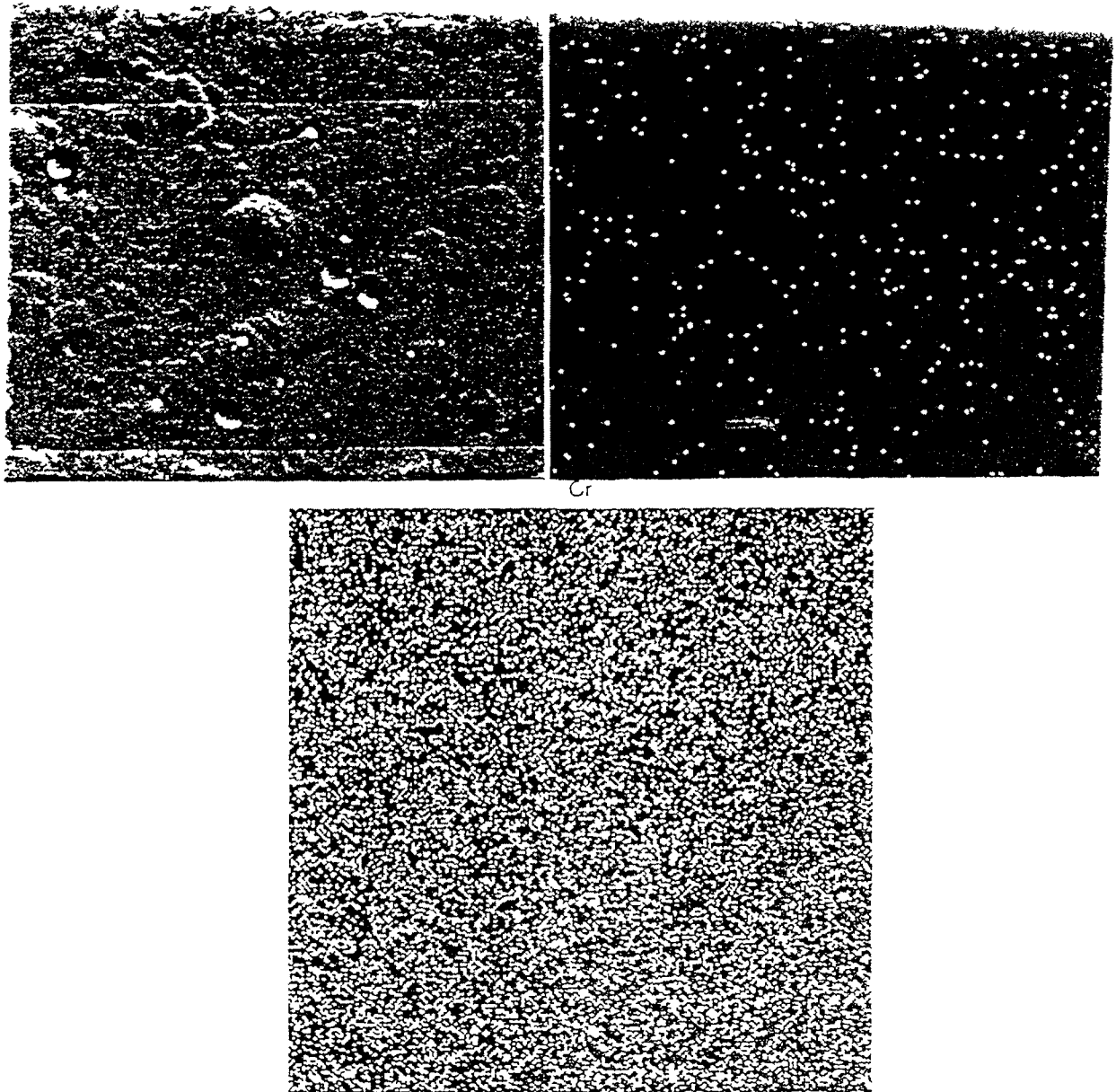


FIG. 49. SEM micrograph and X ray area scan maps of N, Cr for the chromium nitrided Ti-25Al-11Nb alloy.

TABLE IXX. COMPOSITION OF PLASMA NITRIDED COATED Ti-25Al-11Nb SAMPLE (ELEMENTS IN WT.%)

Location	Al	Ti	Nb
1	8.631	52.315	39.054
2	4.894	56.575	38.531
3	4.902	56.062	39.036
4	4.988	55.780	39.232

The compositional analysis by EDAX confirms that during plasma nitriding, TiN is the main coating. However, large amount of Al and Nb is also found in the coating.

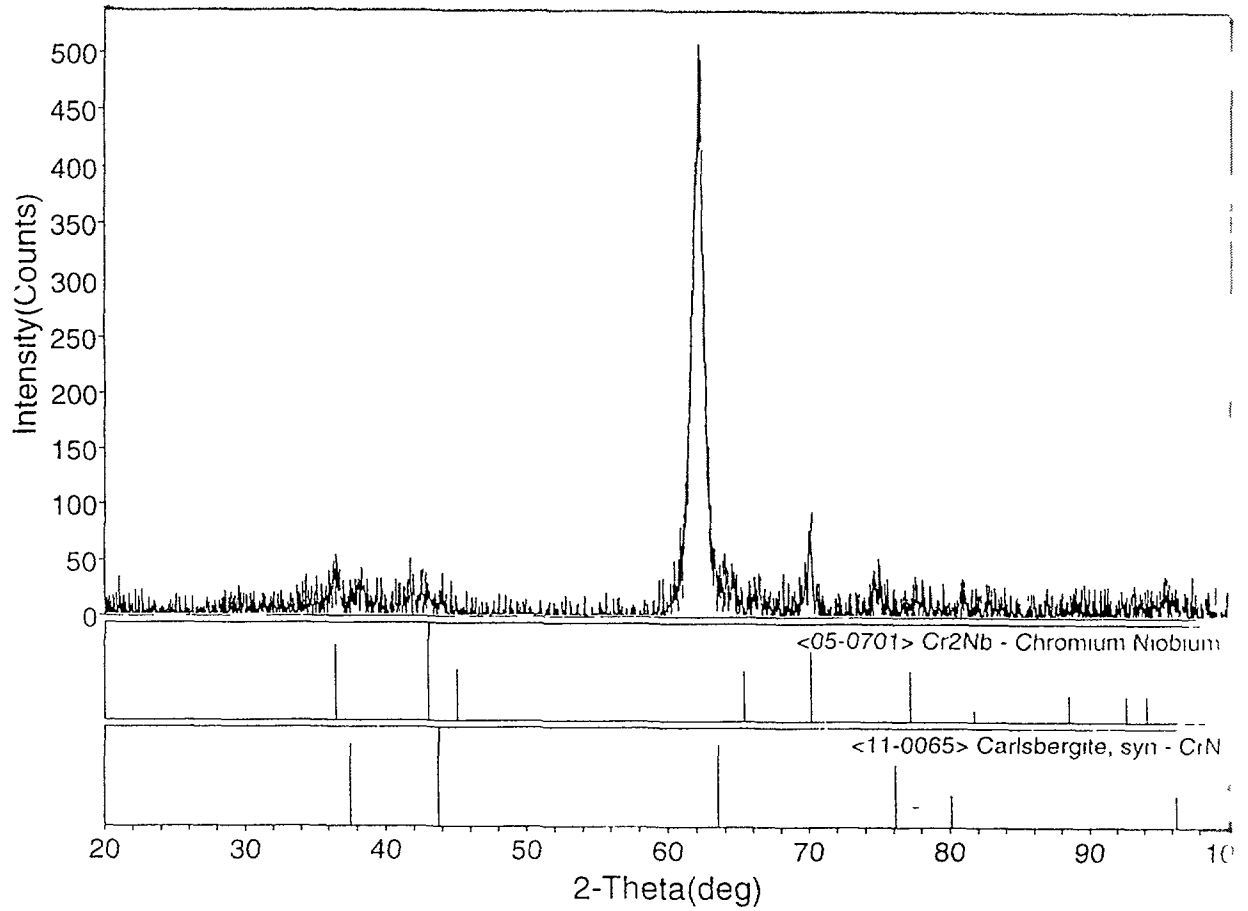


FIG. 50. X ray diffraction method of CrN coated Ti-25Al-11Nb alloy.

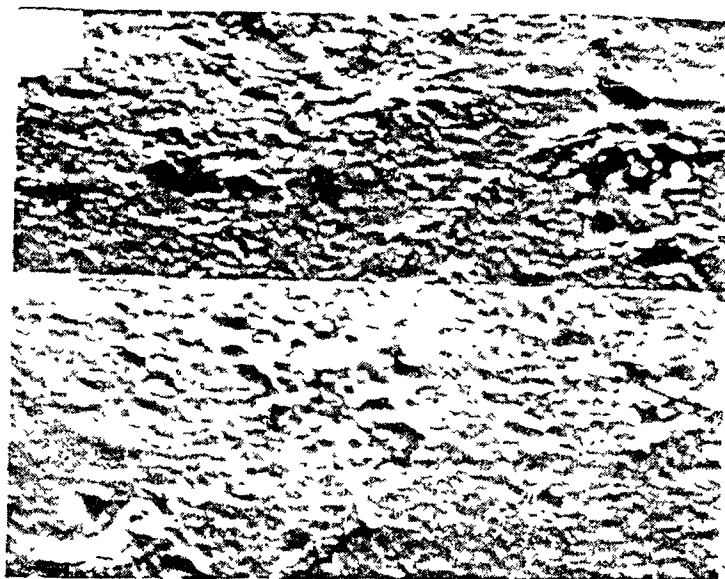


FIG. 51. Scanning electron micrographs of plasma nitrided Ti-25Al-11Nb alloy before oxidation.

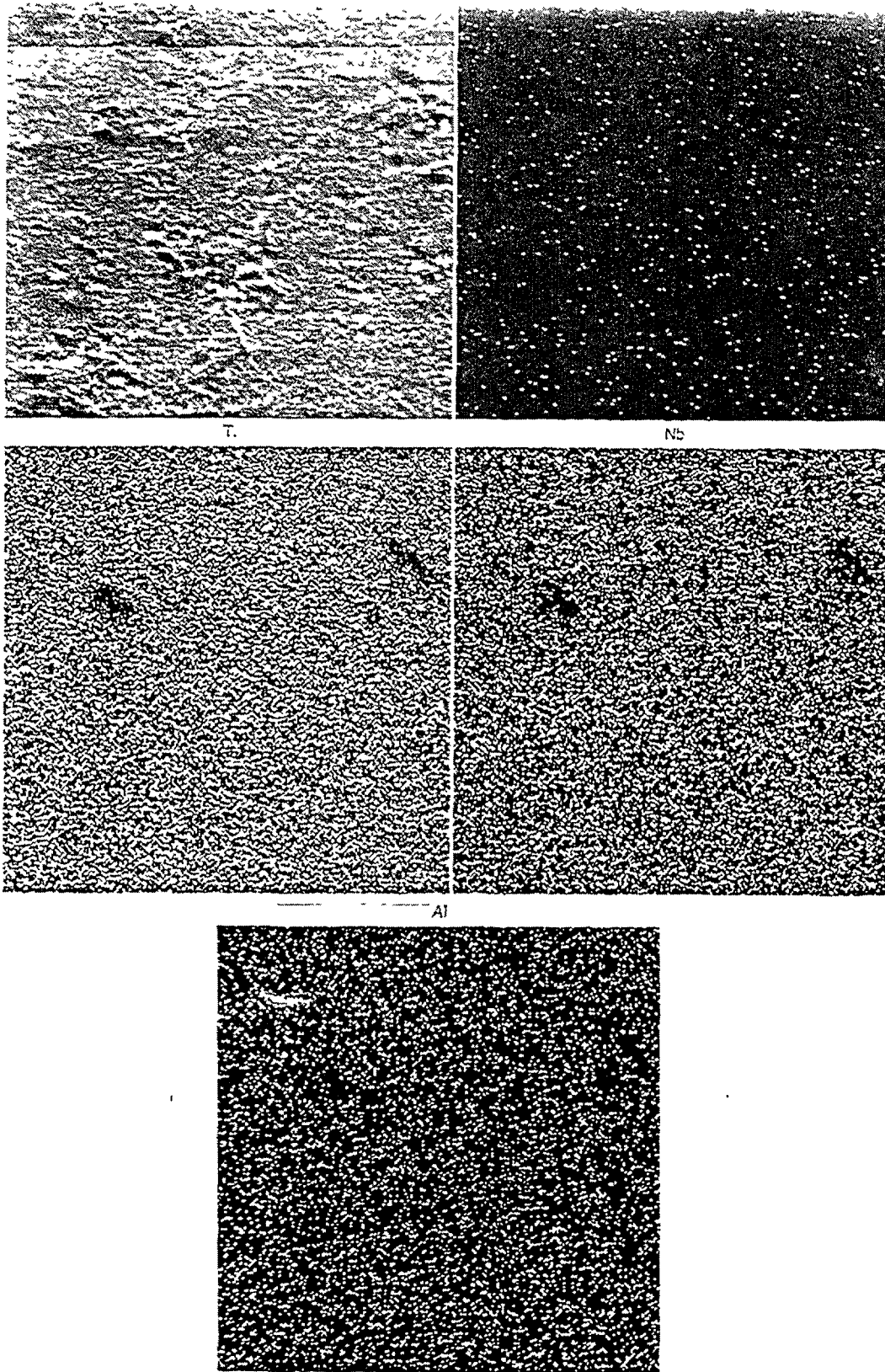


FIG. 52. SEM micrograph and X ray area scan maps of N, Ti, Nb and Al for the plasma nitrided Ti-25Al-11Nb alloy.

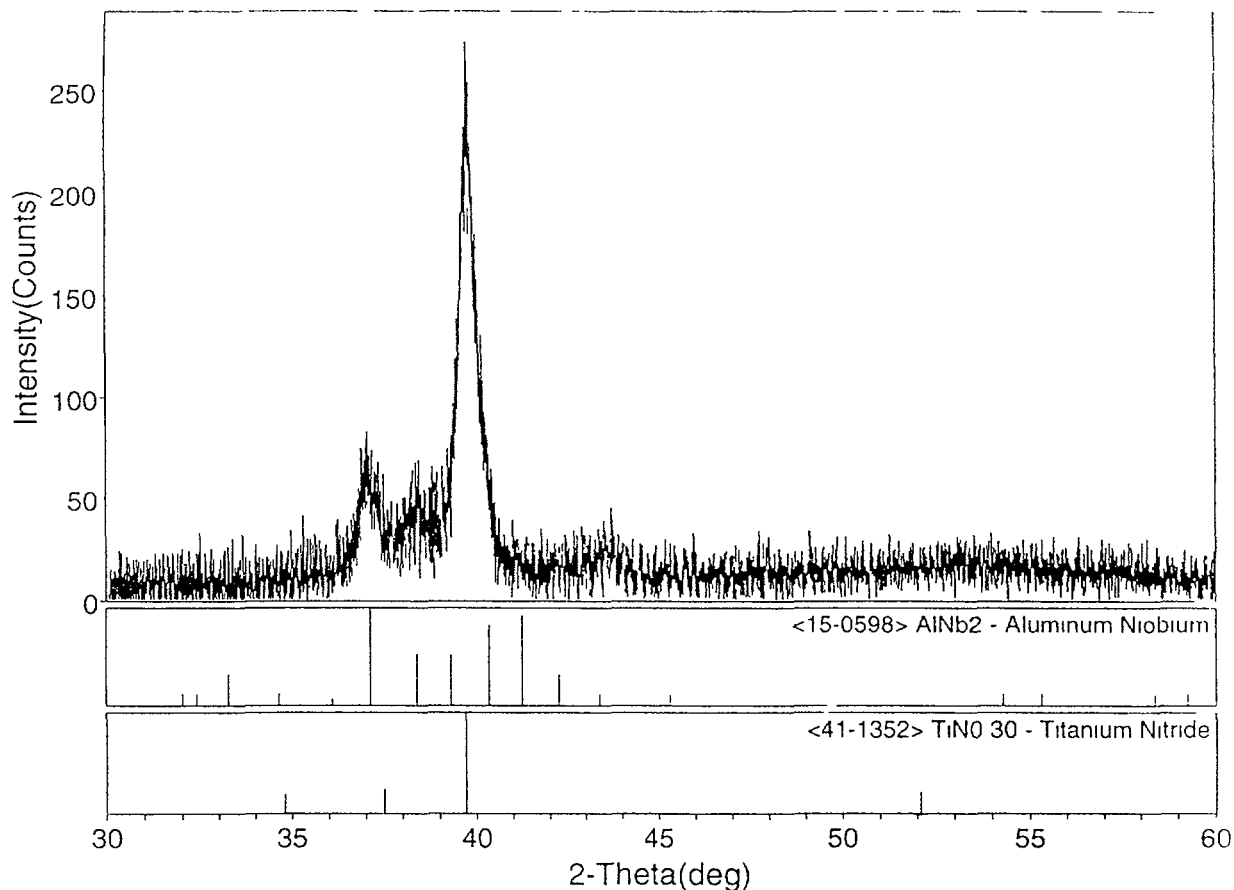


FIG. 53. X ray diffraction method of plasma nitrided Ti-25Al-11Nb alloy.

4.16.7. Oxidation kinetics

Oxidation tests were carried out at 800⁰C in air for 100 hours. The weight changes vs. time plots for the oxidation of the base alloys Ti-25Al-11Nb (B1), Ti-24Al-20Nb (B2), and Ti-22Al-20Nb (B3) are shown in Fig. 54. The oxidation kinetics appear to be parabolic in nature. The parabolic rate constants for alloy B1 ($K_p = 3.9 \times 10^{-3} \text{ mg}^2 \text{ cm}^4 \text{ h}^{-1}$) were found to be significantly smaller compared to those of alloy B2 ($K_p = 6.5 \times 10^{-3} \text{ mg}^2 \text{ cm}^4 \text{ h}^{-1}$) and B3 ($K_p = 13 \times 10^{-3} \text{ mg}^2 \text{ cm}^4 \text{ h}^{-1}$).

The weight changes vs. time plots for the oxidation of CrN coated alloys Ti-25Al-11Nb (CrN1), Ti-24Al-20Nb (CrN2), and Ti-22Al-20Nb (CrN3) at the same temperature in air are given in Fig. 55. The oxidation kinetics appears to be parabolic in nature. The parabolic rate constants for alloy CrN1 ($K_p = 2.5 \times 10^{-3} \text{ mg}^2 \text{ cm}^4 \text{ h}^{-1}$) were found to be smaller compared to those of alloy CrN2 ($K_p = 3.5 \times 10^{-4} \text{ mg}^2 \text{ cm}^4 \text{ h}^{-1}$) and CrN₃ ($K_p = 5.15 (10^{-4} \text{ mg}^2 \text{ cm}^4 \text{ h}^{-1})$). The oxidation kinetics for the CrN coated alloys follows a similar trend as for the base alloys, however, the overall weight gain is much lower for CrN coated alloys, indicating the improvement in the oxidation resistance.

The weight changes vs. time plots for oxidation of plasma nitrided alloys Ti-25Al-11Nb (PN1), Ti-24Al-20Nb (PN2), and Ti-22Al-20Nb (PN3) at 800⁰C in air are depicted in Fig. 56: The oxidation kinetics appears to be parabolic in nature. The parabolic rate constant for alloy PN1 ($K_p = 1.6 \times 10^{-3} \text{ mg}^2 \text{ cm}^4 \text{ h}^{-1}$) were found to be smaller compared to those of alloy PN2 ($K_p = 2.6 \times 10^{-3} \text{ mg}^2 \text{ cm}^4 \text{ h}^{-1}$) and PN3 ($K_p = 8.7 \times 10^{-3} \text{ mg}^2 \text{ cm}^4 \text{ h}^{-1}$). The alloy PN1 again shows

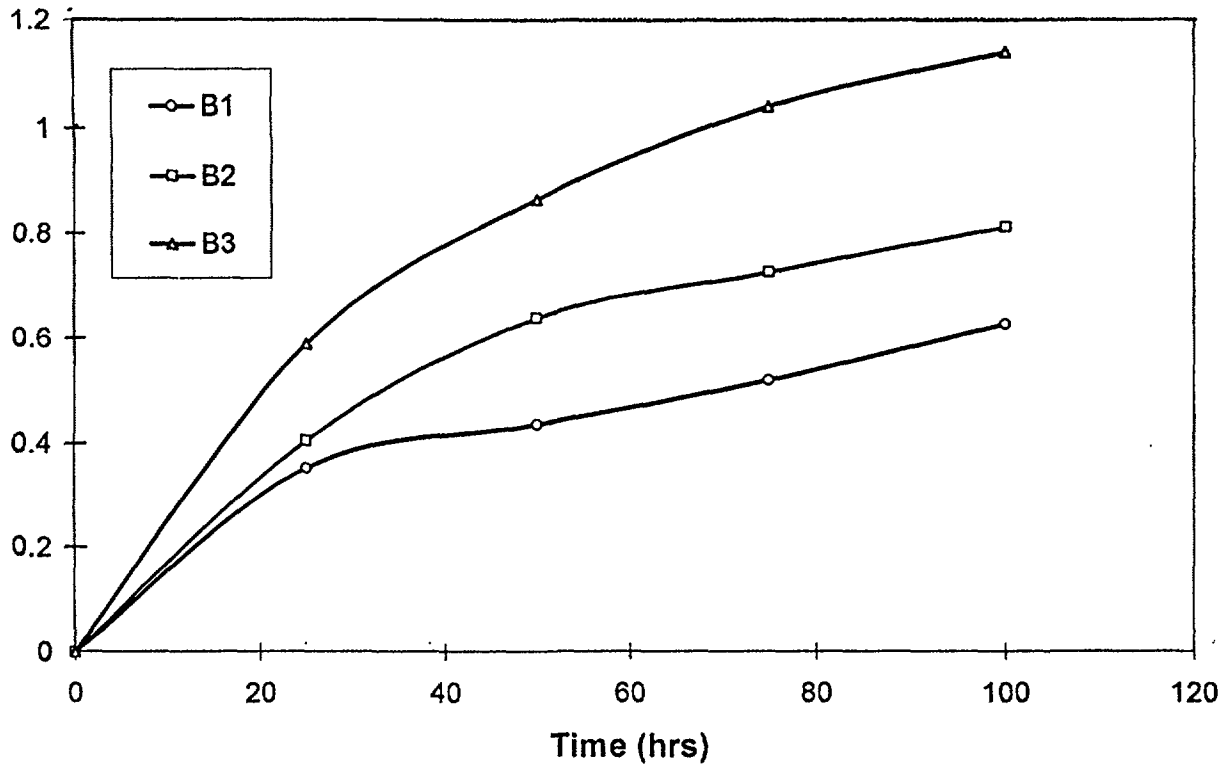


FIG. 54. Oxidation of base Ti_3Al-Nb alloys at 800 °C in air.

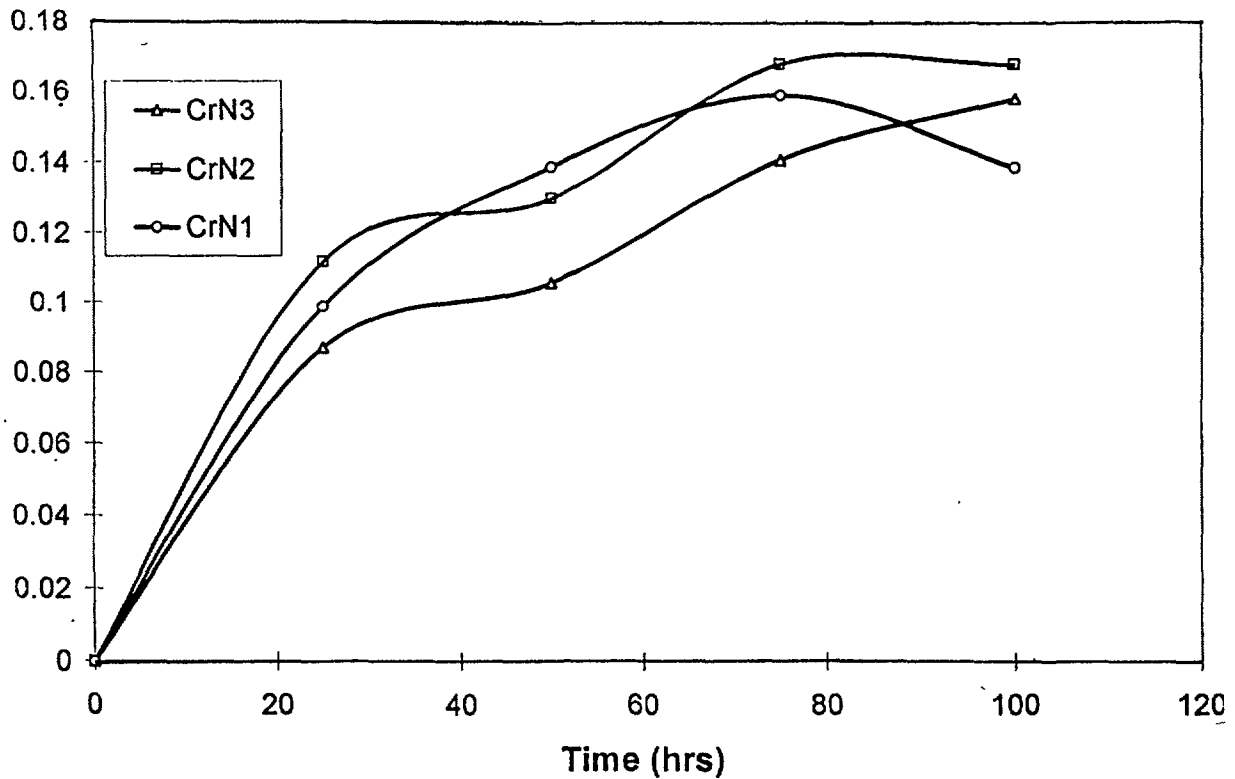


FIG. 55. Oxidation of Cr-Nitrided Ti_3Al-Nb alloys at 800 °C in air.

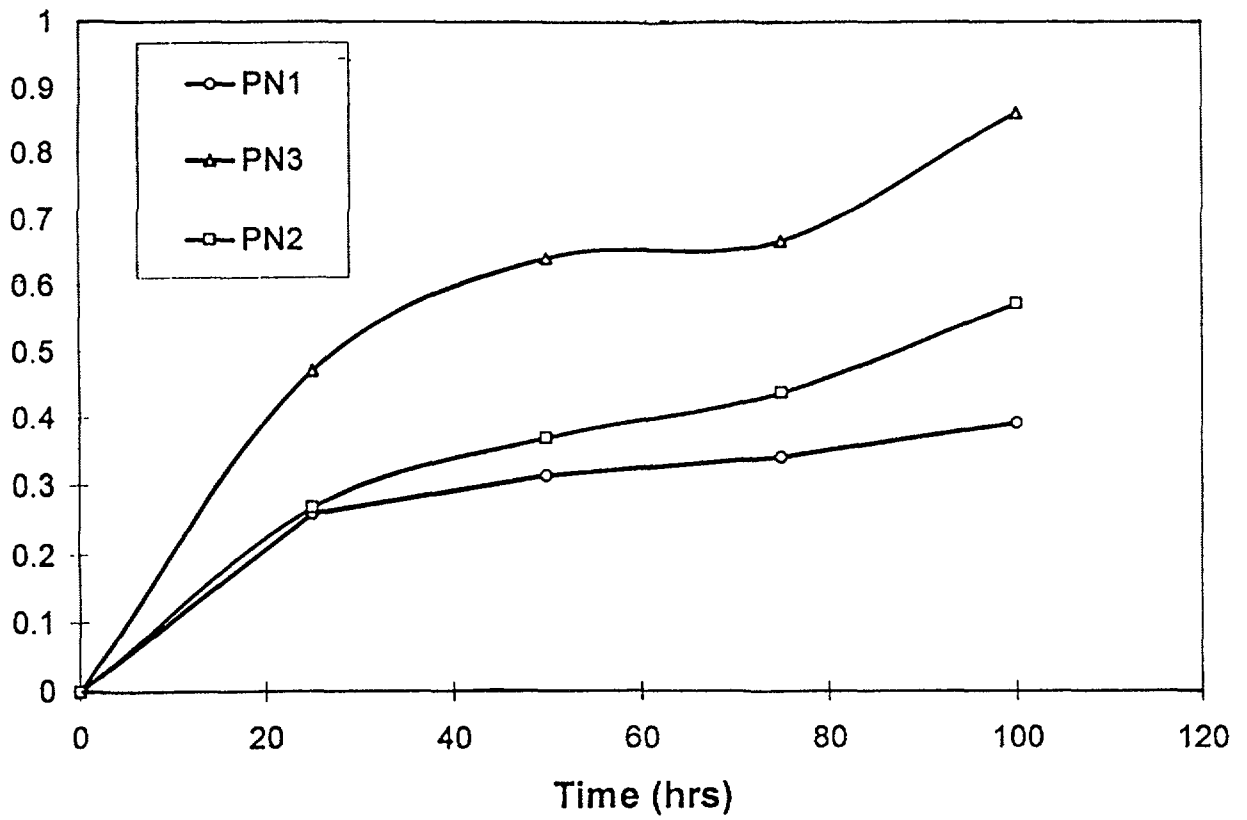


FIG. 56. Oxidation of plasma nitrated Ti_3Al-Nb alloys at $800^\circ C$ in air.

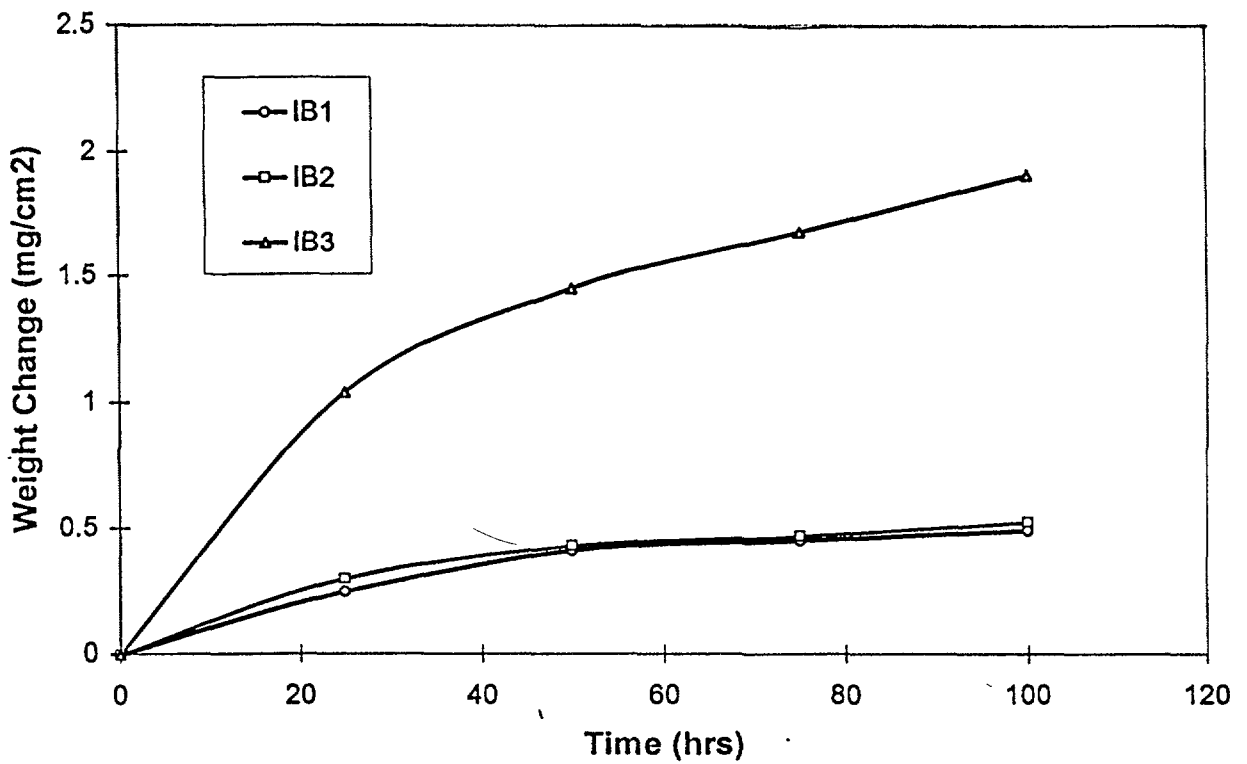


FIG. 57. Oxidation of Al/Ar ion beam mixed Ti_3Al-Nb alloys at $800^\circ C$ in air.

the lowest oxidation rate among the three alloys. The overall weight gain is lower for plasma nitrated alloys than the base alloys, however, it is higher than the chromium nitrated coated alloys. This shows that the nitrated coating using plasma technique improves the oxidation resistance of the base alloys but it is relatively less effective than the CrN coating made by plasma arc process.

Figure 57 shows the weight change vs. time plots for the oxidation of Al/Ar⁺ ion beam mixed alloys Ti-25Al-11Nb (IB1), Ti-24Al-20Nb (IB2), and Ti-22Al-20Nb (IB3). The oxidation kinetics appears to be parabolic in nature. The parabolic rate constant for alloy IB1 ($K_p = 3.3 \times 10^{-3} \text{ mg}^2 \text{ cm}^4 \text{ h}^{-1}$) was found to be smaller compared to those of alloy IB2 ($K_p = 3.6 \times 10^{-3} \text{ mg}^2 \text{ cm}^4 \text{ h}^{-1}$) and IB3 ($K_p = 41 \times 10^{-3} \text{ mg}^2 \text{ cm}^4 \text{ h}^{-1}$). The weight change follows a similar trend as in the case of the base alloy. The weight gains for the coated alloys are lower than the base alloys, however, the improvement in oxidation resistance is lower than the plasma nitrated or CrN plasma arc process. In the case of Ti-22Al-20Nb (IB3) sample, higher weight gains are found. This might be due to some defects, which were found in the base alloy before coating.

It is of great interest to note that the chromium nitride coated samples were found to have even better oxidation resistance than the plasma nitrated and Al/Ar⁺ ion beam mixed samples. Thus it can be said that the chromium nitride coating can be highly beneficial for improving the oxidation resistance of these alloys at high temperatures.

Scanning electron micrographs of the base alloy Ti-25Al-11Nb, CrN coated alloy, plasma nitrated and ion beam mixed Al coated alloy specimens, after oxidation in air at 800°C for 100h are depicted in Fig. 58. Local growth of oxide scale is evident in the case of the base alloy (Fig. 58a). Oxide scales formed on chromium nitrated and Al/Ar⁺ ion beam mixed specimen was uniform and compact. Some pores in oxide scale were found in the case of plasma nitrated Ti-25Al-11Nb specimen (Fig. 58c).

Figure 59 shows the oxide morphologies of the base alloy Ti-24Al-20Nb, CrN coated, plasma nitrated and ion beam mixed Al coated specimens, after oxidation in air at 800°C for 100 h. Dense pillar-like grains of oxide can be seen on CrN sample (Fig. 59b). Oxide scale was found to be compact and uniform in the case of the base alloy, plasma nitrated and ion beam mixed specimens. However, some pores in oxide scale were also found in the case of plasma nitrated specimen (Fig. 59c).

The scanning electron micrographs of base alloy Ti-22Al-20Nb, CrN coated, plasma nitrated and ion beam mixed Al coated alloy specimens, after oxidation in air at 80 for 100 h are depicted in Fig. 60. Oxide scale characteristics were similar to that observed in the case of Ti-25Al-11Nb alloys.

4.17. FORMATION OF WEAR-RESISTANT COMPOSITE SURFACE LAYERS

Layer composition: C-Me (Zr, Ti, Ta), C-N and B-N.

Substrates: AISI M2 high speed steel (0.86% C, 6.0% W, 5.0% Mo, 4.1% Cr, 1.9% V, 0.5% Co, in wt.%); Al and Fe; carbon steel.

Ion beam technologies:

— Conventional ion implantation (CII).

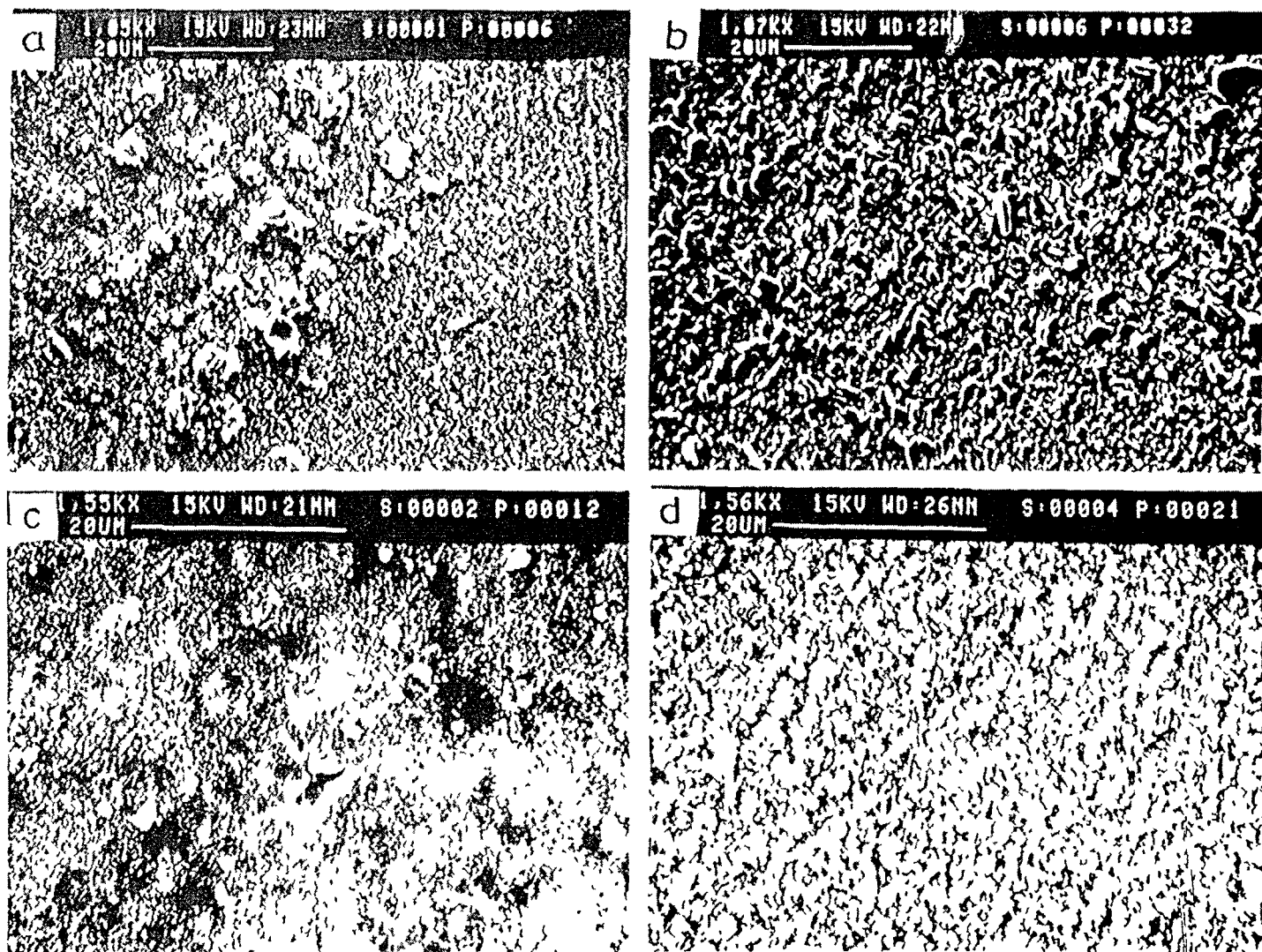


FIG 58 SEM micrographs showing the oxide morphology after oxidation in air for 100 h at 800 °C, (a) base Ti-25Al-11Nb, (b) CrN coated, (c) plasma nitrided, and (d) Al/Ar⁺ ion beam mixed alloys

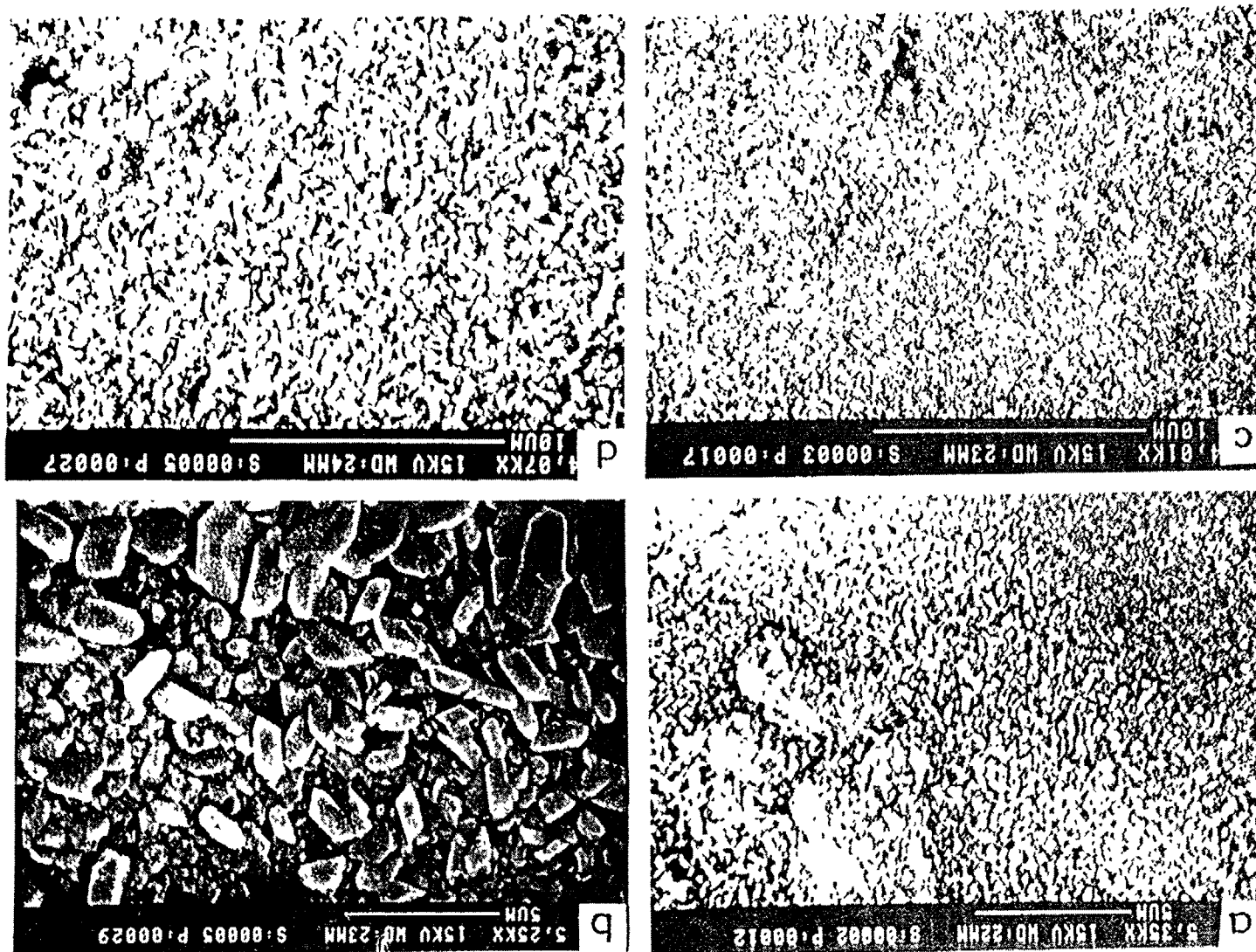


FIG. 59. SEM micrographs showing the oxide morphology after oxidation in air for 100 h at 800 °C, (a) base Ti-24Al-20Nb, (b) CrN coated, (c) plasma nitrided, and (d) Al/Ar⁺ ion beam mixed alloys.

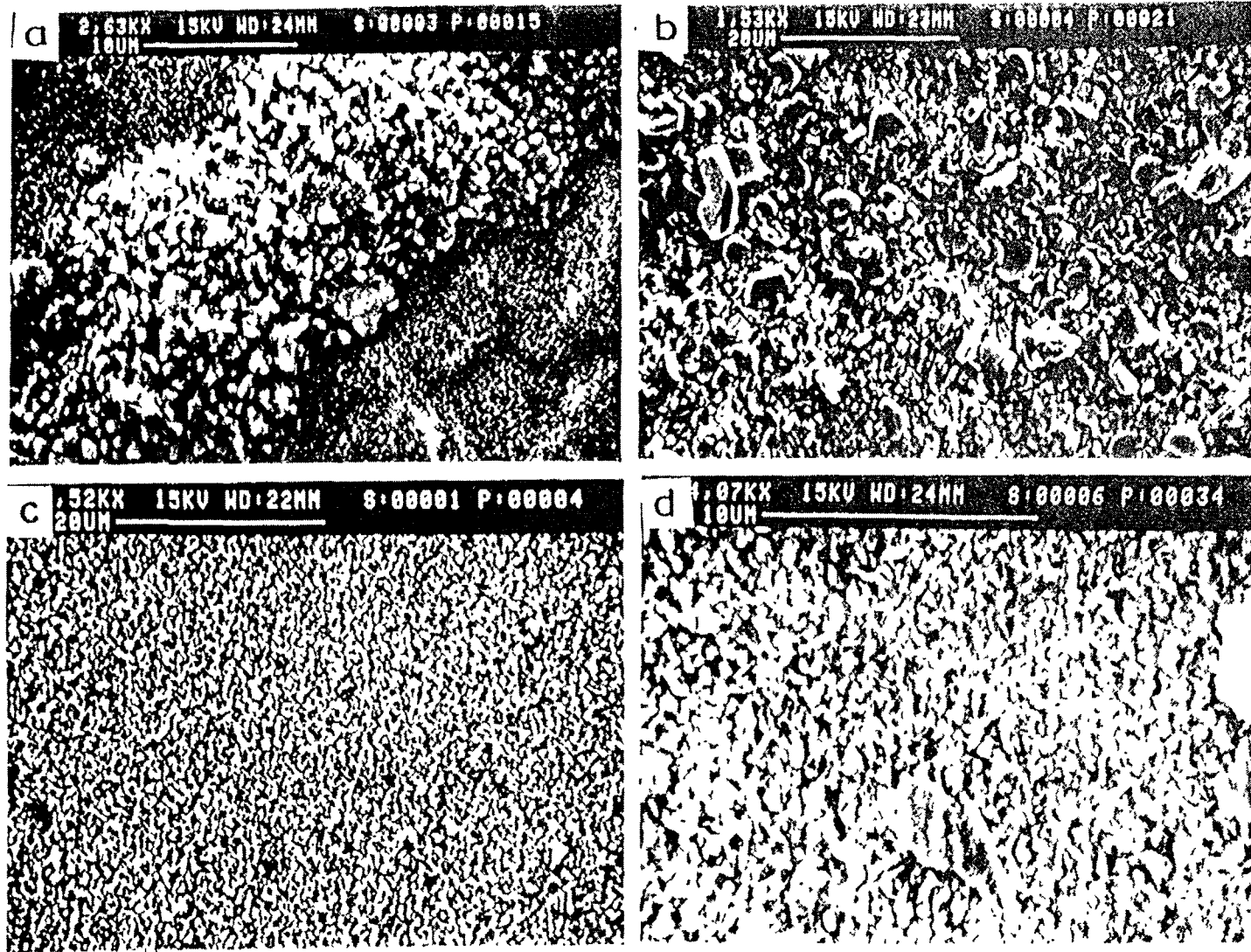


FIG. 60. SEM micrographs showing the oxide morphology after oxidation in air for 100 h at 800 °C, (a) base Ti-22Al-20Nb, (b) CrN coated, (c) plasma nitrided, and (d) Al/Ar⁺ ion beam mixed alloys.

- Double ion implantation (DII) | high current ion implantation (HCII).
- Coatings deposition by SVETLJACHOK source.

TREATMENT REGIMES

Method/Source	Ion	Energy, keV	Current density, $\mu\text{A}/\text{cm}^2$	Dose, ions/ cm^2	Temperature, $^{\circ}\text{C}$
CII	B + N	24,60 + 75,92	1.5 + 1.5	$3 \cdot 10^{17} + 3.6 \cdot 10^{17}$	RT
HCII	N + B	1 + 20	3500 + 530	$7 \cdot 10^{19} + 2 \cdot 10^{18}$	500
MEVVA	C + Zr	20 + 25	20 + 40	$2 \cdot 10^{17} + 2 \cdot 10^{17}$	350
SVETL.	C + Me (Zr, Ta, Ti)	20 + 25	11 + 6	$2 \cdot 10^{17} + 2 \cdot 10^{17}$	RT

Auger electron spectroscopy (AES); X ray diffraction (XRD); glancing X ray diffraction (GXR); transmission electron microscopy (TEM); conversion electron Mossbauer spectroscopy (CEMS, scanning depth of 0.1(μm), conversion X ray Mossbauer spectroscopy (CXMS, scanning depth of 10(μm); X ray photoelectron spectroscopy (XPS); microhardness and nanohardness, friction (pin-on-plane and pin-on-disk), and wear measurements were used.

4.17.1. Element composition

- DII and coating deposition by SVETLJACHOK source allow to form composite uniform and layer surface structure with elements concentration strongly depending on irradiation energy, current density, dose and sequence of implantation;
- HCII of nitrogen and boron leads to deep (up to 20 μm) penetration of nitrogen into AISI M2 steel and forms surface boron layer with thickness of about 0.3 μm on top of nitrogen containing layer;
- The forming profiles of nitrogen and boron strongly depend on sequence of implantations by HCII methods. This is due to strong sputtering during N implantation and boron surface accumulation during B implantation;
- Carbon coating with thickness of up to 0.25 μm containing up to 20 at.% of metal (Zr, Ta, Ti) by SVETLJACHOK source.

4.17.2. Phase composition and microstructure

- (1) Phase composition of near-surface (0.1 μm , GXR, CEMS) and deep (~10 μm , CXMS) layers (Table XX) formed by HCII is superposition of $\epsilon\text{-Fe}_3\text{N}$, $\alpha''\text{-Fe}_{16}\text{N}_2$, $\alpha\text{-Fe}$ (C, N) and FeB phases.
- (2) Irradiation using SVETLJACHOK source leads to formation of amorphous carbon coating with ZrC carbide precipitates in it and $\chi\text{-Fe}_2\text{C}$ carbide in interface of coating and substrate.
- (3) AES and XPS spectra of iron after DII of boron and nitrogen are indicative of possible boron nitrides formation in the concentration region of 10–18 at.% after successive boron and nitrogen CII.

TABLE XX. PHASE COMPOSITION OF AISI M2 STEEL AFTER HCII OF NITROGEN AND BORON IONS

Sample	depth μm	share in spectrum, %
N	0.1	$\alpha\text{-Fe(C)}$ 95, $\gamma\text{-Fe(C)}$ 5
	0.1	$\alpha\text{-Fe(C,N)}$ 76, $\gamma\text{-Fe(C,N)}$ 3, $\epsilon\text{-Fe}_3\text{N}$ 21
	10	$\alpha\text{-Fe(C,N)}$ 66, $\gamma\text{-Fe(C,N)}$ 4, $\epsilon\text{-Fe}_3\text{N}$ 20, $\alpha''\text{-Fe}_{16}\text{N}_2$ 10
N + B	0.1	$\alpha\text{-Fe(C,N)}$ 55, $\gamma\text{-Fe(C,N)}$ 4, $\epsilon\text{-Fe}_3\text{N}$ 29, $\alpha''\text{-Fe}_{16}\text{N}_2$ 6, FeB 7
	10	$\alpha\text{-Fe(C,N)}$ 49, $\gamma\text{-Fe(C,N)}$ 6, $\epsilon\text{-Fe}_3\text{N}$ 36, $\alpha''\text{-Fe}_{16}\text{N}_2$ 10

4.17.3. Mechanical properties

- (1) Double HCII of nitrogen and boron increases hardness and decreases friction coefficient by a factor of 2. The enhanced hardness is observed up to a depth of 20 μm .
- (2) HCII of nitrogen greatly changes roughness of steel from 0.01 μm to 0.6 μm due to strong sputtering by nitrogen ions. Additional boron implantation decreases roughness down to 0.25 μm due to deposition of boron film.
- (3) Decrease of friction coefficient of AISI M2 steel by a factor of 6 down to 0.1 and increase of wear-resistance by a factor of 4 after irradiation using SVETLJACHOK source.
- (4) High hardness of C–Zr composite layers formed by SVETLJACHOK source.
- (5) Increase of aluminium lifetime by a factor of 100 after deposition of carbon coating in nitrogen atmosphere due to possible formation of C–N bonds.

From the above it may be concluded that:

- Composite surface layers formed by double HCII and by SVETLJACHOK source possess beneficial mechanical properties (high hardness and wear-resistance, low friction coefficient).
- Double ion implantation of boron and nitrogen into iron is possible method of BN nitride formation.
- Comparison analysis of high speed steel modified by various methods (MEVVA, HCII, SVETLJACHOK) has shown that the composite carbon 20Zr80C layers formed by SVETLJACHOK source are the most wear-resistant.

4.18. DETERMINATION OF THE H CONTENT IN DIAMOND FILMS GROWN BY CVD AND ITS INFLUENCE ON THE COEFFICIENT OF THERMAL CONDUCTIVITY (K) OF THE FILMS

The thin films of diamond are grown using chemical vapour deposition techniques. The hot filament chemical vapour deposition (HFCVD) technique is used to grow the films of the thickness ranging from 3–40 micron. The detailed diagram of the deposition apparatus is shown in Fig. 61. A detailed structural, electrical and mechanical characterization of the films have been carried out. Various deposition parameters are optimized so as to grow the state-of-the-art films. We observe that the deposition pressure is a very important parameter controlling the non-diamond impurities in the films. The films grown at low deposition pressure (20–40 torr) show white translucent colour with almost zero non diamond carbon impurities as observed by Raman spectroscopy. The X ray diffraction (XRD) is employed to

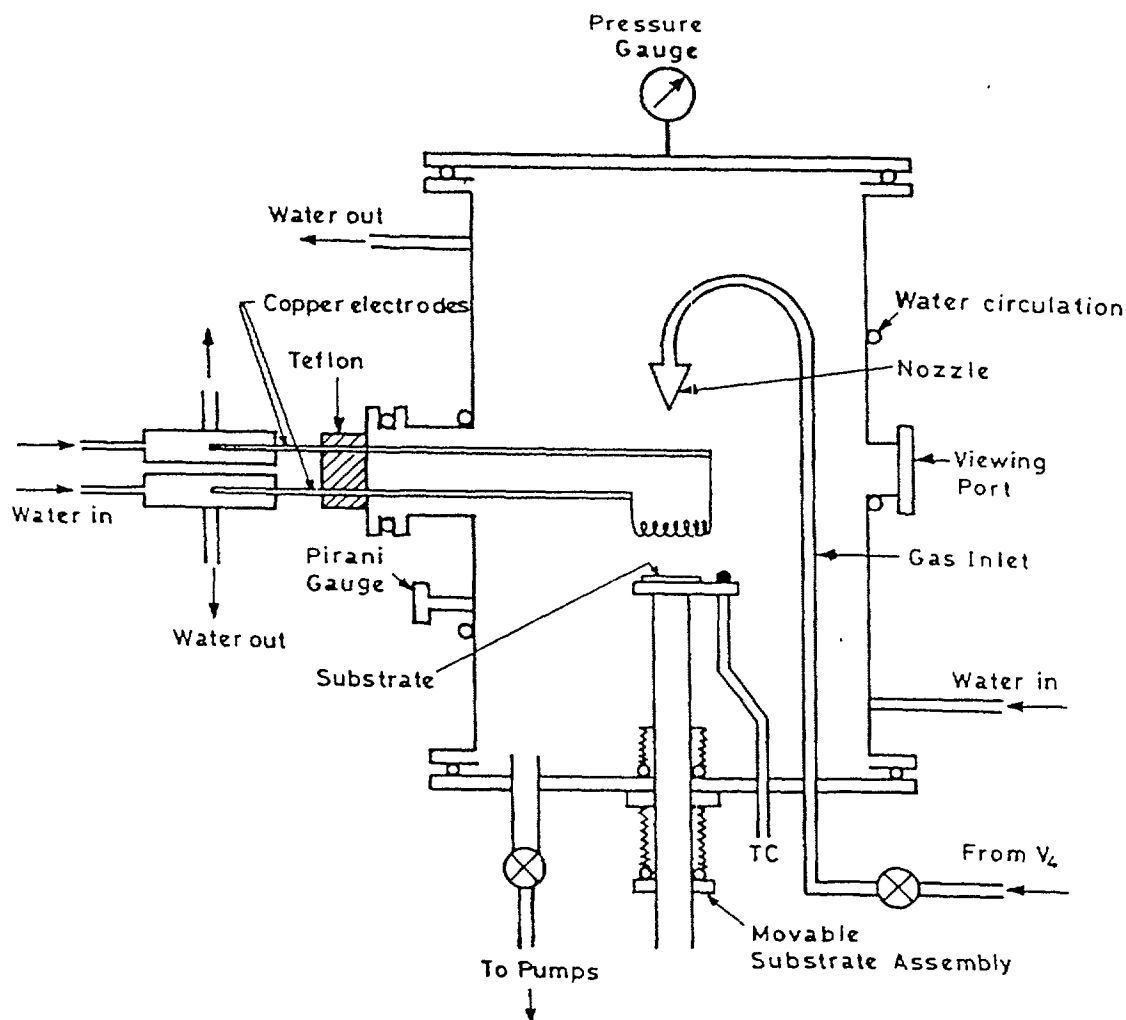


FIG. 61. The schematic diagram of the HFCVD apparatus.

determine the crystal structure of the films. The films have polycrystalline morphology with a dominantly cubic crystal structure. The lattice constant of the CVD diamond films are 3.52 \AA . Raman spectra as presented in Fig. 62 show the presence of a sharp line at 1332 cm^{-1} indicating a sp^3 bonded carbon network. The FWHM of the Raman line is $5\text{--}7 \text{ cm}^{-1}$ showing the excellent quality of the crystallites.

The films grown at higher deposition pressure indicate the presence of non-diamond carbon in the films. The non-diamond carbon is characterized by the presence of a broad Raman band at 1500 cm^{-1} . The intensity of this non-diamond band increases significantly in the films grown at 100–140 torr. An increase in the non-diamond carbon in the films is accompanied with an increase in the H content of the films (Table XXI).

TABLE XXI. THE H CONTENT IN DIAMOND SHEETS GROWN IN HFCVD APPARATUS

Serial no	Deposition pressure (torr)	H content (at. %)
1.	20 torr	0.2
2.	40 torr	0.25
3.	60 torr	0.35
3.	80 torr	0.65
5.	100 torr	1.05
6.	120 torr	1.35

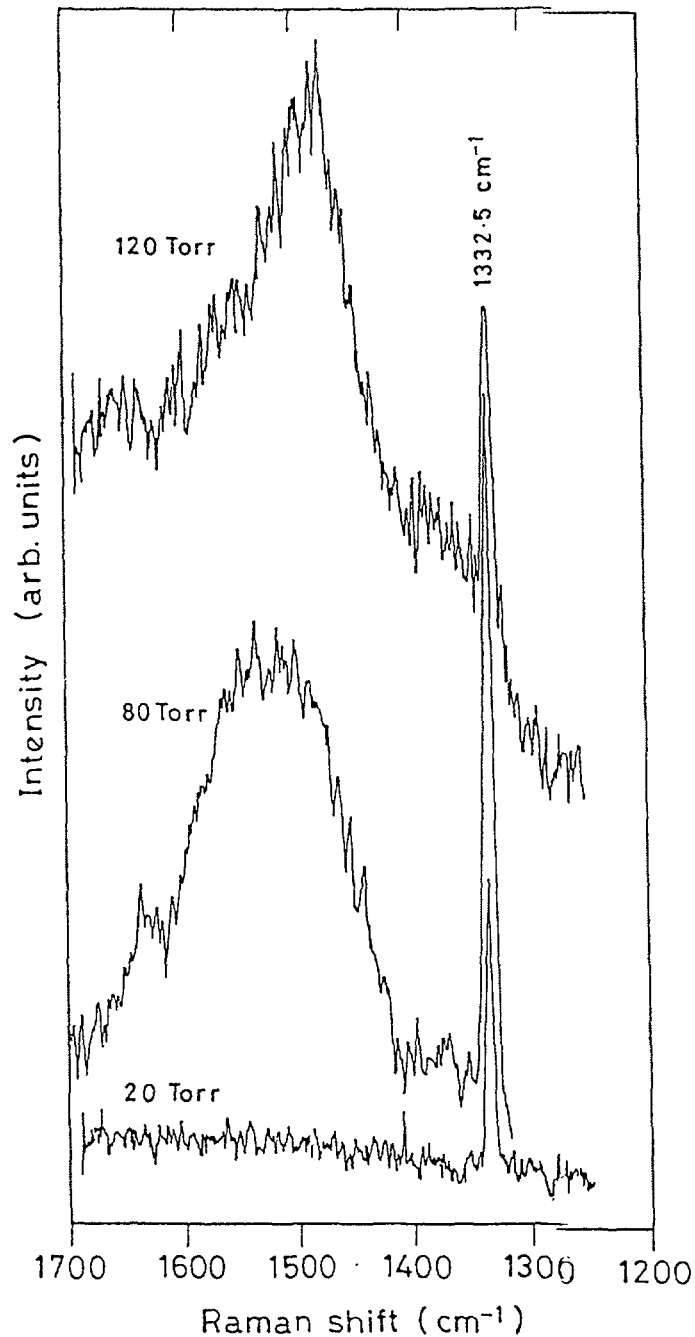


FIG. 62. Raman spectra of the diamond sheets grown at various pressure.

This may indicate the fact that the Hydrogen impurities in the films may be bonded with the non-diamond carbon. The H impurities are measured using elastic recoil detection analysis (ERDA). A Ni ion beam of 77 MeV is used for the ERDA measurements. The variation in H content correlate with the various electrical and thermal characteristics of the films. The electrical conductivity (σ_{300}) measurements are carried out on the films in sandwich configuration to avoid the surface leakage currents. The σ_{300} values are very sensitive to the presence of H impurities in the samples. The coefficient of the thermal conductivity (K) of the films decreases as the H content in the films increase. An interesting correlation between the H content in the films and the value of K is shown in Table XXII.

TABLE XXII. THE THERMAL CONDUCTIVITY VALUES AND ATOMIC % OF H IN THE SHEETS

serial no	deposition pressure	atomic % of H	K (watt/cm °K)
1	20 torr	0.2	15
2	30 torr		
3	40 torr	0.25	12
4	60 torr	0.35	10
5	80 torr	0.65	8
6	100 torr	1	5

In addition to the above, serious attempts have also been made to enhance the adhesion of the diamond films with the stainless steel substrates for the diamond tool applications. We find that a buffer layer of a mixture of NiCr prove to be very effective in enhancing the adhesion of the films. In the co-ordination program the Raman spectra and ERDA analysis are carried out on the CrN films supplied by the agency. The CrN coated substrates have been coated with the CVD diamond films. The characteristics of the diamond coated on CrN deposited SS substrates are compared with the films deposited on bare SS.

5. ROUND ROBIN TEST ON EVALUATION AND PERFORMANCE OF ION BEAM ASSISTED CHROMIUM NITRIDE COATING ON STAINLESS STEEL SUBSTRATE

Stainless steel coupons of 20 mm diameter and 2 mm thickness were cut from a controlled lot of an AISI type 304 stainless steel bar. These samples were then polished to a mirror finish using a series of standard metallurgical polishing steps. 300 polished samples were then loaded into a planetary system for rotation and translation to receive a uniform chromium nitride coating.

IBAD system of SPIRE Corporation, USA, was used for this purpose, which is shown schematically in Fig. 63. The system consists of a chamber with two independent systems, one for deposition of Cr by electron beam evaporation and, from the other, an intense beam of N ions is bombarded at an operating voltage of 1000 eV. Vacuum level of the chamber was maintained at 5×10^{-7} torr. Extensive experience at SPIRE Corporation has shown that a chromium rich chromium nitride coating is better than stoichiometric CrN for tribological applications. Also, temperature of the substrate has been controlled to obtain the best coating performance.

Chromium nitride was chosen as the coating of choice for several reasons: a) it is a fully developed and optimized coating offered by SPIRE Corporation with extensive laboratory testing behind it, b) it is a hard, wear-resistant coating for challenging industrial applications and, c) it is chemically inert and is ideal coating for corrosion testing.

The samples are characterized by RBS, AES, AFM, XPS, XRD and Glancing XRD methods and evaluated by tribological, microhardness, dynamic micro-indentation, impact, scratch, dry sliding, friction wear and corrosion tests.

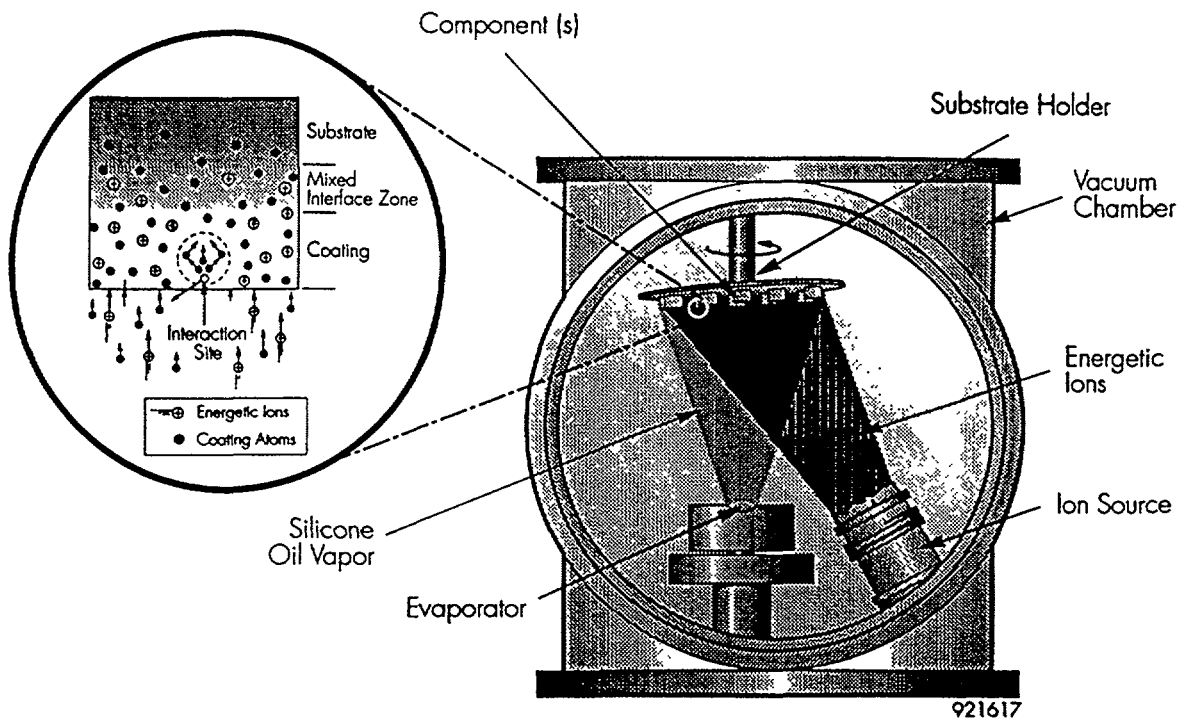


FIG. 63. Experimental set-up of IBAD.

5.1. CHARACTERIZATION OF CHROMIUM NITRIDE COATINGS

5.1.1. Rutherford backscattering analysis (RBS)

The composition and thickness of the chromium nitride film on stainless steel samples were analysed by Rutherford Backscattering (RBS) method. Ion beams of high energy, collimated to 2-mm diameter, were impinged normally on the targets placed inside a scattering chamber. A silicon surface barrier detector (with a resolution of ~ 11 keV for 5.5 MeV α -particles) mounted at a backward angle of 168° was used to detect the backscattered particles. Backscattered spectra were acquired by PC based multichannel analyser. The backscattered spectrum of the chromium nitride film obtained using 3 MeV α -particles is shown in Fig. 64. The step observed at the high energy end corresponds to Cr in the chromium nitride film whereas the peak can be attributed to the presence of an interfacial thin film of Cr. However, the backscattered signal due to N is not discernible. The thickness of the film calculated by taking into consideration the energy separation between the front and rear edges of the Cr step in the spectrum depicted in Fig. 64 is ~ 1.3 μm . The stopping power required for estimating the thickness has been calculated using TRIM95 on the basis of composition determined earlier.

The backscattered spectrum of the chromium nitride film acquired using ^{14}N (p,p) ^{14}N resonance reaction at 1.74 MeV is shown in Fig. 65. The first step at the high-energy end in this spectrum is due to Cr in the chromium nitride film, the second due to Fe in the backing material whereas the peak corresponds to N in the film. The cross-section of the resonance reaction at 1.74 MeV has been reported to be 145 mb/sr. In order to estimate the thickness, the film was profiled by incrementing the energy of the beam from 1.74 MeV onwards in step of 20 keV. The width of this resonance reaction is about 4–6 keV. Thus the reaction yield at the resonance is sensitive to detector resolution, ion energy and thickness of the film. Therefore, this energy was not considered suitable for determining the composition. However, the cross-

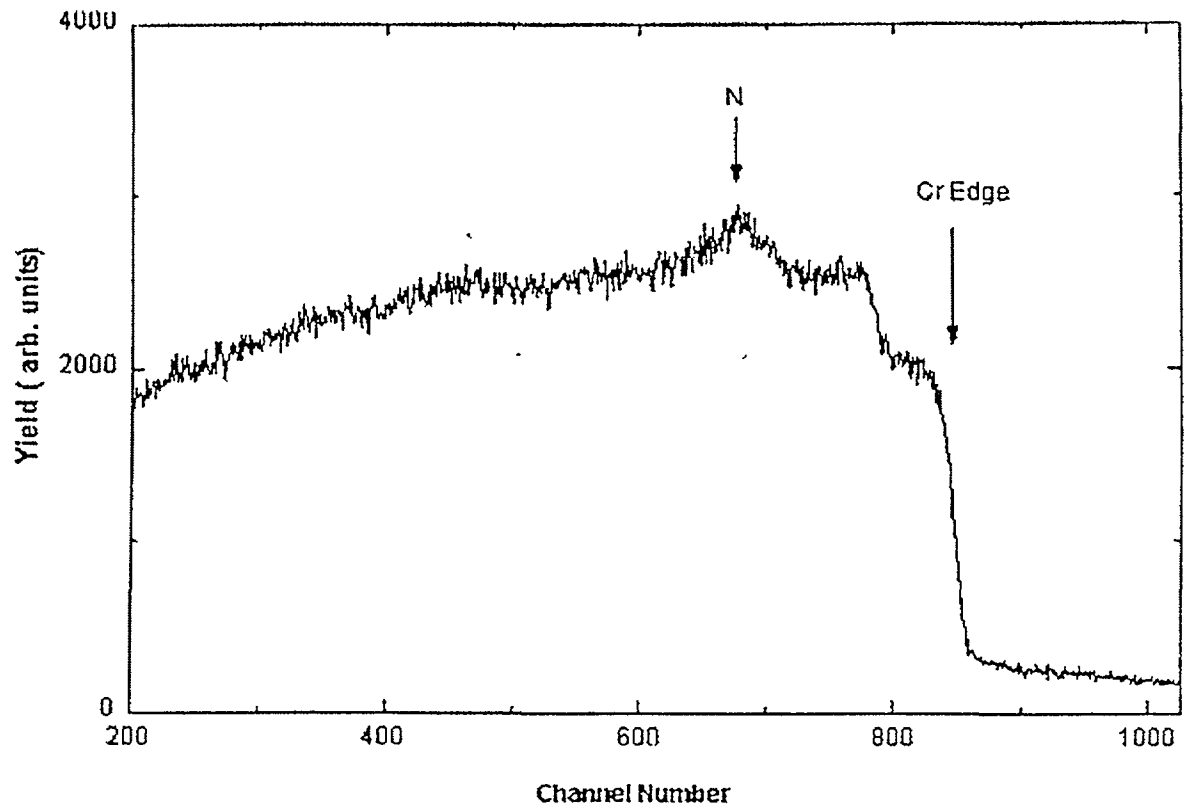


FIG 64 Backscattered proton spectrum of ion beam assisted CrN film on SS ($E_{\alpha} = 3 \text{ MeV}$)

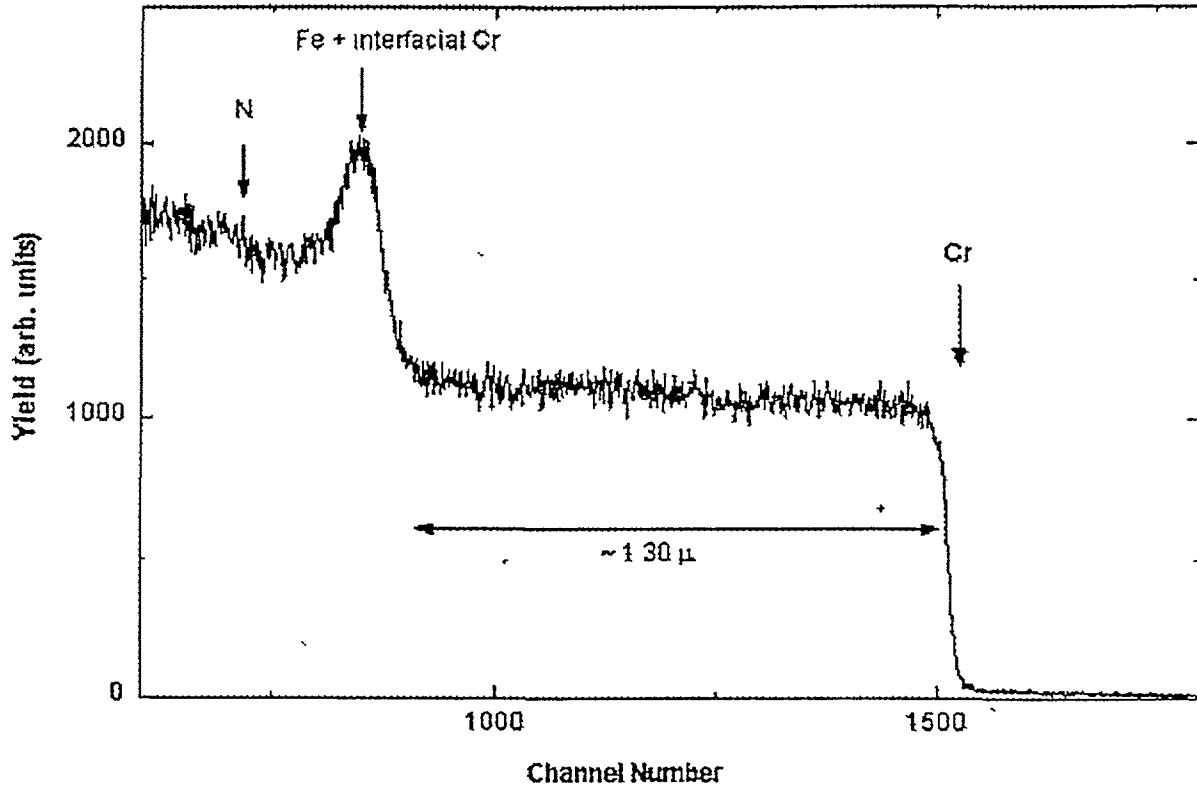


FIG 65 RBS spectrum of IB assisted CrN film on SS ($E_p = 1.711 \text{ MeV}$)

section of the resonance reaction is almost constant (~95 mb/sr) in the energy region of 1.6 to 1.7 MeV. Hence, $^{14}\text{N}(\text{p,p})^{14}\text{N}$ resonance reaction at different proton energies in this region was utilized to estimate the composition of the film. The composition of the film (Cr/N) ratio, estimated using the formula:

$$Y_{\text{Cr}}/Y_{\text{N}} = N_{\text{Cr}} \cdot \sigma_{\text{Cr}}/N_{\text{N}} \cdot \sigma_{\text{N}}$$

where Y = counts under the N peak or Cr-step and σ = respective scattering cross section.

The composition of the chromium nitride film was found to be $\text{Cr}_{0.75}\text{N}_{0.25}$. The thickness of the film as determined by profiling using $^{14}\text{N}(\text{p,p})^{14}\text{N}$ reaction is in close agreement with this value. The interfacial chromium is not clearly distinguishable while using protons (Fig. 65). This film estimated to be ~1000 could have formed during initial stages of deposition which might be enhancing the adhesion of chromium nitride. This study shows that while $^{14}\text{N}(\text{p,p})^{14}\text{N}$ is suitable for determining composition of films containing low z elements, RBS provides valuable information regarding the film thickness and interfacial regions.

5.1.2. Auger electron spectroscopy (AES)

AES was used to determine the composition and depth profile of chromium nitride coating. The sample was analysed with a PHI 545A scanning Auger microprobe at a base pressure in the vacuum chamber below 1.3×10^{-7} Pa. A static primary electron beam of 3 KeV, 1 μ A and a diameter of about 40 μ m was used. The sample was ion sputtered with 3 KeV Ar^+ ion beam, rastered across an area larger than 5 mm \times 5 mm, with a sputtering rate of about 5 nm/min. The Auger peak-to-peak heights of C(272eV), N(379eV), O(510eV), Cr(529eV), Fe(703eV) and Ni(848eV) as a function of the sputtering time were quantified by applying the relative elemental sensitivity factors: $S_{\text{N}} = 0.32$, $S_{\text{O}} = 0.50$, $S_{\text{Cr}} = 0.32$, $S_{\text{Fe}} = 0.21$ and $S_{\text{Ni}} = 0.29$.

Figure 66 shows the AES depth profile of the as-deposited chromium nitride coating on the stainless steel. The elemental composition of the coating by design doesn't correspond to the stoichiometric CrN with the atomic ratio Cr/N = 1/1. The maximal concentration of the N at the coating/substrate interface is about 27.0 at% and is gradually decreased up to the coating's surface where the concentration is about 22.0 at%. The chromium rich chromium nitride coating with this composition, as the tribological and chemical testing in this paper indicate, has excellent properties and has been developed based on many years of research. The average concentration of C in the coating was about 1 at% and the surface of the chromium nitride film is slightly oxidised.

5.1.3. X ray photoelectron spectroscopy (XPS)

XPS analysis on chromium nitride coated stainless steel substrate was carried out in a Perkin-Elmer 5300 spectrometer with a hemispherical electron energy analyser using Mg K α irradiation. The CrN coating was sputtered using a differentially pumped 3 KeV Ar ion gun at an incidence angle of 45°. The sample was ion sputtered over an area of 5 mm \times 5 mm, with a sputtering rate of about 1.2 nm/min. The size of an analysed area was about 1 mm². The data acquisition was performed by an Apollo work station interfaced with the spectrometer. The peak areas of Cr 2p, N 1s, O 1s and C 1s were registered and the atomic concentration was calculated through a proper area calculation and using correspondent sensitivity factors.

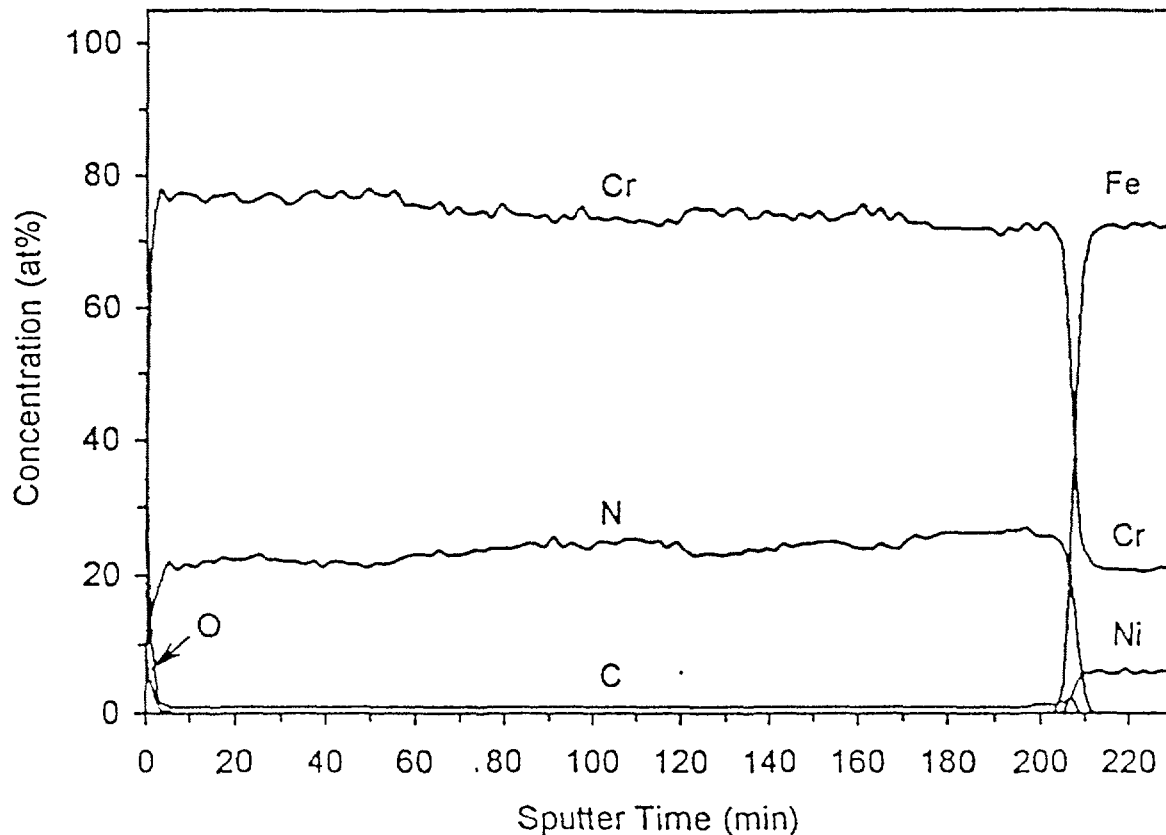


FIG. 66. AES sputter depth profile of the CrN coated SS.

Contrary to the AES results, the XPS analysis showed in the CrN coating besides the carbon the presence of oxygen was also noticed (Fig. 67). In the XPS spectra, the corresponding peaks of N 1s at 396.6 eV (Fig. 67b) O 1s at 529.5 eV (Fig. 67c) and C 1s at 281.9 eV (Fig. 67d) are characteristic for Cr nitride, oxide and carbide, respectively. XPS sputter depth profiling revealed inside of the CrN coating the following composition: 75 at% Cr, 16.0 at% N, 5 at% O and 4 at% C.

5.1.4. X ray diffraction analysis (XRD)

The X ray diffraction of chromium nitride coated SS 304 showed that the structure of chromium nitride coating is amorphous, not crystalline. The amorphous pattern can be observed very clearly from the XRD spectrum, as shown in Fig. 68. X ray diffraction of AISI 304 SS is also shown in Fig. 69, which reveals that chromium nitride coating consists mainly of Cr₂N phase (28 at. % of N) and some quantity of pure Cr is also present in coating. The presence of CrN phase can not be determined unambiguously because CrN diffraction lines overlap that of Cr₂N and substrate γ — (Fe, Cr, Ni).

5.1.5. Glancing angle X ray diffraction

The results of Glancing X ray analysis of chromium nitride coated stainless steel samples are given in Fig. 70. These results confirm the coating as Cr₂N with grain size of 5 ± 2 nm. It also confirms that the thickness of coating is equal to around 1.2 μ m, which is also confirmed by RBS method.

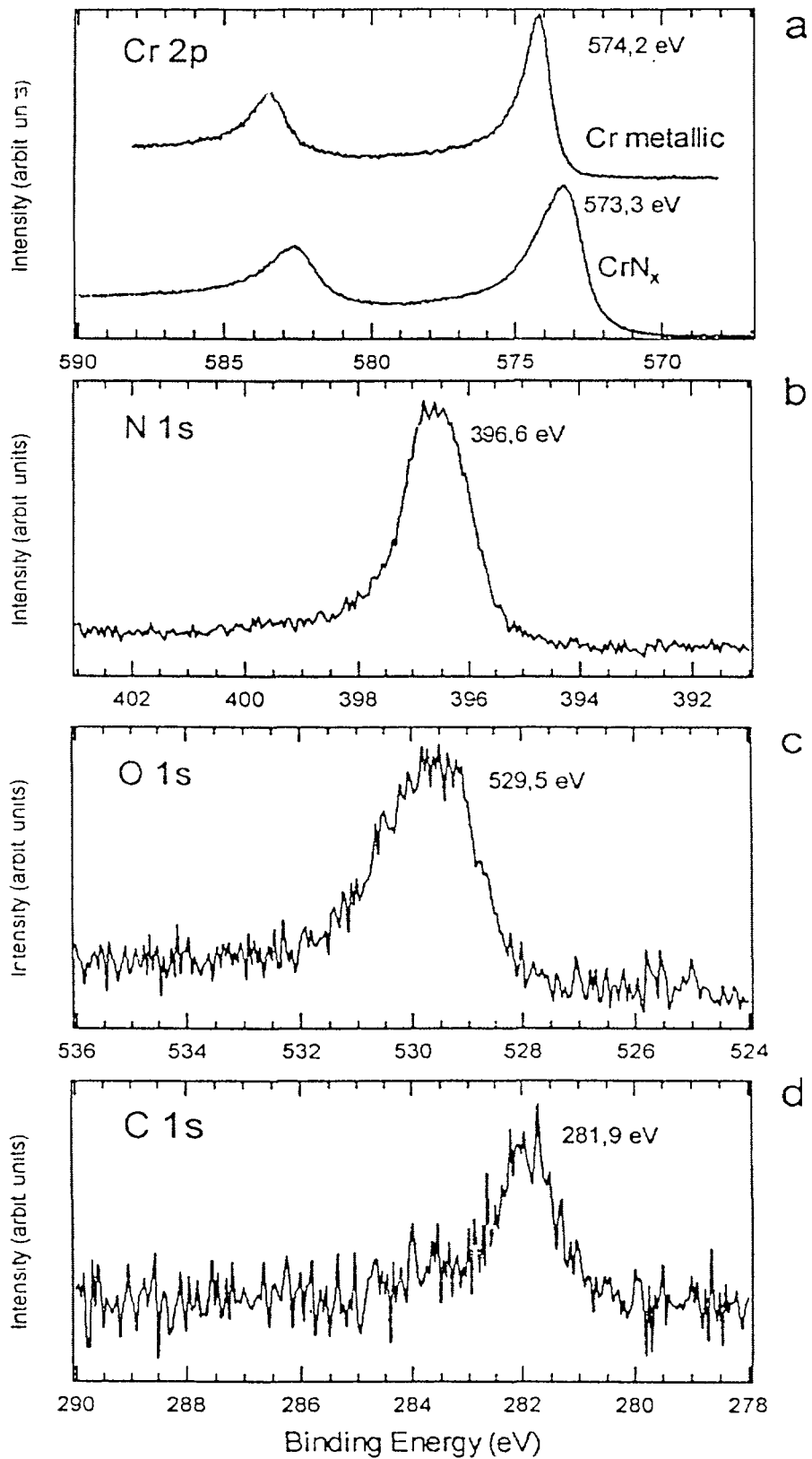


FIG. 67. Photoelectron spectra of (a) Cr 2p, (b) N 1s, (c) O 1s, and (d) C 1s measured in the CrN coating after 60 minutes ion sputtering time in the depth of about 70 nm.

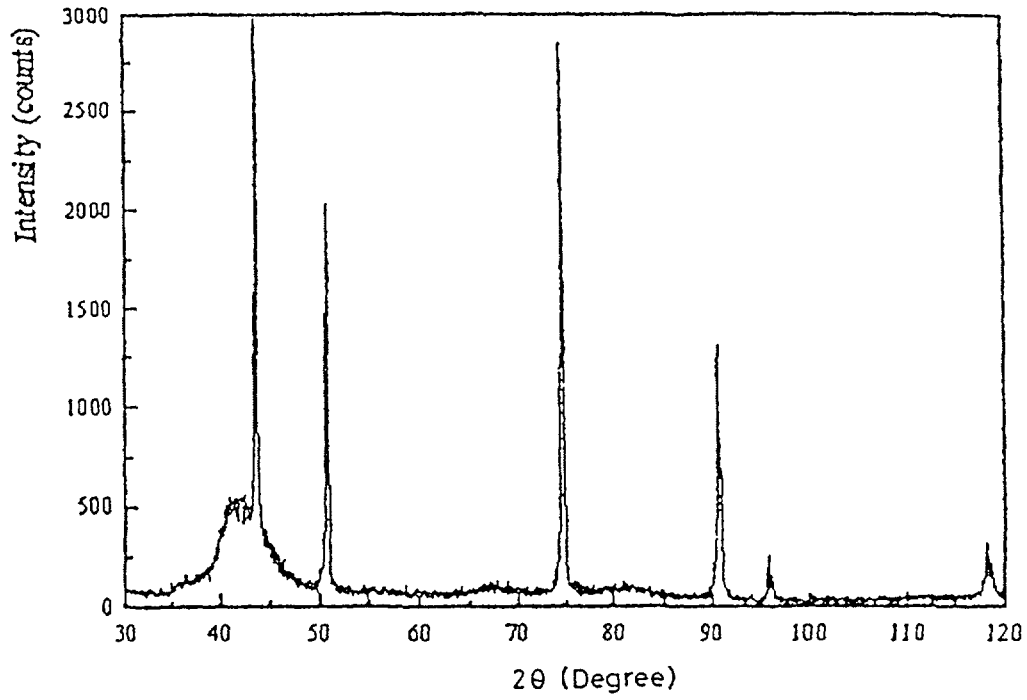


FIG. 68. X ray diffraction of CrN coated SS.

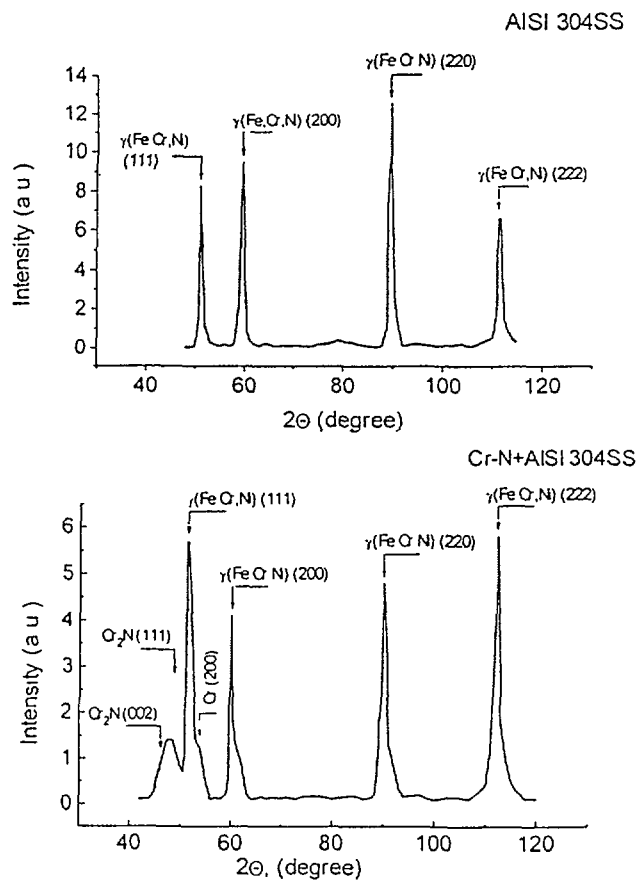


FIG. 69. XRD analysis of AISI 304SS and CrN coated AISI 304SS.

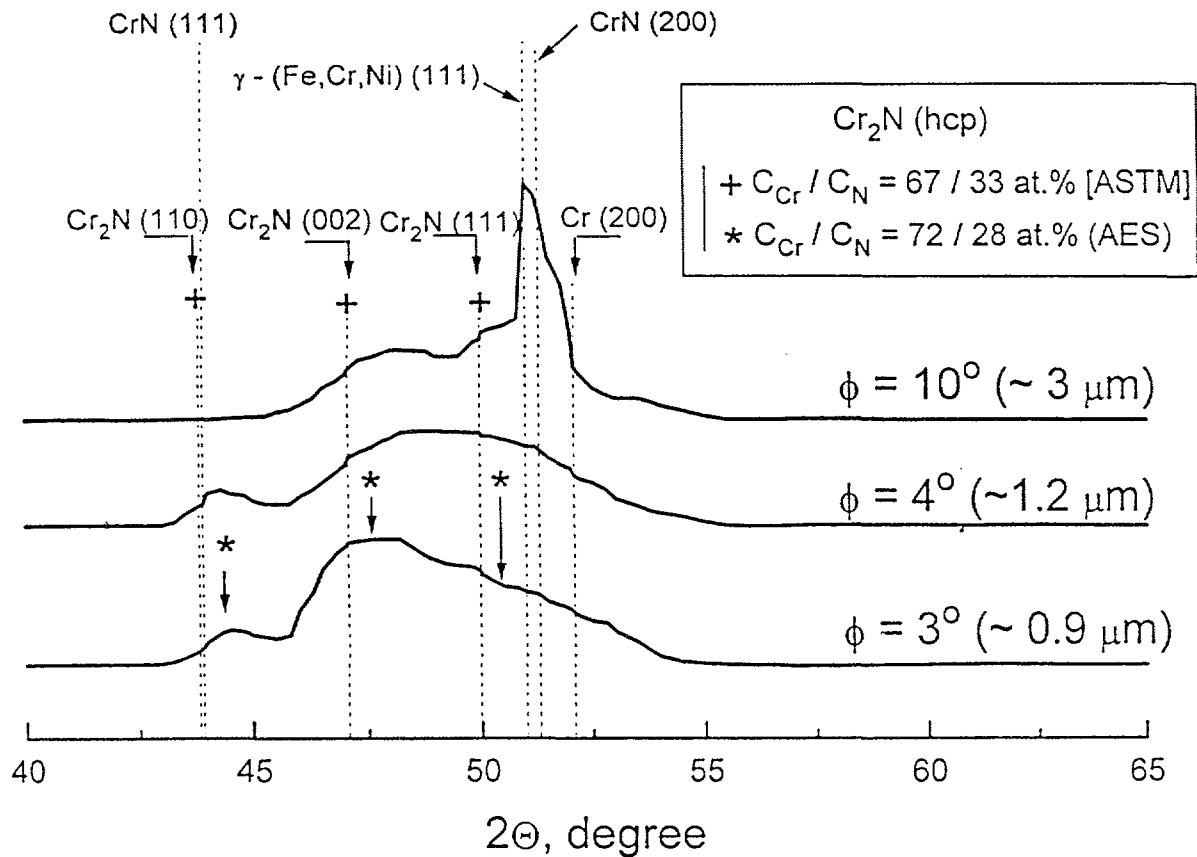


FIG. 70. Glancing X ray analysis of CrN coated SS.

5.1.6. SEM/EDAX/AFM

Surface of chromium nitride coated SS 304 was analysed by scanning electron microscopy. The coating was found uniform and dense (Fig. 71). The composition of the chromium nitride layer as measured by EDAX is given in Table XXIII.

TABLE XXIII. CHEMICAL COMPOSITION OF VARIOUS ELEMENTS PRESENT IN COATING

Element	W.T.%	A.T.%	% S. E.
Fe	5.47	5.11	2.1
Corrosion	94.53	94.89	0.32

The atomic force microscopy (AFM) measurements were performed on a Topo-Metrics TMX 2000 Explorer in ambient conditions. In this equipment the cantilever with the tip scans over the fixed sample by means of piezoelectric drives. AFM provides a topography image and quantitative topography information (Fig. 72). The most frequently used roughness parameter is R_a , which is the arithmetic mean of the deviations in height from the profile mean value. The root mean square (RMS) roughness values based on the power spectral density, which is defined as the square magnitude of the Fourier Transform of the surface profile.

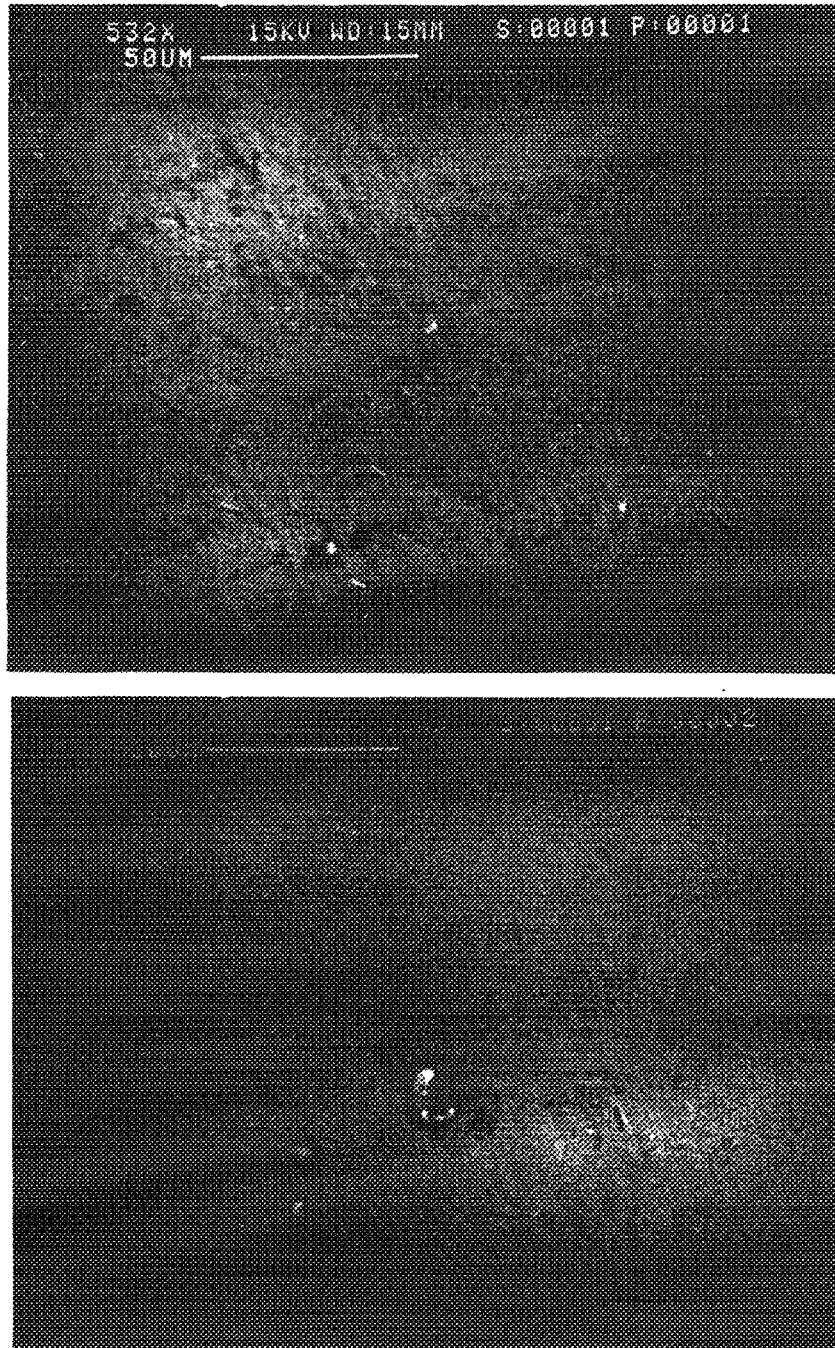


FIG. 71. Scanning Electron Micrographs of CrN coated SS 304.

5.2. PERFORMANCE EVALUATION OF CHROMIUM NITRIDE COATING

5.2.1. Tribological and dynamic micro-indentation test

Tribological and micro-indentation tests were performed on chromium nitride coated SS substrate. The ball-on-disk friction and wear tests were performed in a TRIBOMETER FALEX ISC 320. The general conditions of the test for all the samples were the following:

- Ball material: AISI 52100 steel.
- Ball diameter: 10.0 mm.

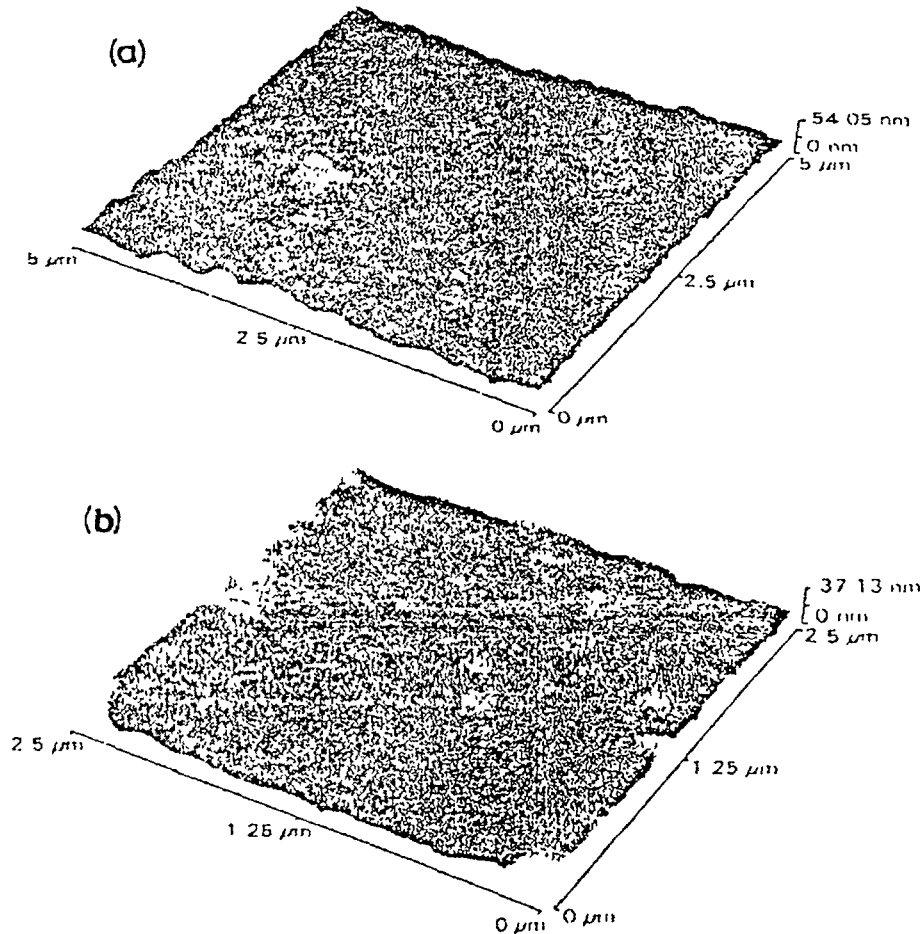


FIG. 72. AFM of polycrystalline CrN coating at two different scan areas: (a) $5 \times 5 \mu\text{m}^2$ and (b) $2.5 \times 2.5 \mu\text{m}^2$.

- Applied load: 100gf.
- Track radius: 9 mm.
- Speed: 53 rpm. linear speed: 5.0 cm/s.
- Temperature: 25°C.
- Relative humidity: 60% lubricant: none.

The friction curves for all chromium nitride samples are presented in Fig. 73, where a dispersion of results can be observed.

Wear tracks were examined by a Optical Profilometry System, and the worn area was calculated for all the samples. The results are indicated in Table XXIV. For comparison purposes a set of coatings, including TINALOX and a Ti-doped DLC coating, both produced by Magnetron Sputtering PVD, were also tested under identical conditions. The results are presented in Fig. 74 and Table XXIII.

Dynamic microindentation tests were carried out with the FISHERSCOPE H100 MICROHARDNESS TEST SYSTEM with load increments until a maximum load of 10 mN was achieved and finally decreasing the load. At each loading and unloading sequence, the vertical displacement (indentation depth) of the indenter into the material is recorded. The results obtained are given in Table XXVI. The loading and unloading curves for both the CrN

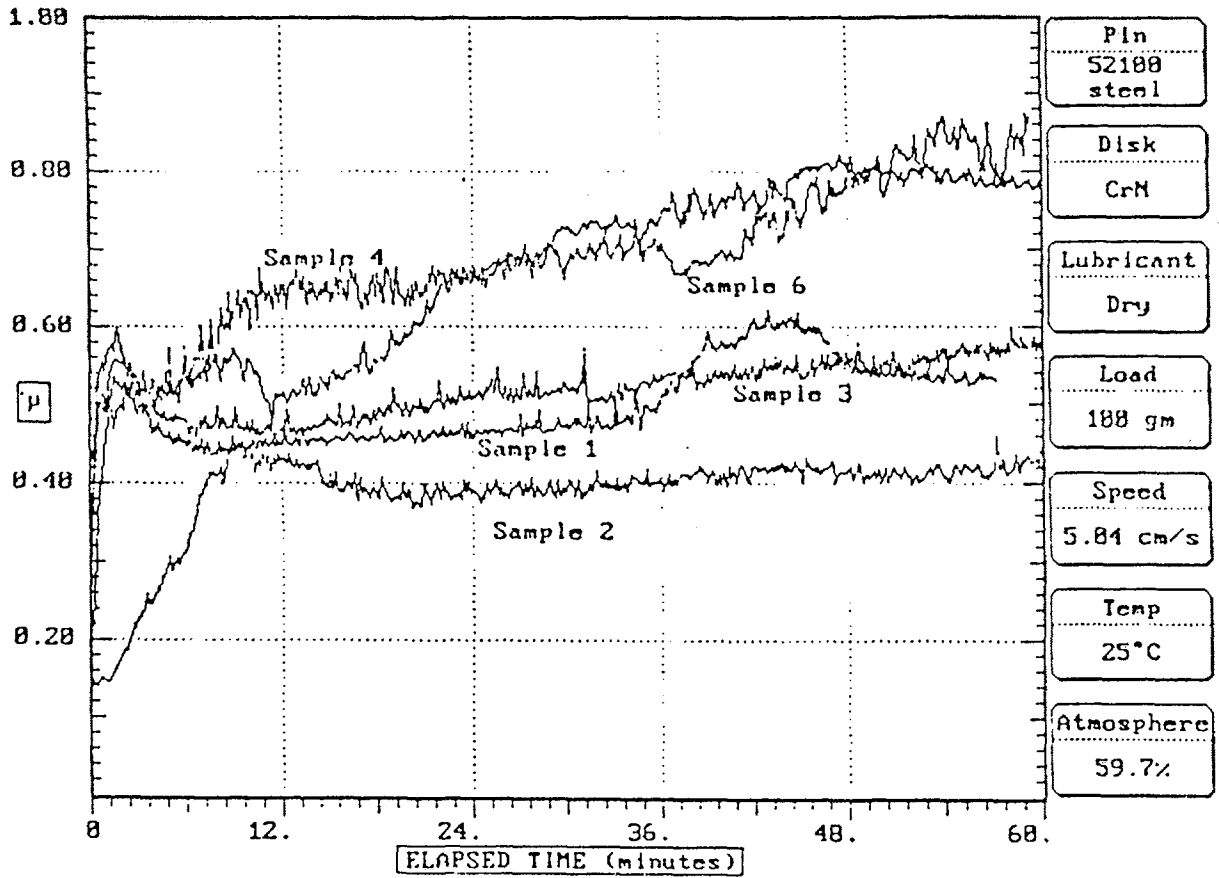


FIG. 73. Friction curves obtained from CrN coated samples.

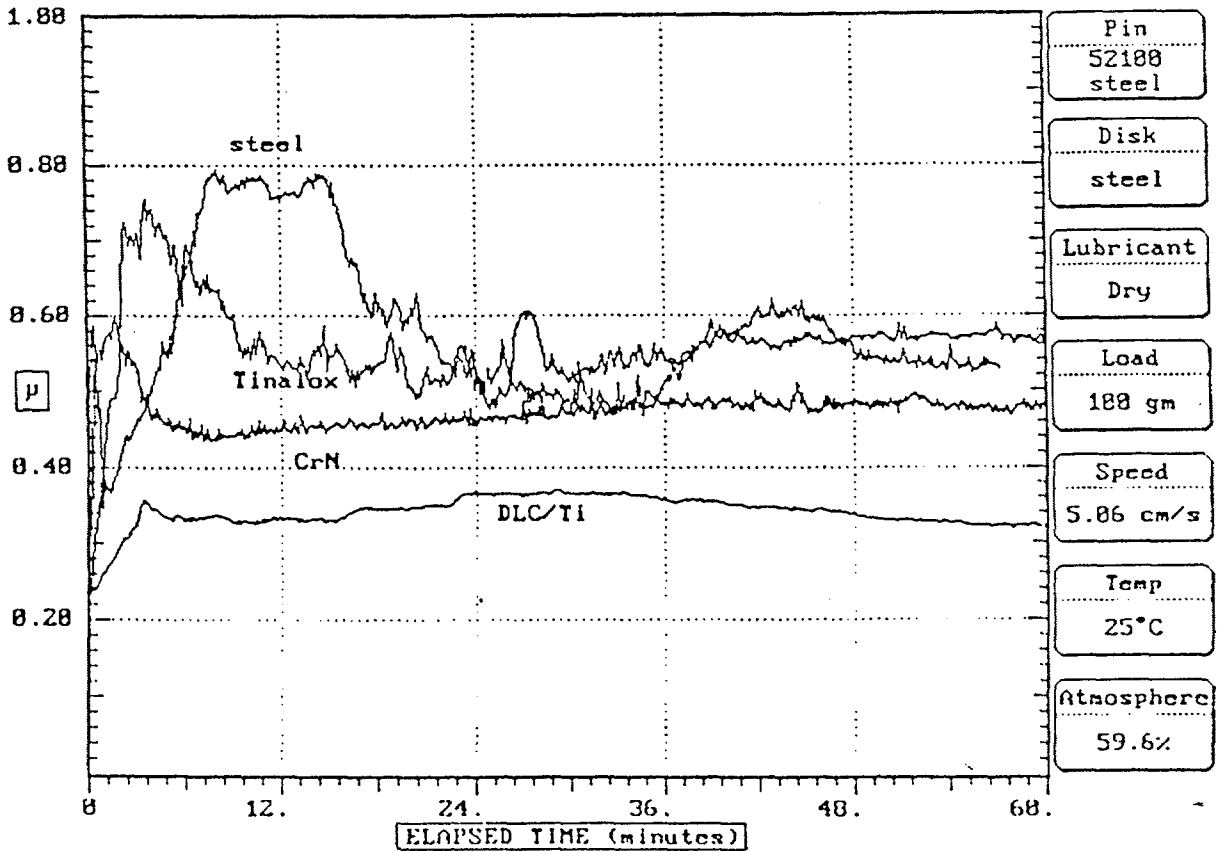


FIG. 74. Friction curves obtained from AISI 52100 steel, CrN (sample 1), TINALOX and Ti-DLC coated samples.

TABLE XXIV. WEAR AREAS OBTAINED BY OPTICAL LASER PROFILOMETRY FROM WORN CrN COATINGS

CrN coatings	Wear tracks area (mm ²)
Sample 1	0.0000225
Sample 2	0.0000225
Sample 3	0.0000500
Sample 4	0.0000500
Sample 5	0.0000525
Sample 6	0.0000525

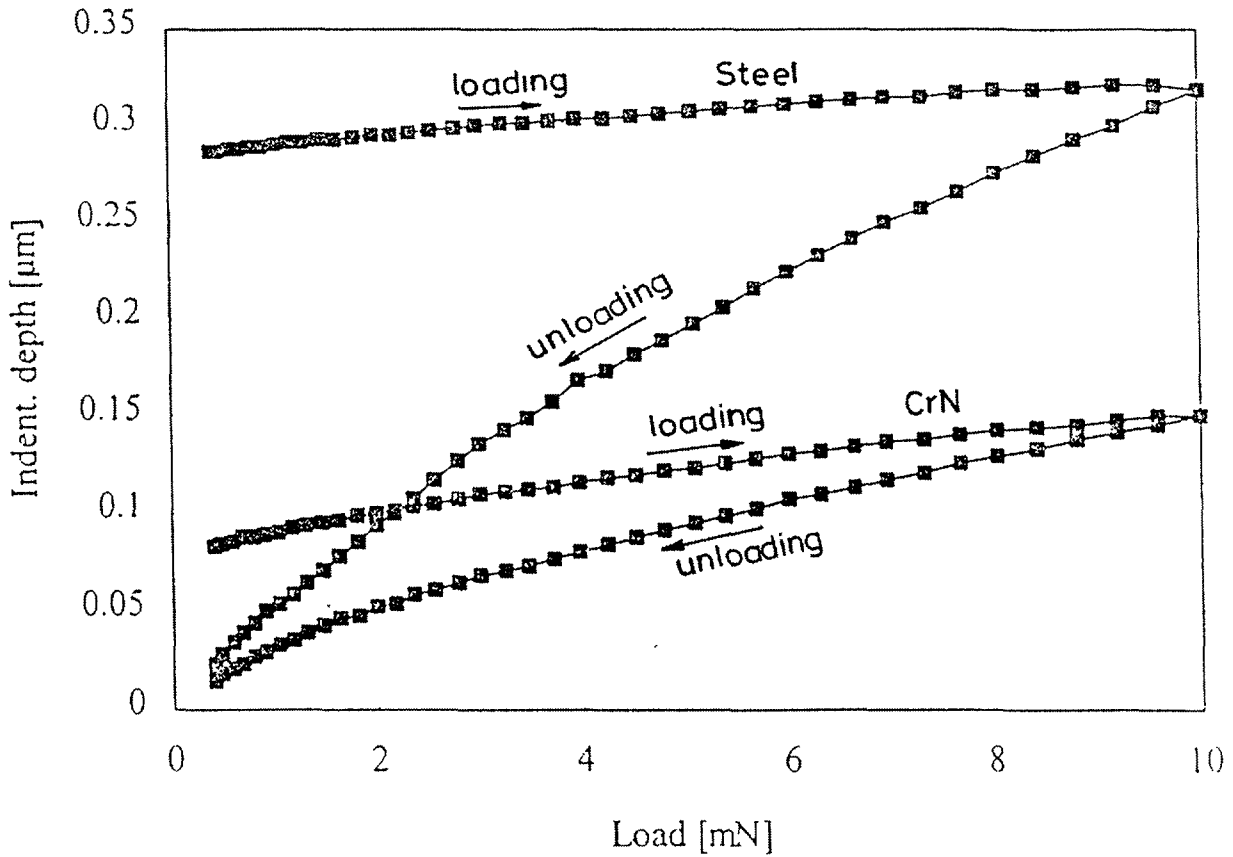
TABLE XXV. WORN AREAS MEASURED BY OPTICAL PROFILOMETRY

Materials/Coatings	Wear track areas (mm ²)
AISI 52100 steel	0.0001025
CrN (sample1)	0.0000225
TINALOX	0.0000475
TI-DLC	0.0000275

coating (lower curves) and the corresponding substrate material (upper curves) are presented in Fig. 75. In this figure it is clearly seen that the elastic recovery and hardness values for the coating are significantly higher than the base material.

TABLE XXVI. DYNAMIC MICRO-INDENTATION RESULTS FOR CrN AND ITS SUBSTRATE MATERIAL

	CrN coating	Steel substrate
Vickers hardness at 10 mN	16749 N/mm ²	3728 N/mm ²
Relative elastic recovery	35.96 %	8.48%
Total work (nj)	0.75	1.51
Elastic work (%)	46.59	10.35
Plastic work (%)	53.41	89.65
Young modulus (GPa)	201	165
Plastic hardness (N/mm ²)	14373 N/mm ²	2549 N/mm ²



Hardness steel= 3728 N/mm²

Hardness CrN=16749 N/mm²

FIG. 75. Loading and unloading curves from substrate and CrN coating after micro-indentation experiments.

5.2.2. Hardness and modulus

The hardness and modulus of the chromium nitride coated sample were measured using an ultra-low load depth sensing force transducer for the Digital Instruments Nanoscope III, developed by Hysitron, Inc. The Hysitron Triboscope has a load resolution of 100 nN and displacement resolution of 0.2 nm. Indentations were made using a Berkovich diamond tip to a maximum load of 2 and 5mN. The loading-unloading behaviour was analysed using the method of Oliver and Pharr. The load displacement curves of the 2mN for three indents are shown in Fig. 76.

	2mN	5mN
Hardness H (GPa)	(18.4 ± 1.2)	(19.6 ± 1.5)
Load Modulus E (GPa)	(234 ± 12)	(198 ± 9.5)

While the hardness is approximately the same for the both loads, the modulus is different. The reason is that the indents made with 5mN are stronger influenced by the substrate. The measured hardness, however, seems to be the real hardness of the film.

5.2.3. Adhesion and scratch test

The scratch test on chromium nitride coated SS 304 substrate was carried out by a scratching tester equipped with a diamond tip and sound sensor. The data are as follows:

Loading rate (kg/min)	Scratching speed (mm/min)	Adhesion ($\times 10^7$ N/m ²)
4	5	120
3	4	130
4	3	125

The adhesion of the deposited layers on AISI 316L steel coated with chromium nitride, was also measured using a scratch test apparatus. Diamond stylus having 120 μm in diameter spherical tip was used as a counter sample. The stylus was mounted on the lever having the stiffness of 45.739 mN/ μm .

The first part of the tests were devoted to the determination of the critical load, i.e. the load causing the layer damage. The speed of translation was set to 0.1 mm/s. The critical force value was determined from the length of the crack from the track beginning up to the place in which the first traces of damage were observed. The tests were done on untreated samples and chromium nitride layers prior and after nitrogen implantations. During the tests performed in increasing load mode tensile type Hertzian cracks were observed for loads exceeding 700 mN. This type of damage suggests that the $\text{CrN}_{0.4}$ layer was not delaminated from the surface of the sample. The final depth of the track equals to several micrometers (typically 3.5–4 μm) (Fig. 77). This value exceeds the total thickness of the deposited layer. Nevertheless, even at the end of the track the chromium nitride layer remains bonded to the substrate. One can thus conclude, that the soft austenitic substrate became contorted, however due to the strong adhesion the chromium nitride layers bends following the substrate deformations. Only slight

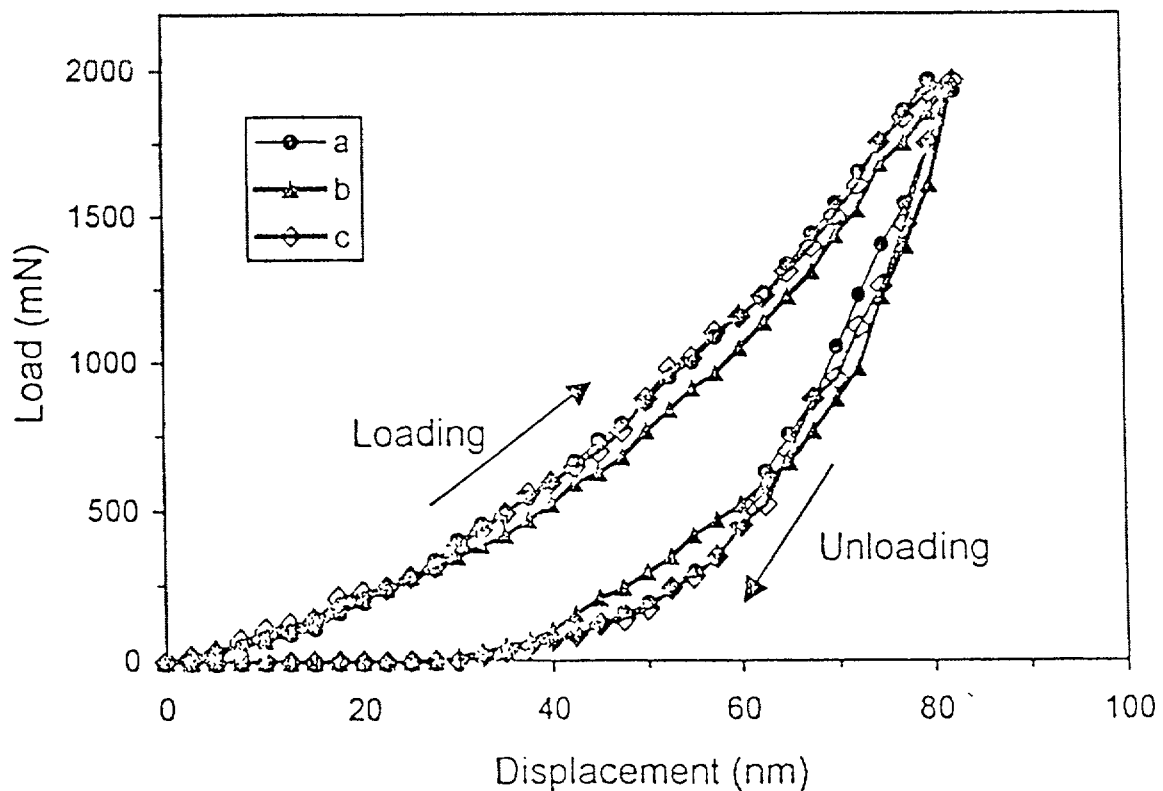


FIG. 76. The loading/unloading curves for three indents made with maximum load of 2 mN.

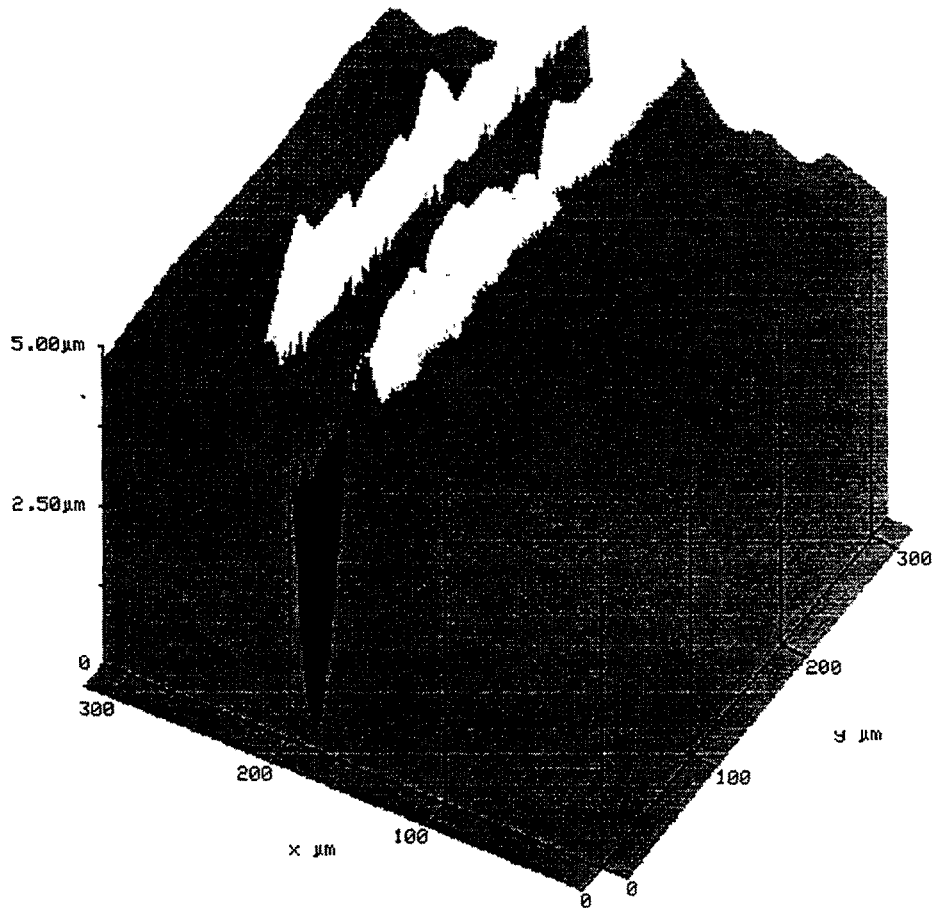


FIG. 77. Surface micro-topography of the end part of scratch track for CrN coated SS.

differences were observed between as deposited and nitrogen ion implanted chromium nitride layers. At the beginning and in the middle the cracks seem to be less numerous and shallower in the case of nitrogen implanted layers. The difference disappears at the end of the cracks.

5.2.4. Impact testing

Results of impact test carried out on chromium nitride coated SS 304 samples using 0.035 J impact energy are given below:

Measuring condition: Impacting energy: 0.035 J for each impacting.

Frequency: $f = 2.5$ times/second

Total impacting numbers: 200

Frequency: $f = 3$ times/second

Total impacting numbers: 3000

After impacting, the chromium nitride coatings of two samples were not broken or peeled off, confirming a good impact resistance of the coating.

5.2.5. Microhardness test

Microhardness test on chromium nitride coated and uncoated SS 304 samples were performed by the MXT- α Digital Microhardness using a load of 5 gm. The result is shown in Table XXVII.

TABLE XXVII. RESULTS OF MICROHARDNESS TEST OF CrN COATED AND UNCOATED 304 SS SAMPLE

Sample surface	av-HK, kg/mm ²	Dev, kg/mm ²	av-HV, kg/mm ²	Dev, kg/mm ²
CrN coated	1013.6	59.8	988.9	74.4
Uncoated	230.9	8.9	213.4	6.6

av-HK: average knoop hardness; av-HV: average vickers hardness; Dev: deviation.

5.2.6. Dry sliding test

Dry sliding test on chromium nitride coated and uncoated AISI 304 steel samples is presented in Fig. 78. In this figure it is clearly seen that the friction coefficient of chromium nitride coating ($\mu = 0.4$) is 1.5 times less than that of AISI 304 steel substrate at the load of 0.7 N.

5.2.7. Friction and wear test

Friction and wear tests were carried out on pin-on-disk wear machine, shown schematically in Fig. 79, as per ASTM standard G 99-90. The apparatus consists of a cylindrical pin (coated/uncoated) which is pressed vertically against a rotating disk. A desired load is applied to the pin while it is sliding. The bottom surface of the pin and the face of the disk together form a wear couple. The experiment is carried out for a particular duration for which a time setter is provided. An LVDT sensor converts the displacement of the pin into an electronic signal which when connected to a computer terminal through a software gives a

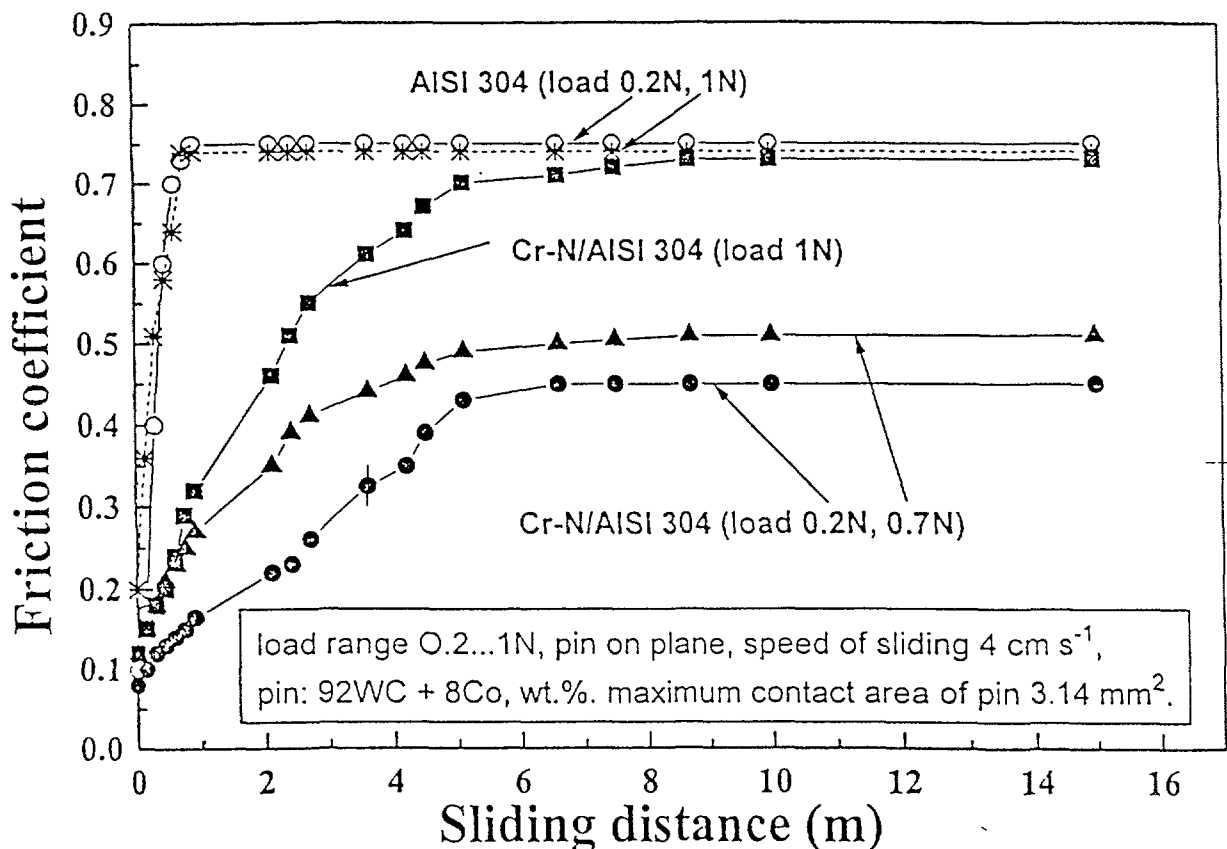


FIG. 78. Dry sliding analysis for CrN coated and uncoated AISI SS304.

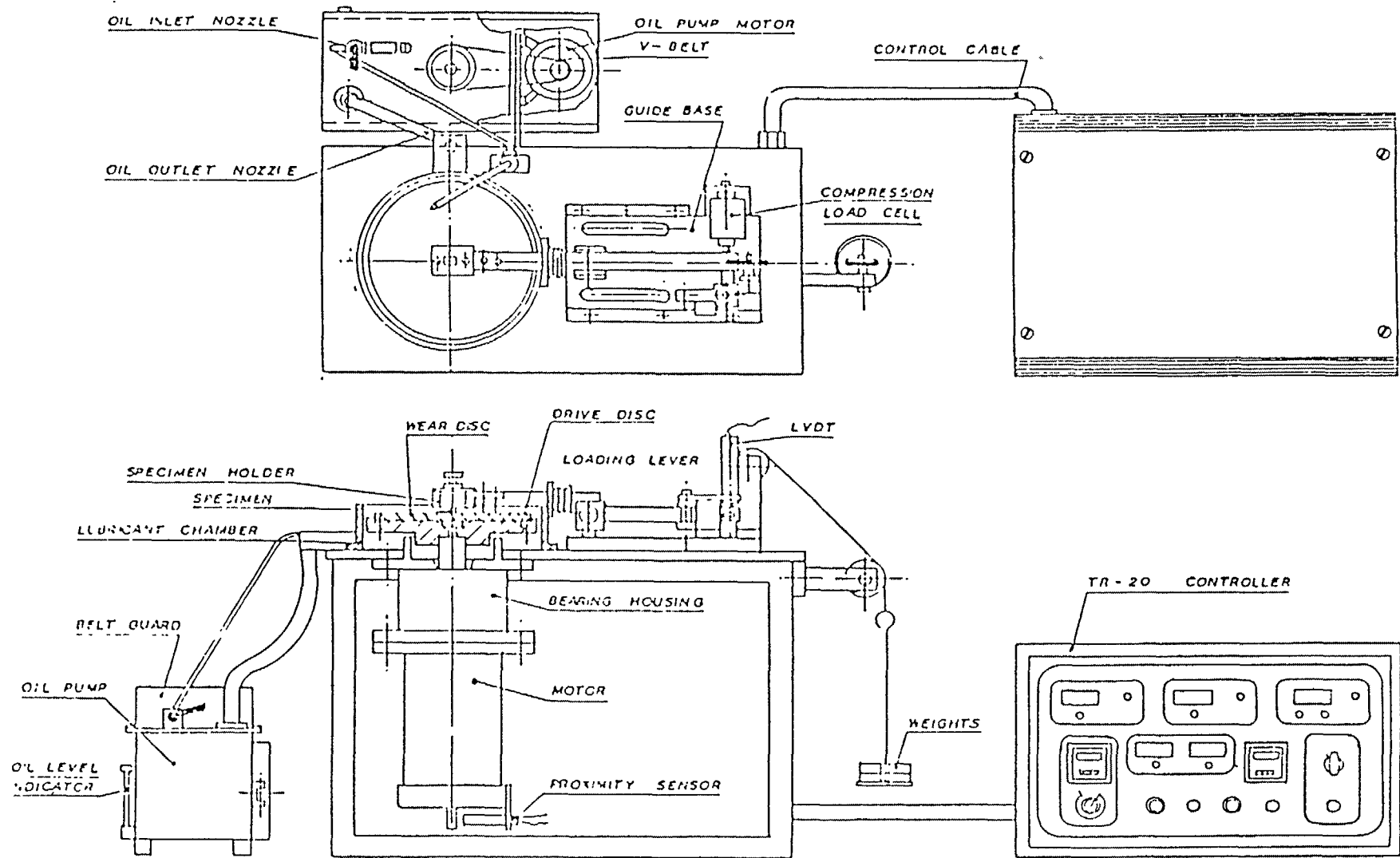


FIG. 79. Schematic of pin-on-disc machine.

graphical plot of a wear vs time. The frictional force can also be obtained through a load cell. The speed of the rotating disk can be varied when desired.

These tests were carried out on pin-on-disk machine, which gives the plot of "displacement in microns vs time in minute" and "frictional force vs time". Wear tests were carried out on En-32 steel disc. The test was carried out at the load of 0.5 kg (5N) for the sliding distance of 250m at the sliding velocity of 0.5 m/s. The plot of displacement vs time are shown in Fig. 80 and Fig. 81 for a load of 0.5 and 1.5 kg respectively. Initially some scatter in the data was observed but later on the overall trends were found to be uniform. The slope of displacement vs time gives the wear rate of the coatings in microns per minute. From the plot of frictional force vs time, coefficient of friction can be calculated as given in Table XXVIII.

TABLE XXVIII. WEAR RATE AND COEFFICIENT OF FRICTION FOR SS AND CrN COATED SS

	Stainless Steel	CrN coated SS
Coefficient of friction	0.54	0.47
Wear rate	2.24	1.75

Wear and friction tests were also carried out on nitrogen implanted chromium nitride coated samples. The as-deposited chromium nitride layers were nitrogen implanted up to dose of $5 \times 10^{16} \text{ N}_2^+/\text{cm}^2$, $1 \times 10^{17} \text{ N}_2^+/\text{cm}^2$, $2 \times 10^{17} \text{ N}_2^+/\text{cm}^2$ by 100 KeV molecular nitrogen ion (N_2^+) beam. The wear and friction test of nitrogen implanted samples were studied using a ball-on-flat tribotester. The 6.5 mm balls were used as a counter sample. The test was carried at a load of 5N Hz in air up to 300 oscillations. The friction coefficient values were equal to 0.76 to 0.8 for as-deposited, low and medium dose nitrogen implanted samples. For the highest nitrogen dose, the friction coefficient value dropped down to 0.54.

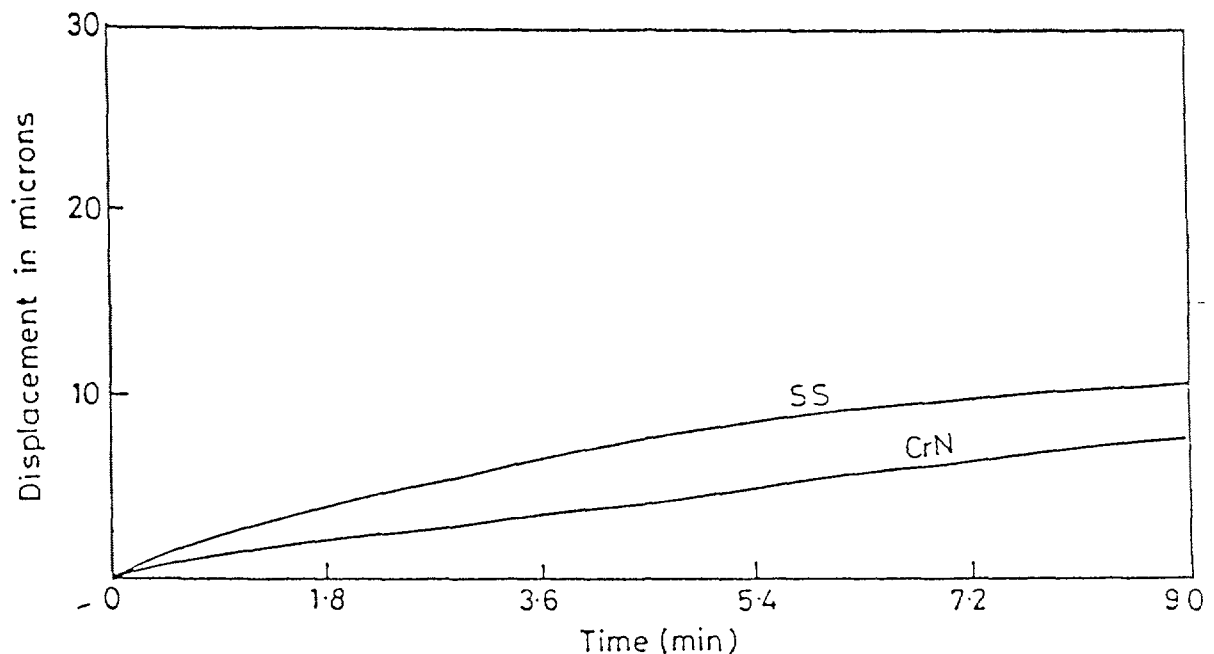


FIG. 80. Wear trend for SS and CrN coating (load = 0.5 kg, $v = 0.5 \text{ m/s}$, sliding distance = 250 m).

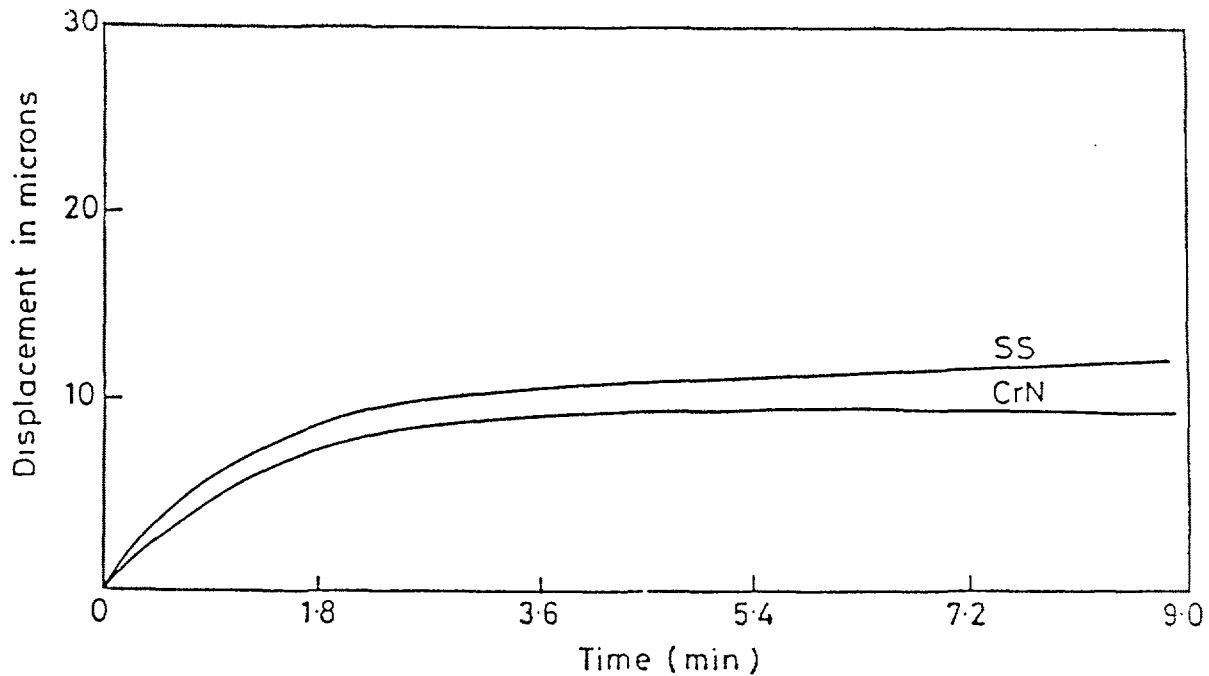


FIG. 81. Wear trend for SS and CrN coating (load = 1.5 kg, $v = 0.5$ m/s, sliding distance = 250 m).

The wear extent was determined by using a 3-D Tayler-Hobson Profilometer. The typical surface reliefs obtained for as-deposited and high dose nitrogen implanted samples are shown in Fig. 82. It is interesting to note that striking reduction of wear was observed after nitrogen implantation. Taking into account, that the depth of the modification (~1 micrometer) exceeds significantly the projected range of the implanted ions (~0.1 micrometer) this effect can very likely be attributed to the changes in stress level in CrN layer. Such observation points to an interesting application of ion implantation; the process can be used not for the modification of the composition of surface layer, but to tailor the stress in deposited layers.

5.2.8. Corrosion test

Corrosion tests were carried for the base SS 304 and chromium nitride coated SS samples by Potentiodynamic scan in 1N-H₂SO₄ solution at the same scan rate of -0.2V to 1V, 1mV/s, 1s/pt. The experimental set-up is shown in Fig. 83. The anodic polarization curves are given in Fig. 84a and b. From these figures following inference can be obtained about the corrosion behaviour of the coated and uncoated specimens (Table XXIX).

TABLE XXIX. RESULTS OF ANODIC POLARIZATION TESTS OF SS 304 AND CrN SS 304 IN 1N H₂SO₄ ON SS SPECIMEN

Sample	E_{ocp} (V)	Area (cm ²)	E_{corr} (mV)	I_{corr} (A/cm ²)	Corr. Rate (mpy)
SS 304	-0.527	1	508.4	3.51×10^{-4}	4.084
CrN coated	0.245	0.42	150.1	1.0×10^{-7}	0.001

It is clear that E_{corr} and I_{corr} values are much lower for chromium nitride coated stainless steel specimen. These analyses confirm that chromium nitride coated SS shows lower corrosion rate than the base SS 304.

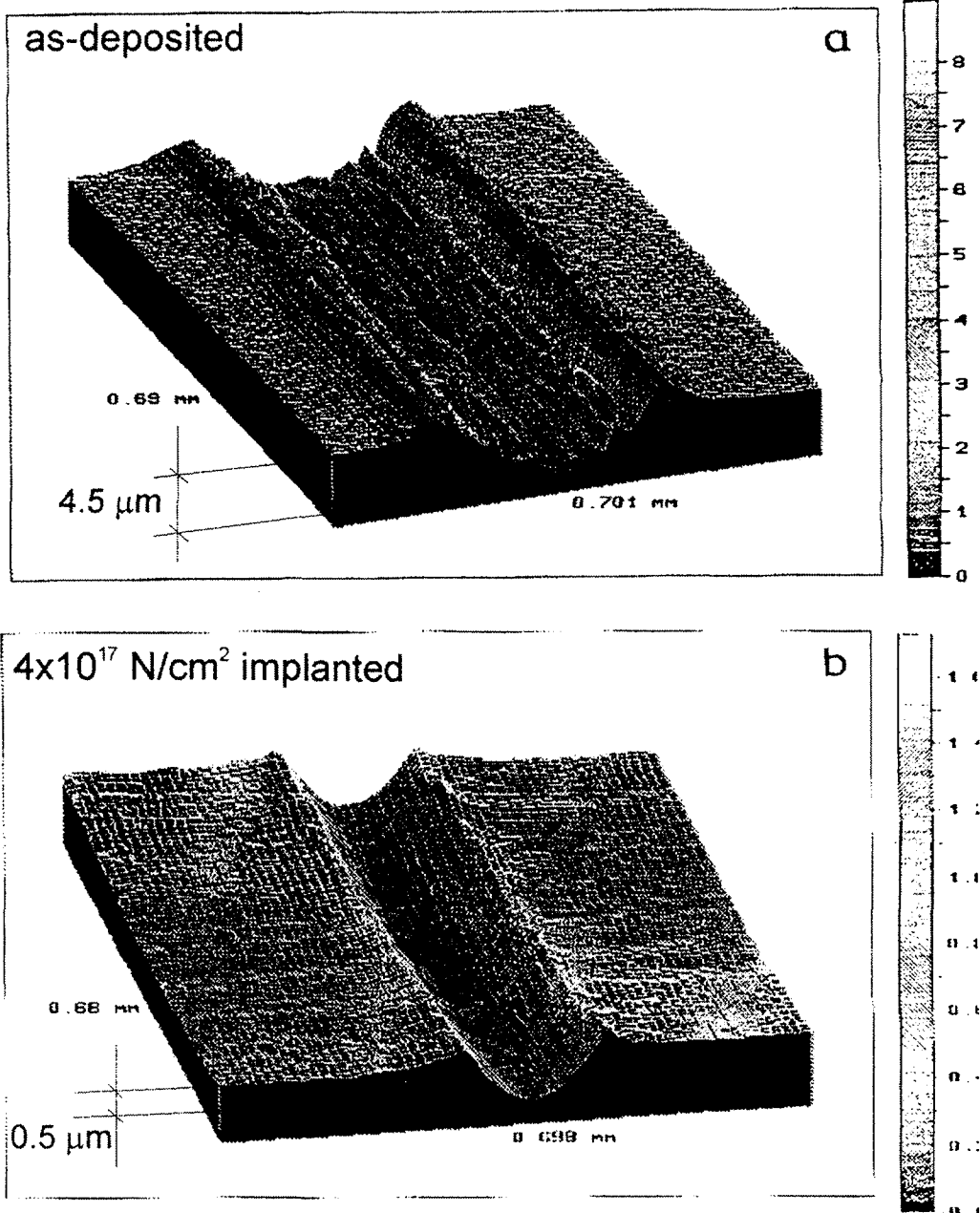


FIG. 82. Surface profiles using 3-D Taylor-Hobson profilometer for (a) as-deposited (b) nitrogen implanted chromium nitride coated stainless steel.

5.2.9. Discussion

Scanning electron micrographs of chromium nitride coated stainless steel substrate showed that the chromium nitride coating is uniform and dense. The thickness of the chromium nitride coating on SS specimens was calculated to be $1.3 \mu\text{m}$ by RBS method, which was also confirmed by Glancing X ray method.

The XPS analysis of the chromium nitride coating on stainless steel sample showed that the chromium nitride coating was composed of mostly Cr_2N , and potentially CrN in an elemental Cr matrix, and small quantities chromium carbide and oxide. The overall ratio of Cr

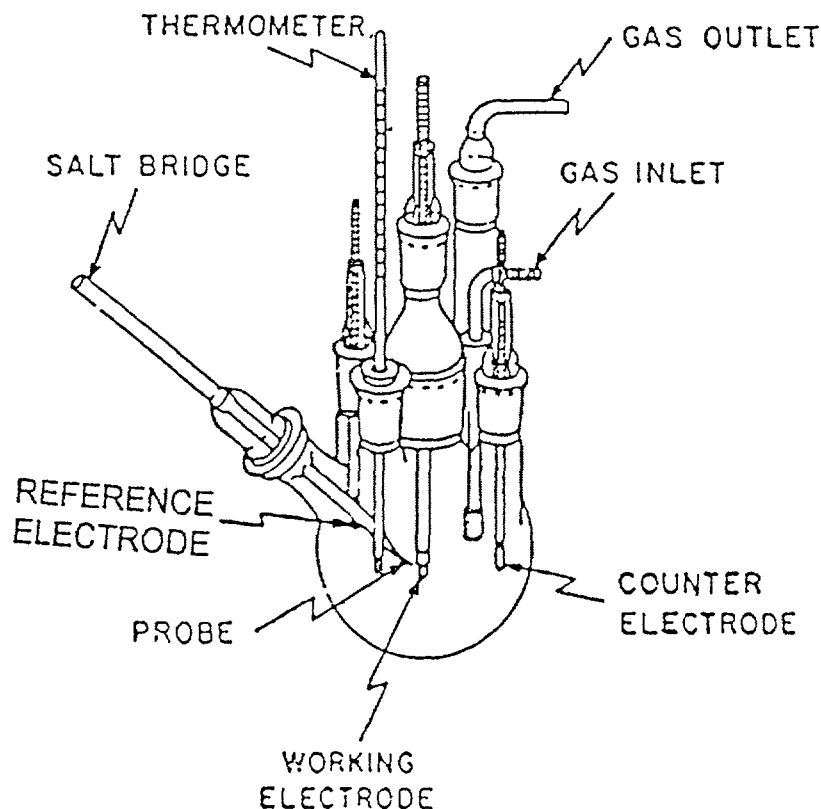


FIG. 83. Experimental set-up of Anodic Polarisation.

to N was $75 \pm 5\%$ Cr to $25 \pm 5\%$ N. This result was further confirmed by AES depth profile of the coating, which showed the presence of chromium nitride in the entire coating depth. Both XPS and AES results showed that the chromium nitride coating is a complicated mixture of CrN, Cr₂N, and chromium oxide. The AES and XPS sputter depth profile have further shown that the average atomic composition was close to Cr_{0.80}N_{0.20} (also confirmed by RBS method) in the sub-surface region; and close to Cr_{0.73}N_{0.27} near the substrate/coating interface. The coating also contained small quantities of carbide and oxide. The roughness parameters of the coated specimens measured with the AFM method are: $R_a = 5.91$ nm and $RMS = 7.53$ nm, the same as the substrate samples. Thus, the coating uniformly covers the substrate. The chromium nitride coating consists mainly of Cr₂N phase as confirmed by glancing XRD analysis, with grain size of 5 ± 2 μ m. The low grain size is a result of low temperature coating deposition process which characterizes the IBAD process.

Stainless steel specimens coated with chromium nitride were also subjected to various performance tests. Several mechanical tests were carried out on chromium nitride coated and uncoated AISI 304 steel sample. Chromium nitride coatings are not known for low friction; however, dry sliding wear test showed that the friction coefficient of stainless steel improves by 1.5 times by chromium nitride coating. Other tests such as hardness, scratch and impact measurement also showed significant improvement on tribological properties. The adhesion of the coating to the substrate proved to be excellent as tested in various, indent and scratch tests. This is another characteristic of IBAD coatings.

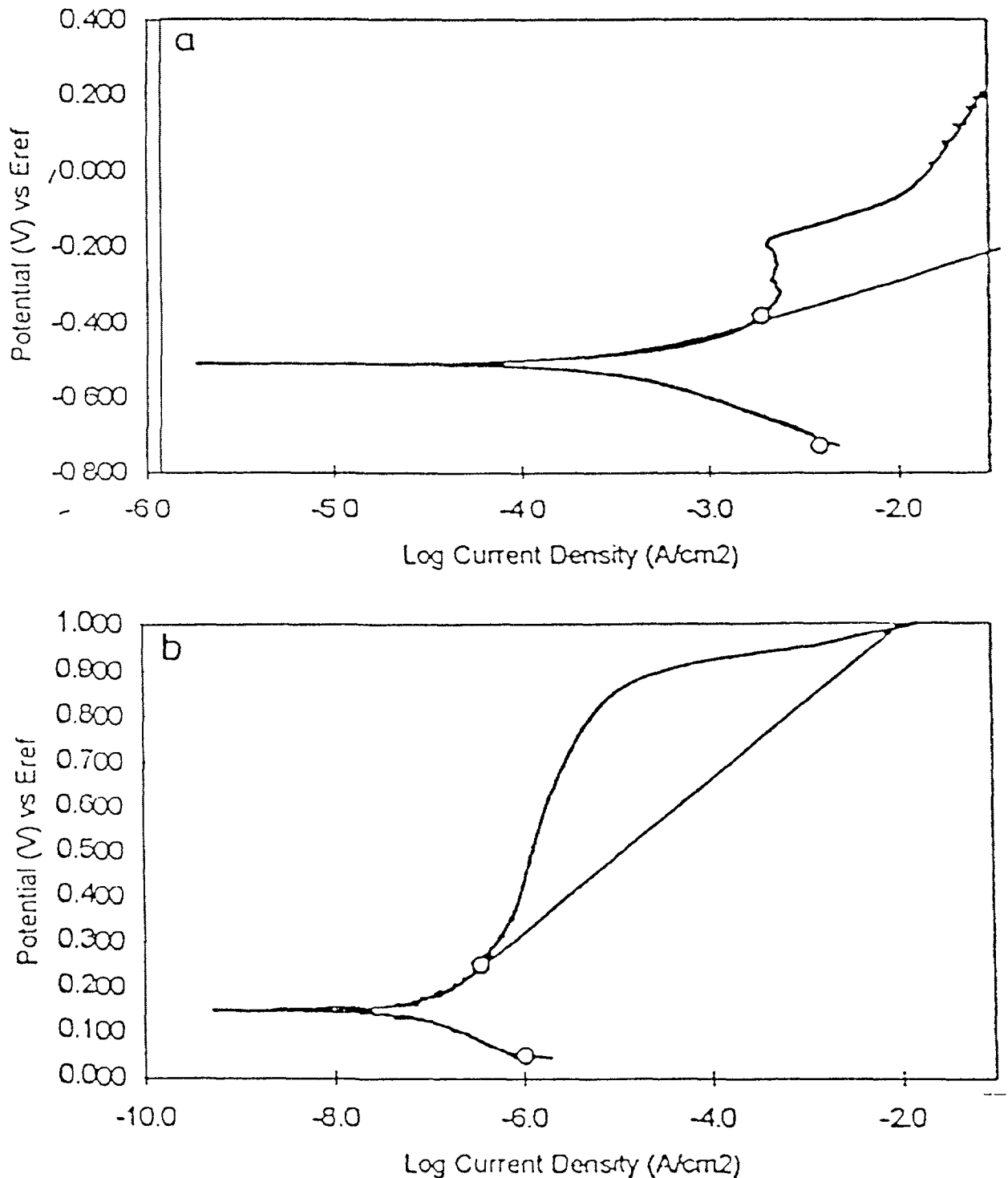


FIG. 84. Anodic Polarisation curve of (a) SS 304 (b) CrN coated SS.

6. COST ANALYSIS FOR ION BEAM MODIFICATION PROCESSES

The capital equipment cost for ion implantation system varies depending on specifications. Mass analyzed ion implanters are significantly more expensive but provide the opportunity to work with a pure elemental species and furthermore with a specific isotope of the element. Non-mass-analyzed ion implanters are less expensive and yet quite useful for ion implantation of gaseous species.

Combining ion implantation technology with a coating process adds significantly to the capital equipment cost but also considerably adds to the performance capability of the system.

A typical cost of ion beam treatment (with the associated equipment requirements such as transformers, chillers, air conditioning, etc.) system is about US\$ 500 000. Pre-owned ion implanters (from semiconductor manufacturers) can be obtained at a substantially lower cost. (US\$ 100 000). New ion implantation systems are considerably more costly (US\$ 2 000 000). Unit cost for the ion beam processing of samples is a variable depending on local labour, utility and amortization costs for the equipment. According to recent estimates this cost can vary between US\$ 0.1 to 1.0 per cm² for most typical components processed.

According to the Thai experience the capital cost to set up ion beam based laboratory in developing country is:

150 kV mass ion implanter (research type, second hand)	US\$150 000
Sample preparation equipment (polishing machine, profilometer) and test equipment (wear, microhardness)	US\$ 50 000
250 m ² laboratory with cooling water and air conditioned small housing	US\$100 000
Total:	US\$300 000

The characterization equipment such as a small tandem accelerator, AES, SEM, XRD to study depth profiling and surface micrography should be carried in other collaborating laboratory. These characterization facilities cost as much as the capital of the whole ion beam laboratory.

7. CONCLUSIONS

- (a) Reliability and reproduction of ion beam technologies make them highly desirable for material modification in many industrial applications.
- (b) The CRP was able to evaluate alternative ion beam based coating techniques to coat relatively thicker coatings and achieve improvement in tribological and chemical properties of the surfaces.
- (c) The main contribution of ion beam techniques is to improve the adhesion of coating to the substrate. Additional advantage of ion beams is to control the stress in the coated films.
- (d) Nitrided coatings achieved by IBAD process (in the range of 1 μm) improved considerably wear, friction, hardness, corrosion and oxidation of stainless steel.
- (e) CrN coating by plasma arc process, plasma nitriding and Al deposition by ion beam mixing process on Ti-Al intermetallics enhanced their high temperature oxidation resistance.
- (f) Zr and C deposition by arc vapour deposition improved significantly the hardness and resistance of high speed steels. Also, pre-implantation of Ar followed by TiN coatings deposition on steel by arc vapor further enhanced the adhesion of the improved friction properties.
- (g) W coatings made by ion beam mixing techniques improved the wear and friction of high speed steel by a factor of four.
- (h) Performance of bio-medical implants has been improved by ion beam treatment of light ions such as N and C ions.

- (i) Ion implantation applied as a post treatment to IBAD coatings and hard Cr plating further improve tribological properties significantly.
- (j) Metallic ion implantation (Mo, Y) on Si_3N_4 and ZrO_2 ceramics by MEVVA enhanced the conductivity and mechanical properties.
- (k) The interlaboratory test carried out by all the participants of CRP, characterized and evaluated the performance of CrN coatings on stainless steel samples. The high-quality contribution from each laboratory enhanced the understanding of the properties of the coating. Coatings like the one evaluated have provided significant potential to improve friction, wear and corrosion of industrial component.

8. RECOMMENDATIONS

- The CRP recognizes the importance of the ion beam based processes as a means for evaluation of surface related properties such as friction, wear, corrosion. This technology offers an excellent opportunity for infrastructure development, training and mutual collaboration among various groups, disciplines and laboratories for further advancement in the understanding of surface related phenomena. The CRP believes that for the immediate future these technologies need to be further developed in research and educational institutions in collaboration with relevant industries.
- For developing countries with manufacturing industries, an ion beam based technique should be established step by step in order to enhance infrastructure development and finally finding its own niche market. The establishment of the ion beam laboratory could be accomplished in consulting with the Agency through expert groups.
- For specific niche market, judicious choice should be made for the implementation of the available technologies for a specific industrial application.
- The CRP believes an extension of these technologies to the surface treatment of polymers deserves special attention as addition of surface related technologies allows property changes that were not available as conventional technologies such as:
 - surface cleanliness to improve adherence,
 - electrical properties,
 - surface energy,
 - surface chemistry and structure,
 - mechanical properties,
 - gas permeability.
- These technologies offer significant improvement in surface properties of polymers used in medical application. These property evaluation needs further studies through a well focussed CRP.

REFERENCES

- [1] MARKWITZ, A., et al., Investigation of ultra thin silicon nitride layers produced by low-energy ion implantation and EB-RTA, Nucl. Instrum. Methods in Phys. Res., Section B, Beam Interactions with Materials and Atoms **89** 1-4 (1994) 362–368.
- [2] KETZER, C.S., et al., Synthesis of iron silicides starting with Fe/Si multilayers, Hyperfine Interactions **83** 1–4 (1994) 321–325.
- [3] LATUSZYNSKI, A., MACZKA, D., Application of radioactive ion beams in the study of implanted layers, Nucl. Instrum. Methods in Phys. Res., Section B, Beam Interactions with Materials and Atoms (1994) **85** (1–4) 798–802.
- [4] ZHANG, T., et al., A study of pulsed high flux Ti, Mo, V, and Y ion implantation for surface modification of resistances in wear, corrosion and oxidation, Vacuum **45** 9 (1994) 945–950.
- [5] SVORCIK, V., et al., Modification of polyethyleneterephthalate by implantation of nitrogen ions, J. Electrochem. Soc. **141** 2 (1994) 582–584.
- [6] ITOH, M., et al., Transport properties of modulation-doped grown by molecular beam epitaxy after focused ion beam implantation, Japan. J. Applied Phys., Part 1, Regular Papers and Short Notes **33** 1B (1994) 771–774.
- [7] POULSEN, J.R., et al., Diffusion of nanaosized sodium inclusions in platinum, J. Phys. Condensed Matter **6** 28 (1994) 5397–5408.
- [8] POULSEN, J.R., et al., Diffusion of nanaosized sodium inclusions in platinum, J. Phys., Condensed Matter **6** 28 (1994) 5397–5408.
- [9] ZHANG, J., et al., Ion beam mixing of Ti/Mo bilayers and multilayers, Atom. Energy Science and Technol. **27** 6 (1993) 481–487.
- [10] CHEN, M., et al., Ion beam applications on a 100 keV EMIS and ion implanter, Trends Nucl. Phys. **10** 4 (1993) 39–42.
- [11] SAKAMOTO, K., Modification of polymers with carbon-carbon chain by ion implantation, IONICS **20** 3 (1994) 19–26.
- [12] SUZUKI, Y., et al., Ion implantation into polymeric materials for biomedical application, IONICS **20** 3 (1994) 35–42.
- [13] SUGIZAKI, Y., et al., Effect of ion beam modification on hydrogen absorption by metals, Surface and Coatings Technol. **65** 1–3 (1994) 40–44.
- [14] LI, H., JI, C., Surface modification of non-semiconductors by ion beams in China, Surface and Coatings Technol. **65** 1–3 (1994) 189–193.
- [15] CHEN, J., QIU, H., SHU, C., A 100 keV ion implantation and mixing machine for metal surface modification, Nuclear Techniques **17** 1 (1994) 37–41.
- [16] RIVIERE, J.P., Surface treatments using ion beams, Materials Science Forum **163–165** 2 (1994) 431–448.
- [17] NISHIMURA, O., et al., Surface structure of nitrogen ion implanted 304 stainless steel, Surface and Coatings Technol. **66** 1–3 (1994) 403–407.
- [18] ZHANG, Q.Y., et al., Investigation of TaN films implanted with nitrogen and argon ions, Surface and Coatings Technol. **66** 1–3 (1994) 468–471.
- [19] LIU, L.J., et al., Modification of tribological properties of commercial TiN coatings by carbon ion implantation, Surface and Coatings Technol. **71** 2 (1995) 159–166.
- [20] ZHANG, H., et al., Metal ion implantation with three beams, Surface and Coatings Technol. **66** 1–3 (1994) 345–349.
- [21] MULLER, H.R., ENSINGER, W., FRECH, G., WOLF, G.K., A new approach to ion beam modification of powders (Au/Al₂O₃), Nuclear Instrum. and Meth. Phys. Res., Section B, Beam Interactions with Materials and Atoms **89** 1–4 (1994) 357–361.

- [22] EVANS, P.J., et al., Surface modification of austenitic stainless steel by titanium ion implantation, *Surface and Coatings Technol.* **71** 1-3 (1995) 151–158.
- [23] BRUEHL, S., et al., Generation of residual deformations by pulsed ion implantation, *J. Phys., D, Applied Physics* **28** 8 (1995) 1655–1660.
- [24] SIMSON, S., HEIDE, N., SCHULTZ, J.W., Surface analytical investigations of Al and (Ti, Al) nitrides formed by ion implantation and their corrosion properties, *Surface and Interface Anal.* **22** 1–12 (1994) 431–435.
- [25] WOOD, B.P., et al., Initial operation of a large scale plasma source ion implantation experiment, *J. Vacuum Science and Technol. B, Microelectronics* **12** 2 (1994) 870–874.
- [26] AGGARWAL, S., et al., Surface characterization of nitrogen ion implanted etched and polished AISI 316 stainless steel, *Thin Solid Films* **237** 1–2 (1994) 175–180.
- [27] LIEB, K.P., BOLSE, W., UHRMACHER, M., Ion beam mixing in metal/metal and nitride/metal layers-new perspectives, *Nuclear Instrum. Methods Phys. Res. Section B, Beam Interactions with Materials and Atoms* **89** 1–4 (1994) 277–289.
- [28] HUANG, C.-T., DUH, J.-G., Nitrogen implantation of Ti and Ti+Al films deposited on tool steel, *Vacuum Nucl. Instrum. Methods Phys. Res., Section B, Beam Interactions with Materials and Atoms* **89** 1–4 (1994) 369–372.
- [29] JIMENEZ-MORALES, A., et al., Electrochemical study of the corrosion behaviour of copper surface modified by nitrogen ion implantation, *J. Appl. Electrochem.*, **27** 5 (1997) 550–557.
- [30] CHOI, B.H., et al., The characteristics of surface oxidation and corrosion resistance of nitrogen implanted zircaloy-4, *Surface and Coatings Technol.* **89** 3 (1997) 252–257.
- [31] WANG, X., et al., A study of corrosion resistance behaviour of W+C dual ion implanted H13 steel, *Nuclear Techniques* **20** 3 (1997) 138–142.
- [32] RAO, Z., SOOD, D.K., WILLIAMS, J.S., O'CONNOR, B.H., Wear behaviour of carbon implanted hard chromium coatings, *Surface Engineering* **13** 1 (1997) 61–65.
- [33] ENDRST, R., SVORCIK, V., RYBKA, V., Surface modification of polymers induced by ion implantation, *Radiation Effects and Defects in Solids* **137** 1–4 (1995) 25–28.
- [34] WANG, G., HA, H., Surface modification of biomaterials with ion implantation in polymer, *J. Isotopes* **9** 1–4 (1996) 189–192.
- [35] HAMPIKIN, J.M., SAQIB, M., POTTER, D.I., Improved oxidation resistance of group VB refractory metals by Al³⁺ ion implantation, *Metallurgical Transactions, B, Process Metallurgy* **27** 3 (1996) 491–500.
- [36] BAI, X.D., ZHU, D.H., LIU, B.X., Anodic and air oxidation of niobium studied by ion beam analysis with implanted Xe marker, *Nuclear Instrum. Methods Phys. Res. Section B, Beam Interactions with Materials and Atoms* **114** 1–2 (1996) 64–69.
- [37] WANG, B., A comparative test for wear resistance of N⁺ ion implanted piston rings, *Nuclear Techniques* **19** 4 (1996) 208–210.
- [38] KNIGHT, S.T., SAMANDI, M., EVANS, P.J., Titanium aluminide formation by ion implantation, *J. Mater. Science Lett.* **15** 5 (1996) 414–415.
- [39] WANG, Q., YANG, X., WANG, Z., Surface modification of alumina by nitrogen ion implantation, *Nuclear Techniques* **19** 2 (1996) 75–79.
- [40] BOUDOUKHA, L., et al., Mechanical characterization by nanoindentation of zirconium ion implanted alumina, *Nuclear Instrum. Methods Phys. Res., Section B, Beam Interactions with Materials and Atoms* **108** 1–2 (1996) 87–93.
- [41] SHRIVASTAVA, S., et al., Hardening of steel by boron steel ion implantation — dependence on phase composition, *Vacuum* **47** 3 (1996) 247–249.
- [42] MITSUO, A., et al., Improvement of thermal oxidation property of thermocouple by Al-ion implantation, *IONICS* **21** 6 (1995) 57–62.

- [43] KOTHARI, D.C., PRATAP, R., Tribological applications of ion implantation, Transactions of the Metal Finishers' Association of India **4** 91 (1995) 67–75.
- [44] RUECK, M., DOROTHEE, Experience with the MEVVA source for implanting metals for improved wear, Surface and Coatings Technol. **65** 1–3 (1994) 121–127.
- [45] ANDERS, A., et al., Metal plasma immersion ion implantation and deposition using vacuum arc plasma sources, J. Vacuum Science and Technol., B. Microelectronics Processing and Phenomena **12** 2 (1994) 815–820.
- [46] TUSZEWSKI, M., et al., Plasma immersion ion implantation for semiconductor thin film growth, J. Vacuum Science and Technol., B. Microelectronics Processing and Phenomena **12** 2 (1994) 973–976.
- [47] KOMVOPOULOS, et al., Surface modification of magnetic heads by plasma immersion ion implantation and deposition, J. Appl. **76** 3 (1994) 1656–1664.
- [48] DEB, D., SIAMBIS, J., SYMONS, R., Plasma ion implantation technology for broad industrial application, J. Vacuum Science Technol., B, Microelectronics Processing and Phenomena **12** 2 (1994) 828–832.
- [49] ANDERS, A., et. al., Increasing the retained dose by plasma immersion ion implantation and deposition, Nucl. Instrum. Methods in Phys. Res **102** 1–4 (1995), 132–135.
- [50] ZENG, X., TANG, B., CHU, P.K., Improving the plasma immersion ion implantation impact energy inside a cylindrical bore by using an auxiliary electrode, Appl. Phys. Lett. **69** 25 (1996) 815–3817.
- [51] LEE, S.C., HO, W.Y., HUANG, C.C., MELETIS, E.I., LIU, Y., Hydrogen embrittlement and fracture toughness of a titanium alloy with surface modification by hard coatings, J. Mat. Eng. Performance **5** 1 (1996) 64–70.
- [52] YU, G., GENG, M., HUANG, Y., GONG, X., YU, Y. TANG, D., Application of MEVVA discharge to material surface modification, Nucl. Fusion Plasma Phys. **16** 1 (1996) 31–35.
- [53] THOMAE, R.W., et al., High current ion implantation by plasma immersion technique, Nucl. Instrum. Methods Phys. Res., Section B, Beam Interactions with Materials and Atoms **99** 1–4 (1995) 569–572.
- [54] BERTOTI, I., MOHAL, M., SULLIVAN, J.L., SAIED, S.O., Surface chemical changes in PVD TiN layers induced by ion bombardment, Surface and Interface Analysis **21** 6–7 (1994) 467–473.
- [55] HUSEIN, I.F., ZHOU, Y., QIN, S. CHAN, C., Surface modification by ion and ion beam implantation, Surface Engineering **13** 1 (1997) 56–60.
- [56] BOUCHIER, D., et al., Effect of noble gas ions on the synthesis of c-BN by ion beam–assisted deposition, Nucl. Instrum. Methods Phys. Res., Section B, Beam Interactions with Materials and Atoms **89** 1–4 (1994) 369–372
- [57] BABA, K., HATADA, R., Corrosion resistant titanium nitride coatings formed on stainless steel by ion beam assisted deposition, Surface and Coatings Technol. **66** 1–3 (1996) 368–372.
- [58] CHUBACI, J.F.D., et al., Formation of carbon nitride — a novel hard coating, Nucl. Instrum. Methods Phys. Res., Section B, Beam Interactions with Materials and Atoms **116** 1–4 (1996) 452–456.
- [59] CHEN, Z., et al., Surface engineering of steels by plasma immersion ion implantation and related innovative techniques, Surface Engineering **12** 2 (1996) 137–141.
- [60] ONATE, J.I., et al., Current status of commercial ion implantation in Spain, Surface and Coatings Technol. **103–104** (1998) 185–190.

- [61] ONATE, J.I., et al., Improvement of tribological properties by ion implantation, *Thin Solid Films* **317** (1998) 471–476.
- [62] XIANG, J., HE, S-Z, YANG, K.T, and YUDIAN, F., Formation of AlN films by Al evaporation with nitrogen ion beam bombardment, *Mater. Chem. Phys.* **51** (1997) 199.
- [63] JIANG, Y., ZHANG, H., LIU, C., YANG, S.Z., Novel instrument for material surface treatment by pulsed high power density plasma beam; *Review Scientific Instrum.* **68** (1997) 4221.
- [64] HE, X.J., YANG, S.Z., TAO, K., FAN; Y.D., Reaction of thin metal films with AlN substrate and relevant thermodynamics; *J. Vac. Sci. Technol. A* (in press).
- [65] WEI, K., WU, X., YANG, S-Z, LI, B., LIU C., Study of pulsed high-energy density plasma modified 0.45% C steel. *Materials Science & Engineering A* **254** (1998) 129–135.
- [66] LIU, B., ZHANG, J., CHENG, H.F., JIANG, Y, REN, Y., YANG, S.-Z., Investigation of titanium coatings on Si₃N₄ by using pulsed high energy density plasma (PHEDP) gun, *Materials Chem. Physics* (in press).
- [67] JIZHONG, Z., et al., “Mechanical property changes in silicon nitride by molybdenum ion implantation”, *Functional Materials*, Chemical Engineering Press, Beijing (1997), 817–819.
- [68] GUAN, C., et al., “Molybdenum film deposited on silicon nitride by ion beam enhanced deposition”, *Design and Process Chemical Engineering Press*, Beijing (1997) 373–376 (in Chinese).
- [69] JIZHONG, Z, et al., “Mechanical property change of zirconia implanted by Y ions”, *High Temperature Coatings III (Proc. Symp. San Diego, 1999)*.
- [70] LIU, B., et al., Investigation of titanium coating on Si₃N₄ by using a pulsed high energy density plasma (PHEDP) gun, *Materials Chem. Phys.* (in press).
- [71] GUAN, C., et al., Surface modification of Si₃N₄ by Mo and Y ion implantation, *Thin Solid Films* (in press).
- [72] UGLOV, V.V., et al., *Surf. & Coat. Tech.* **103–104** (1998) 317.
- [73] UGLOV, V.V., et al., *Surf. & Coat. Tech.* **93** (1997) 331.
- [74] UGLOV, V.V., et al., *Surf. & Coat. Tech.* **92** (1997) 190.
- [75] UGLOV, V.V., et al., *Surf. & Coat. Tech.* **97** (1997) 322.
- [76] KHODASEVICH, V.V., et al., *Surf. & Coat. Tech.* **98** (1998) 1433.
- [77] YU, L.D., VILAITHONG, T., SUWANNAKACHORN, D., INTARASIRI, S., THONGTEM, S., Ion implantation modification of special steels in Thailand, *Nucl. Instrum. Methods* **B127/128** (1997) 954–960.
- [78] YU, L.D., VILAITHONG, T., YOTSOMBAT, B., DAVYDOV, S., THONGTEM, S., RHODES, M.W., INTARASIRI, S., SUWANNAKACHORN, D., “Ion implantation for surface modification of hardened tool steels” (*Proceedings Int. Conf. on Surface Engineering, Shanghai, China, 1997*).
- [79] VILAITHONG, T., YU, L.D., VICHASIRIMONGKOL, P., RUJJANAGUL, G., SONKAEW, T., N-ion implantation assisted by preparative and closing implantation for surface modification of tool steel, *Nucl. Instrum. Methods Phys. Res.* **B 148** (1999) 830–835.
- [80] VILAITHONG, T., YU, L.D., VICHASIRIMONGKOL, P., RUJJANAGUL, G., SONKAEW, T., N- ion implantation assisted by preparative and closing implantation for surface modification of tool steel, *Nucl. Instrum. Methods Phys. Res.* **B 148** (1999) 830–835.
- [81] JAGIELSKI, J., MAREST, G., MONCOFFRE, N., *Nucl. Instrum. Meth. Phys. Res.* **B 122** (1997) 575.

- [82] JAGIELSKI, J., KOPCEWICZ, M., TUROS, A., EICHHORN, F., Nucl. Instrum. Meth. Phys. Res. (1999).
- [83] JAGIELSKI, J., et al., Nucl. Instrum. Meth. Phys. Res. (1999).
- [84] MOZETIÈ, M., ZALAR, A., DROBNIÈ, M., Comparison of AES and EXAFS analysis of thin Cu_xAl_y layer on Al substrate, Vacuum **50** (1998) 299–304.
- [85] MOZETIÈ, M., ZALAR, A., DROBNIÈ, M., Self-controlled diffusion of Al in Cu thin film. Vacuum **50** (1998) 1–3.
- [86] MOZETIÈ, M., ZALAR, A., ARÈON, I., PREŠEREN, R., Characterization of copper aluminide thin films, Proc. 34th Int. Conf. On Microelectronics, Devices and Materials, Rog. Slatina (1998), 343–348.
- [87] JAGELSKI, J., et al., Effect of chromium nitride coating on the corrosion and war resistance of stainless steel. Appl Surface Science **156** (2000) 47–64.

NEXT PAGE(S)
left BLANK

CONTRIBUTORS TO DRAFTINGS AND REVIEW

Jagielski, J.	Institute of Electronic Materials Technology, Poland
Khanna, A.S.	Indian Institute of Technology, India
Kucinski, J.	Institute of Atomic Energy, Poland
Misra, D.S.	Indian Institute of Technology, India
Onate, J.I.	Centro Tecnológico Materiales, Spain
Racolta, P.	National Institute of Physics and Nuclear Engineering, Romania
Sioshansi, P.	Radio- Med Corporation, United States of America
Thereska, J.	International Atomic Energy Agency
Tobin, E.	SPIRE Corporation, United States of America
Uglov, V.	Belarussian State University, Belarus
Vilaithong, T.	Chiang Mai University, Thailand
Viviente, J.	Centro Tecnológico Materiales, Spain
Yang, S.	Chinese Academy of Sciences, China
Zalar, A.	Institute of Surface Engineering and Optoelectronics, Slovenia
Zhang, J.	Tsinghua University, China